

ALMA Mater Studiorum  
Universita` degli Studi di Bologna

---

---

SCUOLA DI SCIENZE

Corso di Laurea Magistrale in Astrofisica e Cosmologia

Dipartimento di Fisica e Astronomia

Stellar kinematics of Low-power Radio  
Galaxies: The case of NGC 3557

Candidato:

Francesco Santoro

Relatore:

Chiar.mo Prof.:

Gabriele Giovannini

Co-relatore:

Dott. Isabella Prandoni

Dott. Hans Rudolf de Ruiter



*This thesis has been carried out at INAF/IRA  
(Bologna) and in collaboration with Oxford University,  
as part of an international research project.*



# Contents

<b>1</b>	<b>The current view of local Early-type Galaxies</b>	<b>9</b>
1.1	Introduction . . . . .	9
1.2	The ATLAS <sup>3D</sup> project . . . . .	10
1.3	Morphology and kinematics of ATLAS <sup>3D</sup> ETGs . . . . .	12
1.4	Unveiling the distribution of <i>Fast</i> and <i>Slow Rotators</i> . . . . .	16
1.5	Binary galaxy mergers and the formation of <i>Fast</i> and <i>Slow Rotators</i> . . . . .	19
1.6	Modelling the formation and evolution of <i>Fast</i> and <i>Slow Rotators</i> within a $\Lambda$ CDM Cosmology . . . . .	20
1.7	The kinematic morphology-density relation . . . . .	21
1.8	Angular momentum and nuclear surface brightness profiles . . . . .	23
1.9	The ionized gas kinematics . . . . .	26
1.10	The cold gas content of ATLAS <sup>3D</sup> early-type galaxies . . . . .	29
1.11	On the origin of the molecular and ionized gas in ATLAS <sup>3D</sup> early-type galaxies . . . . .	32
<b>2</b>	<b>Linking radio-loud to radio-quiet Early-type Galaxies</b>	<b>35</b>
2.1	AGN classification and radio galaxies . . . . .	35
2.2	Gas accretion in Radio Galaxies: the LERG and HERG paradigms . . . . .	39
2.3	The Southern radio galaxy sample . . . . .	40
2.4	The role of molecular gas in low power radio galaxies . . . . .	40
2.5	The case of NGC 3557 . . . . .	46
<b>3</b>	<b>The VLT, VIMOS and the IFU observing mode</b>	<b>53</b>
3.1	VLT and the Unit Telescopes . . . . .	53
3.2	The Visual Multi-Object Spectrograph (VIMOS) . . . . .	59
3.2.1	Detectors . . . . .	60
3.3	The Integral Field Unit mode . . . . .	62
3.4	VIMOS IFU observations: NGC 3557 . . . . .	67
3.4.1	IFU data calibration plan . . . . .	67

3.4.2	VIMOS/IFU performance . . . . .	68
<b>4</b>	<b>NGC 3557: VIMOS/IFU Data Reduction</b>	<b>75</b>
4.1	P3D . . . . .	75
4.2	Data reduction steps . . . . .	76
4.2.1	Overview . . . . .	76
4.2.2	Master Bias and Tracing of the spectra . . . . .	77
4.2.3	Creation of the Dispersion-mask . . . . .	78
4.2.4	Flat fielding and transmission corrections . . . . .	84
4.2.4.1	Importance of flat-fielding correction for our NGC 3557 dataset . . . . .	85
4.2.5	Extraction of the spectra . . . . .	85
4.2.5.1	Cosmic ray removal . . . . .	85
4.2.5.2	Recentering the cross-dispersion line profiles . . . . .	86
4.2.5.3	Scattered light subtraction and extraction of the spectra . . . . .	88
4.2.5.4	Realignment along the dispersion axis and wavelength cal- ibration . . . . .	88
4.2.5.5	Correction for transmission and flat-field . . . . .	92
4.2.6	Sensitivity function and Flux Calibration . . . . .	92
4.2.7	Image combination and final image cosmesis . . . . .	102
<b>5</b>	<b>NGC 3557: Stellar kinematics analysis</b>	<b>105</b>
5.1	Extraction of the velocity and velocity dispersion maps . . . . .	105
5.2	Analysis of velocity and velocity dispersion maps . . . . .	111
5.3	Kinematic parameters $\Gamma_{kin}$ , $k_1$ , $k_5/k_1$ . . . . .	115
5.4	Kinematic misalignment: $PA_{phot}$ , $PA_{kin}$ and $\Psi$ . . . . .	118
5.5	Anisotropy diagram ( $V/\sigma - \varepsilon$ ) and angular momentum ( $\lambda_R$ ) . . . . .	119
<b>6</b>	<b>NGC 3557: General Discussion and Conclusions</b>	<b>123</b>
6.1	NGC 3557 kinematics: an open scenario . . . . .	123
6.2	Linking radio-quiet to radio-loud ETGs . . . . .	127
6.3	Future work . . . . .	128

# Sommario

Ad oggi, risulta comunemente accettato che per le radio galassie (RGs) *high-power* sia il gas freddo, trasportato al centro attraverso merging o collisioni con altre galassie ricche di gas, ad alimentare l'attività nucleare della galassia (AGN) e i getti radio. Tuttavia, il gas freddo potrebbe ricoprire un ruolo cruciale anche per l'attività delle radio galassie *low-power*. Le immagini dell' Hubble Space Telescope (HST) mostrano come la polvere sia presente al centro di queste galassie con una frequenza maggiore e in quantità più elevate rispetto alle galassie di tipo early-type (ETGs) che non mostrano attività radio (radio-quiet RGs). In aggiunta, le prime campagne osservative nell'ambito del gas molecolare (CO) mostrano come i rates di detezione siano più alti per le *low power* RGs rispetto alle ETGs radio-quiet (Prandoni et al. 2010, Young et al. 2011). Lo stesso gas molecolare che alimenta l'AGN (a seconda della sua massa, origine e capacità di convertirsi in stelle) può, potenzialmente, dar vita a una componente stellare disaccoppiata. Il disallineamento cinematico tra il gas centrale e la componente stellare risulta, inoltre, un ingrediente chiave per l'attività nucleare (Dumas et al. 2007). Un' analisi spettroscopica di RGs ricche di gas molecolare che impieghi dati integral-field può consentire un interessante confronto con le meglio studiate ETGs radio-quiet, e svelare il ruolo che ricopre l'AGN nello scenario di formazione ed evoluzione delle ETGs insieme al meccanismo che sta alla base dei getti radio.

Un campione “volume-limited” (qui indicato con nome di Campione Sud) costituito da 11 RGs *low power* tutte associate ad ETGs, è stato osservato con il Visual Multi-Object Spectrograph (VIMOS), montato presso il Very Large Telescope (Unit Telescope 3), in modalità Integral Field Unit (IFU). Osservazioni CO di tutte le suddette galassie sono già state eseguite utilizzando APEX, e osservazioni per l'imaging del CO con ALMA saranno proposte. I principali scopi di questo progetto (che coinvolge INAF-IRA, ESO e l'Università di Oxford) riguardano:

- l'indagine dei processi di formazione delle RGs *low power* insieme al ruolo ricoperto dal gas freddo nell'alimentare il Black Hole centrale;
- lo studio della connessione tra il gas molecolare freddo e le proprietà cinematiche delle stelle e del gas ionizzato (dedotte dai dati VIMO/IFU), con particolare attenzione rivolta ad inflow/outflow di gas e ai disallineamenti cinematici tra le diverse componenti;
- lo studio dei possibili effetti dovuti al gas molecolare e al feedback dei getti radio sulla formazione e le caratteristiche della popolazione stellare.

Il presente elaborato è incentrato sull'analisi di dati VIMOS/IFU. Usando le tecniche impiegate per i progetti ATLAS<sup>3D</sup> e SAURON, questo dati possono essere utilizzati al fine

di ottenere la cinematica stellare e del gas, insieme ai principali parametri che descrivono la popolazione stellare di una galassia.

In questa tesi la prima galassia (NGC 3557) del Campione Sud è stata analizzata. NGC 3557 è una ETG associata ad una radio galassia *low power* che mostra getti radio. Osservazioni CO mostrano evidenze di un caratteristico profilo “double-horn” associabile ad una rotazione ordinata del gas in questione (Prandoni et al. 2010). Se confermata, la presenza di un disco di gas molecolare potrebbe essere consistente con il disco di polvere chiaramente visibile nell’immagine HST della galassia stessa (Lauer et al. 2005). La riduzione dai dati VIMOS/IFU per NGC 3557 è stata effettuata utilizzando P3D, un software specifico per la riduzione di dati integral-field. Il risultato finale è un datacube tridimensionale  $(x, y, \lambda)$ , ove  $x$  e  $y$  rappresentano le coordinate celesti della sorgente, mentre la terza dimensione,  $\lambda$ , rappresenta la lunghezza d’onda. Per effettuare l’analisi dei dati, gli stessi sono stati prima sottoposti ad un processo di binning per raggiungere un rapporto S/N costante su tutto il campo di vista. In seguito, la cinematica stellare è stata estratta dagli spettri utilizzando un metodo detto Penalized Pixel-Fitting Method (pPXF). La cinematica stellare mostra un campo di velocità ordinato, senza significative sottostrutture, suggerendo una classificazione di tipo Regular Rotator/*Fast Rotator* per NGC 3557 (Krajnović et al. 2011, Emsellem et al. 2011). Tuttavia, nel momento in cui si utilizzano gli stessi criteri di classificazione impiegati per il campione ATLAS<sup>3D</sup>, diversi fattori vanno presi in considerazione nella classificazione cinematica di NGC 3557. Primo fra tutti la diversa scala spaziale a cui i dati VIMOS/IFU di NGC 3557 fanno riferimento. Alla luce di questo, lo scenario per la classificazione di NGC 3557 rimane aperto: il campo di velocità da noi osservato potrebbe, infatti, essere riconducibile ad un core cinematicamente distinto (KDC) all’interno di uno *Slow Rotator* (Krajnović et al. 2011, Emsellem et al. 2011). Le informazioni cinematiche delle poche radio galassie attualmente osservate in spettroscopia integra-field sembrerebbero supportare quest’ultima ipotesi, sebbene la poca statistica non permetta di effettuare un confronto significativo.

L’analisi dell’emissione del gas ionizzato e della popolazione stellare sarà effettuata in futuro, quest’ultima, insieme ai risultati che saranno ottenuti analizzando i dati VIMOS/IFU dell’intero Campione Sud, potrà costituire una base più solida grazie alla quale poter indagare la struttura cinematica delle radio galassie ed effettuare un confronto statisticamente significativo con il campione ATLAS<sup>3D</sup>.

# Introduction and thesis outline

Understanding the process of galaxy formation and evolution is a key issue of modern astronomy. One of the most demanding requirements on galaxy formation theories is to reproduce the large-scale properties and scaling relations of early-type galaxies (ETGs). Among these, the optical colour-magnitude diagram stands out, with most ETGs restricted to a narrow red sequence, most late-type disk galaxies present in a diffuse blue cloud, and few galaxies in the presumably fast migration region known as the green valley (here the star formation seems to shut up down rapidly; e.g. Faber et al 2007). ETGs themselves are known to be quite heterogeneous: a wide range of kinematic substructures are indeed observed (e.g. Emsellem et al. 2004) spanning from decoupled prograde stellar disks in fast-rotating galaxies to kinematically-misaligned cores in the preferentially massive slow-rotating spheroids (Emsellem et. al 2011). How the star formation shuts down in ETGs and how substructures form are both hotly debated issues, and the answers to these questions may be tightly connected. On the one hand, feedback by supermassive black hole thorough jets is generally called upon to suppress star formation. On the other hand, theorists explain the variety of dynamical structures observed by suggesting various origins: remnants of dry mergers (Bendo & Barnes 2000) and new systems formed of gas from either wet mergers or stellar mass loss (Barnes 2002, Sage & Welch 2006).

It is generally accepted (e.g. Heckman et al. 1986, Baum et al. 1992) that *powerful* radio galaxies (RG i.e. radio-loud ETGs) are triggered by cold gas transported to the centre through merging or collisions with gas-rich galaxies. The most compelling evidence that cold gas can play a role in fueling *low power* RG as well, is that in such a systems dust is detected more often and in larger quantities than in radio-quiet ETGs (de Ruiter et al. 2002). In addition the first systematic CO observing campaigns of nearby (and mostly low-power) RGs (e.g. Prandoni et al. 2007, 2010; Ocaña Flaquer et al. 2010) have revealed higher CO detection rates than in radio-quiet ETGs. This supports the idea that the jets are powered by the accretion of cold gas, rather than by Bondi accretion of hot, X-ray emitting plasma (Allen et al. 2006). Large quantities of warm, but still molecular gas have recently been found in radio-loud Molecular Hydrogen Emission Galaxies (MOHEGs), including some with high cold gas masses (Ogle et al. 2010), and this is also a plausible candidate for the fuel supply. The H<sub>2</sub> lines do not appear related to star-formation, but are excited by shocks, related to AGN feedback. The same molecular gas fueling AGN will also naturally give rise to a decoupled stellar component depending on it mass, origin and ability to turn into stars. Systematic optical integral-field spectroscopic analysis of molecular gas-rich RGs with currently active jets can thus provide a crucial comparison with existing studies of radio-quiet ETGs and allow to isolate the role played by AGN in the overall formation and evolutionary scenario of ETGs.

A complete volume-limited ( $z < 0.03$ ) sample of 11 *low power* RGs in the Southern

sky (hereafter referred to as the Southern Sample), associated with ETGs, has been observed with the Visual Multi-Object Spectrograph (VIMOS) mounted on VLT UT3 in IFU (Integral Field Unit) observing mode. All the galaxies have also been detected in CO with APEX (Prandoni et al. 2010, Senatore et al. 2013), and will be proposed for CO imaging with ALMA. The main aims of this project (involving INAF-IRA, ESO and Oxford University) are:

- an assessment of the formation processes of (*low-power*) RGs and of the possible role played by cold gas in fueling the central black hole;
- a study of the connection between cold molecular gas and stellar and (optical) gas kinematic features, with particular respect to gaseous flows and kinematic misalignments;
- a study of the possible effects produced by molecular gas and jet-induced feedback on the star formation and stellar population.

The present thesis is focused on the analysis of VIMOS/IFU data. Using the techniques adopted for the SAURON and ATLAS<sup>3D</sup> projects, such data can be employed to obtain 2D stellar kinematics maps, 2D ionized gas kinematics maps and information about the ionized gas spatial distribution and the stellar population characteristics. The stellar kinematics can reveal the presence of substructures associated with the molecular gas, and standard stellar population synthesis models will provide information about stellar ages, metallicities and  $\alpha$ -element abundances of the stars. Investigations can be made about the process that dominates the gas ionization while gas-star misalignments and gas-phase metallicity will provide two powerful diagnostic tools to understand the gas origin.

In this thesis the first galaxy (NGC 3557) of the Southern Sample has been analyzed. NGC 3557 is an early type galaxy associated to a *low power* RG showing twin radio jets. CO line observations show some evidence for a double-horned spectrum profile, consistent with ordered rotation (Prandoni et al. 2010). If confirmed, the presence of a CO disk in the galaxy core would be consistent with the presence of a dusty disk in HST high resolution images (Lauer et al. 2005).

The NGC 3557 VIMOS/IFU data reduction has been carried out using the P3D software, a general data-reduction tool for fiber-fed integral-field spectrographs. The final result is a three-dimensional datacube ( $x, y, \lambda$ ), where  $x$  and  $y$  are the sky coordinates and  $\lambda$  is the wavelength. In order to perform the data analysis, two-dimensional data were first binned to a constant signal-to-noise ratio per bin using the Voronoi Binning Method. 2D stellar kinematics maps were thus obtained using a Penalized Pixel-Fitting method (pPXF).

This thesis is mainly focused on the analysis of stellar kinematics ( $v$  and  $\sigma$ ) of NGC 3557, while gas kinematics and stellar population properties will be analyzed in the next future. NGC 3557 does not show significant kinematic substructures, and the galaxy can be classified as a *Fast Rotator* using the  $\lambda_R$  parameter, according to Emsellem et al. (2007). However, due to the limited field of view of our IFU observations, we cannot exclude that we are seeing a decoupled rotating core in a galaxy characterized by slower rotation on a larger scale. Such rotating core could be associated to the CO and dust disks observed in NGC 3557. This hypothesis is supported by the fact that most massive and largest ETGs like NGC 3557, are always associated with slow rotation (Emsellem et al. 2011, Krajnović et al. 2013).

The stellar kinematics properties of NGC 3557 are in line with those of the few other four RGs, for which integral-field spectroscopy is available.

The presence of dust in the centre of NGC 3557 prevents from deriving its nuclear surface brightness profile. However its kinematic properties suggest that this is a core galaxy, in line with what typically found for RGs (de Ruiter et al. 2005, Capetti et al. 2005, Capetti et al. 2006). The analysis of core ATLAS<sup>3D</sup> galaxies (Krajnović et al. 2013) showed that such galaxies are typically associated to massive *Slow Rotators*. In the few cases where a *Fast Rotator* is found the angular momentum is however rather low ( $\lambda_R \leq 0.2 - 0.3$ ). This is observed also in NGC 3557.

A full statistical comparison between RGs and radio-quiet ATLAS<sup>3D</sup> galaxies is, however, beyond the scope of this thesis, as it requires the VIMOS/IFU data of the entire sample of 11 RGs to be analyzed.

The thesis is organized in six Chapters:

- In the first chapter the main properties of radio-quiet ETGs are presented on the basis of the results obtained in the framework of the ATLAS<sup>3D</sup> project, with special focus on stellar kinematics.
- In the second chapter the issue of the formation of radio galaxies is introduced, with particular regard to *low power* RGs. The sparse information on the kinematic properties of RGs is also discussed. Finally we present our Southern Sample; with particular focus on NGC 3557.
- In the third chapter we give an overview of the VLT telescope and of the VIMOS spectrograph. Particular focus is here given to the Integral Field Unit characteristics and performance. Finally the NGC 3557 VIMOS/IFU dataset is described.
- In the fourth chapter we describe the VIMOS/IFU data reduction process carried out using the P3D software. The main reduction steps include *spectral tracing*, the creation of a *dispersion mask*, *flat fielding*, accurate *extraction* of the spectra and *flux calibration*.
- In the fifth chapter we present the analysis of the stellar kinematics of NGC 3557.
- In chapter six we discuss our results in the framework of radio-quiet and radio-loud ETGs and we briefly outline the future perspectives of this work.



# Chapter 1

## The current view of local Early-type Galaxies

### 1.1 Introduction

High redshift galaxies observations typically lack of spectral information and spatial resolution, so nearby objects constitutes a useful laboratory to trace the fossils of galaxy formation processes. Early-type galaxies (ETGs) are particularly useful for this purpose as they are old objects with limited star formation and dust content.

The Sloan Digital Sky Survey (SDSS; York et al. 2000) has given a significant contribution in the understanding of formation of local ETGs. The SDSS has established a statistically significant bimodality in the colour distribution of local galaxies. Galaxies can be separated in two distinct groups: “blue cloud” galaxies are mainly star-forming spiral galaxies while the “red sequence” group is constituted by non-star-forming ETGs, a minor fraction of transitional galaxies can be found in the so-called green valley. Galaxy formation scenarios have been tested in order to reproduce this bimodality: a mechanism that suppress episodes of intense star formation and expels gas from the system is needed in order to allow the rapid transition of a galaxy from the blue cloud to the red sequence (e.g. Faber et al. 2007). There is a common feature between the different simulations made to reproduce the bimodality, red sequence galaxies seems to form by dissipational *wet mergers* of gas-rich blue cloud galaxies followed by the quenching of the resulting star formation by rapid gas ejection. The mechanism driving the gas ejection is still uncertain. It can be the feedback by a supermassive black hole, supernovae winds, gravitational gas heating or shock heating in massive halos. However this process alone cannot account for the formation of the most massive ETGs. It seems that dissipationless dry mergers of red sequence galaxies are needed (e.g. Oser et al. 2010).

Major mergers, both dry and wet, produce red bulge dominated galaxies when the feedback is included in the model, the kinematical structure of the remnant is, however, quite different in the two cases. A major merger (1:1) between blue gas rich galaxies produces a red stellar system dominated by rotation (after the gas removal or conversion into stars, e.g. Jesseit et al. 2009), while a red galaxy with little or no net rotation is produced if the progenitors are red gas-poor galaxies. Minor mergers (1:3 or less), on the other hand, closely retain the structure of the progenitors. Therefore the remnant of spiral mergers will always display significant rotation (e.g. Jesseit et al. 2009).

Under the hypothesis that galaxies assemble by mergers, the simulations thus indicate a kinematical differentiation, predicting a separation between fast and slow rotating galaxies within the red sequence. Various observational indicators have been investigated in the past in order to disentangle this dichotomy in ETGs.

Based on imaging, the ETGs can be divided in galaxies with or without a disk-like structure, this gave rise to the classical separation between ellipticals (E) and lenticulars (S0), and to the so-called Hubble tuning-fork. Given the lack of information about galaxy inclination, this classification appears not strictly bounded to ETGs physical properties, though. A promising improvement was introduced by the so-called diskiness parameter which allowed to show the presence of disks in galaxies classified as ellipticals. The main problem of this classification is related to inclination effects: for galaxies with inclination below  $\sim 60^\circ$  the disk deformation of the isophotes ceases to be seen. The dynamical state of the galaxies was therefore directly investigated using the  $V/\sigma$  parameter, where  $V$  and  $\sigma$  are respectively a measure of ordered and random motions, in the galaxy. The combination of photometric and kinematic parameters clearly showed the existence of luminous ETGs with round or boxy isophotes that rotate slowly together with fainter ETGs with disk-like isophotes that rotate fast. However this information was based on long-slit observations, only performed (at best) along the major and minor axes of the galaxy. In order to obtain a complete characterization of the kinematic properties of a galaxy the introduction of integral field spectrographs (IFS), able to cover a significant part of the galaxy body, represents a huge leap forward.

The SAURON project (de Zeeuw et al. 2002) has carried out observations of a representative sample of local ETGs in integral field spectroscopic mode revealing many types of kinematic structures in ETGs. The existence of two main classes of ETGs was confirmed looking from the analysis of the stellar velocity fields. The  $\lambda_R$  parameter represents the quantitative measurement used for this differentiation. Such a parameter turns out to be more powerful in the distinction between *Fast* and *Slow Rotators* with respect to the classical  $(V/\sigma, \epsilon)$  diagram and is nearly insensitive to projection effects (Emsellem et al. 2007, Cappellari et al. 2007). The SAURON survey was thus crucial in bringing the *Fast/Slow Rotator* dichotomy to light. However, due to its exploratory character, the sample selection criteria were not optimal and did not allow a complete quantitative statistical comparison of galaxies characteristics with simulation results. Moreover the limited number of selected galaxies (48) introduce a large statistical uncertainties.

The following ATLAS<sup>3D</sup> project (Cappellari et al. 2010) was aimed at building a more statistically relevant volume-limited sample of galaxies, able to better compare the observed measurements with theoretical predictions. The observational goals of the ATLAS<sup>3D</sup> project not only include the characterization of the stellar and gas kinematics together with the derivation of the stellar population parameters through IFS observations, but also the assessment of recent gas accretion through cold atomic gas (HI) radio observation, and the tracing the ongoing accretion and star formation activity through cold molecular gas (CO) observations.

## 1.2 The ATLAS<sup>3D</sup> project

The ATLAS<sup>3D</sup> project is based on a complete volume-limited sample of 260 early type galaxies extracted from a volume-limited parent sample of galaxies including both spirals

and ETGs.

The parent sample was selected on the basis of the near-infrared ( $\sim 2.2 \mu\text{m}$ )  $K_s$ -band luminosity provided by the Two-Micron All Sky redshift Survey (2MASS; Skrutskie et al. 2006) used as a proxy of the stellar mass. The main selection criteria are:

- Distance  $D < 42 \text{ Mpc}$
- Galaxy absolute magnitude  $M_k < -21.5 \text{ mag}$
- Observability  $|\delta - 29^\circ| < 35^\circ$
- Galaxy zone of avoidance  $|b| > 15^\circ$

A complete and representative sample of 871 galaxies was selected in a survey volume of  $1.16 \times 10^5 \text{ Mpc}^3$ : 70% are spirals and the remaining part are ETGs.

The ETGs in the parent sample were selected from their morphology through a visual inspection of the true-colour red-green-blue images provided by the SDSS. The revised Hubble classification scheme, entirely based on the presence/absence of spiral arms or dust lanes in highly inclined galaxies was used to perform the morphological selection.

The ATLAS<sup>3D</sup> project includes :

- IFS observations performed with the SAURON integral-field spectrograph mounted at the William Herschel Telescope (WHT) at the Observatory of El Roque des Los Muchachos on La Palma. 64 ETGs had been already observed in the framework of the SAURON (de Zeeuw et al. 2002) and other projects. Such observations were obtained in low spatial resolution mode. The Field of View (FoV) is  $33'' \times 41''$  with  $0''.94$  square lenslets. Typically the images probe 1 effective radius ( $R_e$ ), although for the largest galaxies only  $0.5R_e$  was fully probed. The covered spectral range goes from 4800 to 5380 Å, the spectral resolution is 4.2 Å FWHM ( $\sigma_{\text{instr}}=105 \text{ km s}^{-1}$ ). The other 196 galaxies were observed is performed with the volume phase holographic (VPH) grating that provides a resolution of 3.9 Å FWHM ( $\sigma_{\text{instr}}=98 \text{ km s}^{-1}$ ) over the same wavelength range as for the previous observations. IFS observations were mainly used to reconstruct the stellar and ionized gas kinematics (velocity  $v$ , dispersion  $\sigma$  and the higher Gauss-Hermite moments  $h_3$  and  $h_4$ ) and the stellar population properties. An observing campaign is ongoing to obtain IFS observations for a subsample of ATLAS<sup>3D</sup> galaxies out to a large radius (3-5  $R_e$ ).
- HI interferometry observations of 170 galaxies of the sample (those at  $\delta > 10^\circ$ ) obtained with the Westerbork Synthesis Radio Telescope (WSRT). H I cubes have a spatial and velocity resolution of  $\sim 30 \text{ arcsec}$  and  $16 \text{ km s}^{-1}$ , respectively, over a FoV of  $\sim 1 \text{ deg}^2$  and a velocity range of  $\sim 4000 \text{ km s}^{-1}$ .
- CO single-dish observations performed at the IRAM 30m telescope for the entire ATLAS<sup>3D</sup> sample. Both the  $^{12}\text{CO}$  J=1-0 and 2-1 emission lines are searched pointing at the galaxy centre. The covered bandwidth is  $1300 \text{ km s}^{-1}$  centered at the optical systemic velocity.
- CO interferometry observations for the brightest CO detected galaxies. CO (1-0) emission line observations were obtained with the Berkeley-Illinois-Maryland Array

(BIMA) with the Plateau de Bure Interferometer (PdBI), and with the Combined Array for Research in mm-wave Astronomy (CARMA) millimeter interferometers. This allowed to map the distribution and kinematics of the molecular gas.

- Optical imaging observations with the Wild Field Camera (WFC) at the 2.5m Isaac Newton Telescope (INT). u, g, r, i and z-band imaging was obtained only for those galaxies not observed in the framework of SDSS. In addition deep optical images were obtained with the MegaCam camera installed on the Canada-France-Hawaii (CFH) Telescope in order to investigate the presence of low luminosity features in the outskirts of ETGs that could reveal signatures of the past accretion mass history.

Finally the project includes also theoretical efforts to interpret the observations using models of galaxy formation: binary merger numerical simulations are conducted to understand the formation and evolution of red sequence galaxies; semi analytical models are used to follow the individual evolution of a large statistical sample of galaxies; and cosmological simulations of individual galaxies are employed to better understand the present kinematical structure of ETGs in a complete cosmological context.

The main results of the ATLAS<sup>3D</sup> project are reported in the following sections, with special focus on the more relevant aspects for this thesis. A study of the ionized gas based on the SAURON project is also discussed.

### 1.3 Morphology and kinematics of ATLAS<sup>3D</sup> ETGs

Krajnović et al. (2011) investigated the morphology and kinematics properties of the ETGs in the ATLAS<sup>3D</sup> sample. Ground-based *r*-band images were first employed to find bars, interaction features or dust structures. Bars and rings were detected in  $\sim 25\%$  and  $\sim 17\%$  of the sample galaxies respectively, and often occur together. The total amount of systems showing bars and/or rings is thus 30% (78 sources). About 18% of the systems show dusty features with dust in ordered disks (24 objects) or in filamentary structures (20 objects). About 8% of galaxies show interaction features and not fully settled figures at large radii. Most of them are not actively merging systems.

The analysis of the velocity maps was performed using KINEMETRY<sup>1</sup> (Krajnović et al. 2006). Kinemetry is a generalization of isophotometry of surface brightness images to the other moments of the Line-Of-Sight Velocity Distribution (LOSVD): i.e. the mean velocity, the velocity dispersion, and the higher moments  $h_3$  and  $h_4$ . The method consists in finding the best-fit ellipses along which the velocity profile can be described as a function of the so-called eccentric anomaly cosine. Kinemetry first fits the ellipse parameters, the position angle  $\Gamma_{kin}$ , and the flattening  $q_{kin}$ . The velocity profile is decomposed in odd Fourier harmonics. The first order term  $k_1$  corresponds to the mean velocity, while the higher ones represent deviations from the assumed law. All the values are determined within  $1 R_e$  or within the maximum semi-major axis probed, when SAURON FoV does not cover the galaxy up to  $1 R_e$ . Particular useful is the  $k_5$  harmonic, as it quantifies the deviations of the profile from a simple thin (inclined) rotating disk. Also useful is the  $\overline{k_5/k_1}$  ratio obtained following the prescription of Ryden et al. (1999). When the  $\overline{k_5/k_1}$

---

<sup>1</sup>The IDL KINEMETRY routine is available at <http://www.eso.org/~dkrajnov/idl>.

Feature	RR	NRR
NF	171	12
2M	36	0
KT	2	0
KDC	0	11
CRC	1	7
$2\sigma$	4	7
LV	0	7

Table 1.1: Number of ATLAS<sup>3D</sup> galaxies for each Kinematic type and feature.

value is larger than 4% the velocity map is flagged as non consistent with a cosine law. This value was considered as the minimum significant one when taking into account the intrinsic mean uncertainty of the  $k_5/k_1$  parameter (0.03) and its dispersion (0.01). Based on the  $k_5/k_1$  values, a distinction between two categories can be made: galaxies showing  $k_5/k_1 < 0.04$  have velocity maps characterized by ordered rotation and are called *Regular Rotators* (RR) while galaxies with  $k_5/k_1 > 0.04$  show velocity fields with complex structures and are called *Non-Regular Rotators* (NRR). Most galaxies (82%) are classified as *Regular Rotators*, while only 44 galaxies were found to be *Non-Regular Rotators*. Several distinct kinematical features are visible in the velocity maps (in particular for NRR). They probably are the fossil signatures of different formation processes.

In order to quantify the frequency of such features in both *Regular* and *Non-Regular rotators* a further classification was defined:

- *No Feature* (NF): a constant  $\Gamma_{\text{kin}}$  is measured as a function of the radius.
- *Double Maxima* (2M): the  $k_1$  radial profile is characterized by an initial rise followed by a decrease and another rise.
- *Kinematic Twist* (KT): a smooth variation with radius of  $\Gamma_{\text{kin}}$  is found, with an amplitude of at least  $10^\circ$ .
- *Kinematic Distinct Core* (KDC): an abrupt change in  $\Gamma_{\text{kin}}$  is found, with an amplitude of  $\sim 30^\circ$  between adjacent radii, and  $k_1$  drops to zero in the transition region.
- *Counter-Rotating Core* (CRC): is a special case of KDC with a change in  $\Gamma_{\text{kin}}$  of  $\sim 180^\circ$
- *Low-level Velocity* (LV): a very low  $k_1$  is measured ( $k_1 < 5\text{km s}^{-1}$ ).
- *Double  $\sigma$*  ( $2\sigma$ ): two symmetric peaks, lying along the major ellipse axis, are found in the velocity dispersion map.

Table 1.1 reports a summary of the kinematic features found in the ATLAS<sup>3D</sup> sample.

Based on the kinematic features above, a system of five groups was proposed to classify ATLAS<sup>3D</sup> galaxies :

- *group a* : galaxies that do not show any rotation
- *group b* : galaxies with complex velocity maps but no specific kinematic feature

Group	# of galaxies	kinematic features
a	7	NRR/LV
b	12	NRR/NF
c	19	NRR/KDC, NRR/CRC, RR/CRC
d	11	NRR/ $2\sigma$ , RR/ $2\sigma$
e	209	RR/NF, RR/2M, RR/KT

Table 1.2: Kinematic groups of the ATLAS<sup>3D</sup> sample.

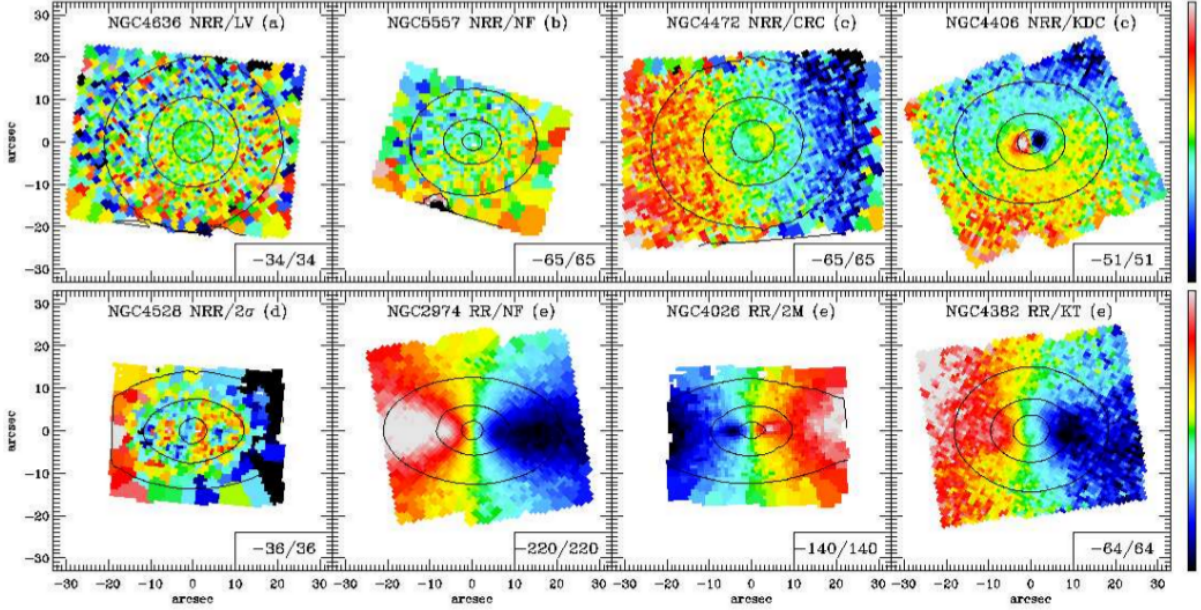


Figure 1.3.1: Examples of the various kinematic features found in the mean velocity maps, as indicated in the upper part of the panels. The velocity range (in  $\text{km s}^{-1}$ ) is reported in the bottom right corner of each panel.

- *group c* : galaxies with KDC or CRC
- *group d* : galaxies with a double peak in the velocity dispersion map
- *group e* : galaxies with ordered rotation, two aligned velocity maxima or kinematic twists

Table 1.2 summarizes the number of galaxies in the five groups and the kinematic features typical of each group. Figure 1.3.1 shows velocity map examples showing the various kinematic features.

Other two important parameters were derived for ATLAS<sup>3D</sup> galaxies: the global kinematic position angle ( $\text{PA}_{\text{kin}}$ ) and the photometric position angle ( $\text{PA}_{\text{phot}}$ ).

$\text{PA}_{\text{kin}}$  is the angle describing the mean stellar motion. It is defined as the angle between the North and the receding part of the velocity map.  $\text{PA}_{\text{phot}}$  measures the orientation of the stellar distribution traced by the light, and defines the position of the apparent photometric major axis measured East of North.

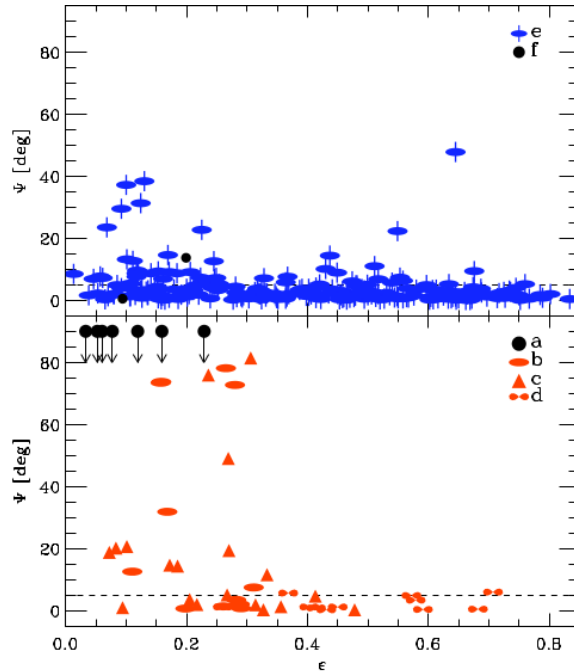


Figure 1.3.2: Distribution of the kinematic misalignment  $\Psi$  as a function of the ellipticity  $\varepsilon$ . In the *top panel* only the *group e* galaxies are plotted (the two points classified as *f* are two unclassified galaxies). In the *bottom panel* *groups a, b, c, d* are shown. The horizontal dashed line indicates the  $\Psi = 5^\circ$  value.

Following the prescription of Fornax et al. (1991) the kinematic misalignment angle  $\Psi$  was calculated as the difference between the measured  $\text{PA}_{\text{phot}}$  and  $\text{PA}_{\text{kin}}$ , and approximates the true kinematic misalignment angle. The kinematic misalignment angle  $\Psi$  is remarkably uniform: about 71% of galaxies have misalignments  $\Psi \leq 5^\circ$ , 90% are consistent to have  $\Psi \leq 15^\circ$ , and the rest (10%) is spread over the remaining  $75^\circ$ . A dependence of  $\Psi$  on the ellipticity  $\varepsilon$  was noted: rounder objects more likely have larger  $\Psi$ . *Group e*, that includes the vast majority of the sample galaxies, is generally characterized by well aligned systems, with very few exceptions. Misaligned systems are mainly morphologically disturbed galaxies (showing rings, bars, dust and interaction features) or galaxies with a normal morphological structure that however show complex kinematics. Figure 1.3.2 shows the distribution of ATLAS<sup>3D</sup> galaxies in the  $\Psi - \varepsilon$  plane.

The small kinematic misalignments found for the great majority of the galaxies in the ATLAS<sup>3D</sup> sample seem to indicate that they are axisymmetric systems. Several galaxy formation processes (valid for the central baryon-dominated region of local ETGs) most often produce disk-like objects that maintain the axisymmetric shape of their progenitors. Such processes are minor mergers, gas accretion, secular evolution together with environmental influences. These are thus the candidate formation processes for most of local ETGs. High misalignments, on the other hand, imply triaxial figures. Such figures are likely created via major merger with or without gas dissipation. Major mergers can therefore account for no more than 10% of the ATLAS<sup>3D</sup> galaxies ( $\Psi > 15^\circ$ ).

## 1.4 Unveiling the distribution of *Fast* and *Slow Rotators*

Emsellem et al. (2011) presented a census of the stellar angular momentum in the central region of ETGs. The difficulty of disentangling lenticular galaxies (disk-like systems) from elliptical ones (spheroidal-like systems) arises from complications associated to inclination effects or from limitations in the photometric measurements. Emsellem et al. (2007) suggest a new parameter ( $\lambda_R$ ) to better classify ETGs, accounting for their kinematic properties. IFS observations are the key ingredient to obtain this kind of measurement.  $\lambda_R$  is a simple parameter able to quantify the apparent stellar angular momentum of a galaxy using the first two stellar velocity moments ( $v$  and  $\sigma$ ). Emsellem et al. (2007) and Cappellari et al. (2007) tested the capabilities of this parameter on the SAURON survey, dividing the galaxies in two families: *Slow Rotators* ( $\lambda_R < 0.1$ ), with little or no rotation, generally characterized by high values of  $\Psi$  and often containing kinematically decoupled cores (KDC); and *Fast Rotators* ( $\lambda_R \geq 0.1$ ), which exhibit regular stellar velocity fields, and resemble disk-like rotational objects. Following the prescriptions of such works, the classification of the ATLAS<sup>3D</sup> galaxies was performed and refined, by introducing also the ellipticity  $\varepsilon$  parameter.

After extracting the kinematic information from the spectra, the  $\lambda_R$  parameter was estimated for each ATLAS<sup>3D</sup> galaxy using the following relation:

$$\lambda_R \equiv \frac{\langle R|V| \rangle}{\langle R\sqrt{V^2 + \sigma^2} \rangle} \quad (1.4.1)$$

where  $R$  is the distance from the centre,  $V$  and  $\sigma$  are the measured velocity and velocity dispersion at that radius.

The  $V/\sigma$  parameter can be calculated by averaging the surface brightness weighted values of the velocity and velocity dispersion over the FoV. Similarly, a surface brightness weighted value for the ellipticity  $\varepsilon$  can be estimated.

It should be noted that both  $\lambda_R$  and  $V/\sigma$  depend on the spatial extent over which the median values are calculated.  $\lambda_R$  values are typically measured within an aperture radius equal to the effective radius  $R_e$ . When the SAURON FoV does not fully cover  $1 R_e$ , the maximum radius  $R_m \equiv \sqrt{A_s/\pi}$  is defined, as the radius corresponding to the maximum aperture (with area  $A_s$ ) actually probed by SAURON.

Accurate dynamical masses  $M_{dyn}$  were also derived via a Multi-Gaussian Expansion (Emsellem et al. 1994) of the galaxy isophotes and detailed Jeans anisotropic dynamical models (Cappellari 2008, Scott et al. 2009) of the stellar kinematics (Cappellari et al. 2010). Usually  $M_{dyn}$  is about two times larger than the total dynamical mass within a sphere containing half of the galaxy light.

The estimated values at  $1 R_e$  are usually indicated as  $\lambda_{R_e}$ ,  $(V/\sigma)_{R_e}$  and  $\varepsilon_e$ .

As already noted in Emsellem et al. (2007) the  $\lambda_R - \varepsilon$  diagram can give important clues about the intrinsic morphology and dynamics of ETGs. Cappellari et al. (2007) showed that there seems to be a broad trend between the anisotropy of ETGs, parametrized with  $\beta^2$ , and the intrinsic (edge-on) ellipticity  $\varepsilon_{intr}$ . In Figure 1.4.1 the  $\lambda_{R_e} - \varepsilon_e$  diagram for

---

<sup>2</sup> $\beta$  is the anisotropy parameter defined as  $1 - \sigma_z^2/\sigma_R^2$  where  $\sigma_z^2$  and  $\sigma_R^2$  are the cylindrical components

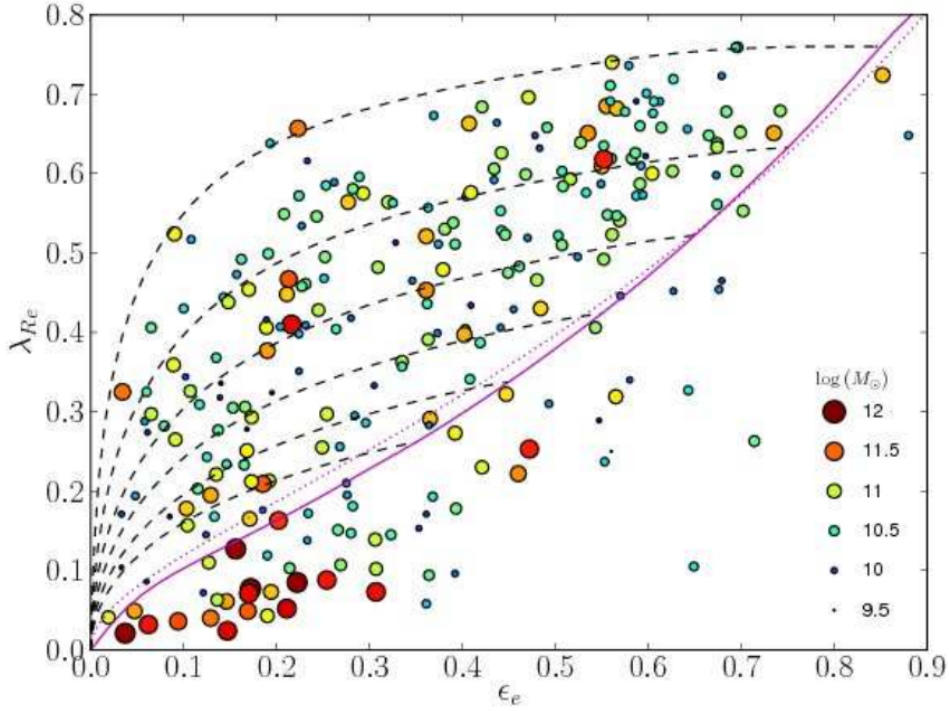


Figure 1.4.1:  $\lambda_{R_e} - \varepsilon_e$  diagram for the ATLAS<sup>3D</sup> sample. The colour and size of the circles are associated to the estimated mass of each galaxy (see legenda in the bottom right corner). The dotted and solid magenta lines show the edge-on view for elliptoidal galaxies integrated up to infinity (using  $\beta = 0.7 \times \varepsilon_{intr}$ ) and to  $1R_e$  (using  $\beta = 0.65 \times \varepsilon_{intr}$ ) respectively. The black dashed lines correspond (from up to bottom) to  $\varepsilon_{intr} = 0.85, 0.75, 0.65, 0.55, 0.45, 0.35$ , derived as function of viewing angle (going from edge-on to face-on from right to left).

the ATLAS<sup>3D</sup> sample is shown, the magenta line represents the relation  $\beta = 0.7 \times \varepsilon_{intr}$  for edge-on viewed systems while the dashed black lines show the effect of inclination. As can be seen, galaxies with  $\lambda_{R_e}$  values significantly larger than 0.1 are located above the magenta line and the upper dashed line, corresponding to  $\varepsilon_{intr} = 0.85$ , provides a good envelope for the galaxies in the sample. This modelization suggests that as ellipticity decreases also the apparent angular momentum decreases. This result was used to refine the criterion to define *Fast* and *Slow Rotators*.

Keeping in mind that two galaxies with the same apparent angular momentum but different (intrinsic) flattening must have, by definition, a different orbital structure, the new refined scheme takes into account the apparent ellipticity. The dividing threshold for  $\lambda_R$  is thus imposed to be proportional to  $\sqrt{\varepsilon}$  with a scaling parameter  $k_{FS}$  which depends on the considered aperture ( $R_e$  or  $R_e/2$ ):

$$\lambda_{R_e} = (0.31 \pm 0.01) \times \sqrt{\varepsilon_e} \quad (1.4.2)$$

$$\lambda_{R_e/2} = (0.265 \pm 0.01) \times \sqrt{\varepsilon_{e/2}} \quad (1.4.3)$$

of the stellar velocity dispersion for a steady-state system.

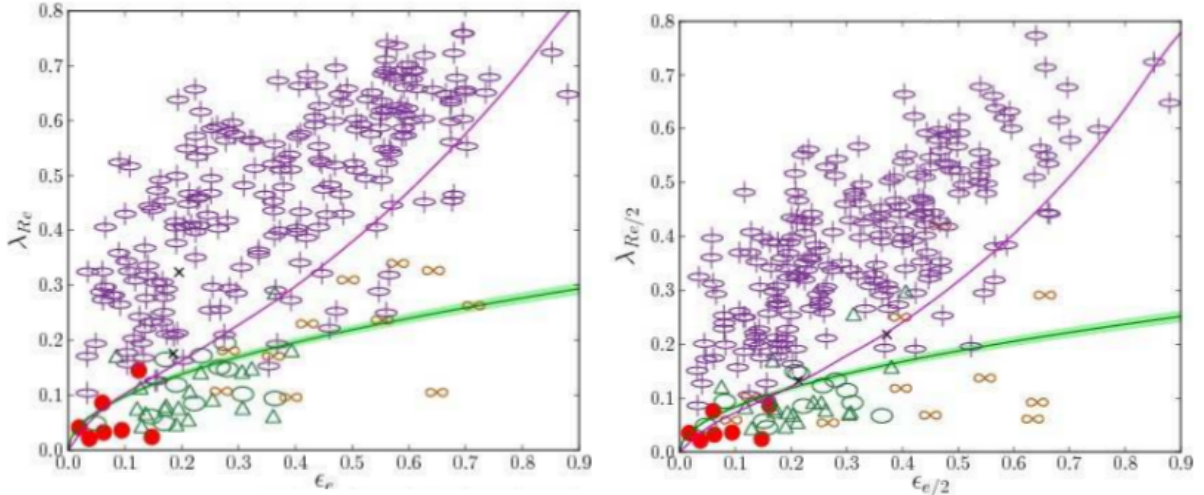


Figure 1.4.2:  $\lambda_R - \varepsilon$  diagram obtained for  $1 R_e$  (left panel) and  $R_e/2$  (right panel) apertures. Red circles indicate *group a* galaxies, green ellipses indicate *group b* galaxies, green triangles indicate *group c* galaxies, orange lemniscates indicate *group d* galaxies, purple symbols indicate *group e* galaxies and black crosses indicate the 2 unclassified galaxies. The solid green line represents the threshold defined by Equations 1.4.2 and 1.4.3 while the magenta line shows the edge-on view for ellipsoidal galaxies integrated up to  $1R_e$  (using  $\beta = 0.65 \times \varepsilon_{intr}$ ).

Equations 1.4.2, 1.4.3 represent the new criterion used to separate *Fast* and *Slow Rotators*. In Figure 1.4.2 the  $\lambda_R - \varepsilon$  diagrams are shown for  $1R_e$  and  $R_e/2$  apertures. The galaxies are classified using the kinematic groups defined by Krajnović et al. (2011) and the new threshold (solid green line) is found to effectively discriminate between galaxies of *group e* and galaxies belonging to the others groups (i.e. galaxies with regular and non-regular velocity patterns respectively).

The  $R_e$  scale is the preferred scale to probe *Fast Rotators* and *Slow Rotators* due to its capability to trace a significant fraction of the stellar mass, and being large enough to be robust against variations in the observational conditions.

Importantly, no clear trend was found between  $\lambda_R/\sqrt{\varepsilon}$  and the morphological type of the ATLAS<sup>3D</sup> galaxies ( $T$ ) reported in the HyperLeda database<sup>3</sup>. Isophotal shapes and central light profiles were analyzed in order to find common trends with the *Fast/Slow Rotator* classification. No simple link was found between the  $a_4$  parameter (quantifying the degree of disciness or boxiness of the isophotes) and the kinematic classification, although a clear trend for *Fast Rotators* to have central light excesses and *Slow Rotators* to exhibit central light deficits was found. This demonstrates that the classical paradigm proposed for ETGs, divided in disk-like S0 and spheroidal-like E elliptical systems, is too simplistic.

According to the new revised criterion, about  $86 \pm 2\%$  (224/260) of the ATLAS<sup>3D</sup> galaxies are found to be *Fast Rotators*. They have typically aligned photometric and kinematic axes (within  $5^\circ$ ), they are consistent with being simple oblate systems (with or without bars) spanning a range of intrinsic ellipticities (between about 0.35 and 0.85).

A Monte-Carlo simulation confirmed the latter hypothesis:  $\lambda_{R_e}$  values are obtained for a mock sample of 50000 galaxies assuming a Gaussian distributions for both the intrinsic

<sup>3</sup><http://leda.univ-lyon1.fr/>

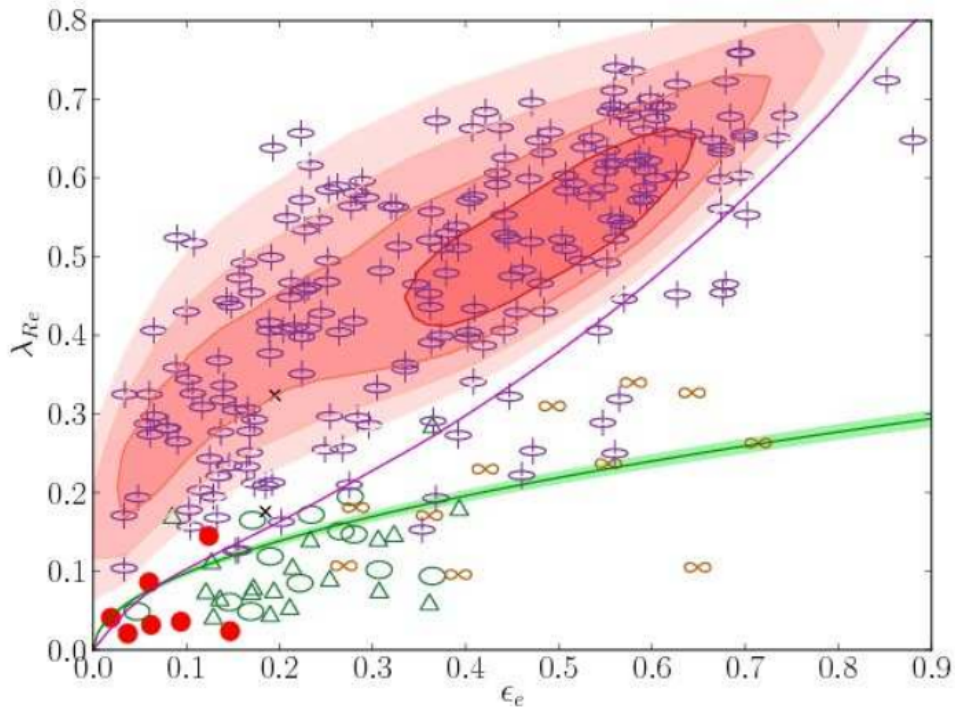


Figure 1.4.3:  $\lambda_{Re} - \epsilon_e$  diagram. The coloured contours show the results of the Monte Carlo simulations. Symbols and lines are as in Figure 1.4.2.

ellipticity (centered at 0.7 and with a dispersion of 0.2) and the anisotropy  $\beta$  parameter (centered at a mean value of 0.5 and with a dispersion of 0.1). The results of the simulation are shown in Figure 1.4.3. They are qualitatively consistent with the distribution of the *Fast Rotators*.

About 14% (36/260) of the galaxies are, on the other hand, *Slow Rotators*. They are typically massive ( $M_{\text{dyn}} > 10^{11} M_{\odot}$ ) and rather round systems ( $\epsilon_e < 0.04$ ), exhibiting central kinematical decoupled components. Four objects of lower mass ( $M_{\text{dyn}} < 10^{10.5} M_{\odot}$ ) are also found, which exhibit large-scale counter-rotating stellar disks.

Most massive *Slow Rotators* can represent the extreme tail of the red sequence galaxies for which significant merging has occurred where no cold stellar component could be re-established through dissipative processes. The possible processes involved in the formation and evolution of *Slow* and *Fast Rotators* are described in more detail in the following section.

## 1.5 Binary galaxy mergers and the formation of *Fast* and *Slow Rotators*

Bois et al. (2011) performed simulations of binary galaxy mergers in order to investigate the formation process of ETGs and compare the results with the observed 260 ATLAS<sup>3D</sup> galaxies kinematic properties. Seventy binary mergers between disk galaxies were simulated by varying the initial parameters (e.g. initial mass ratios from 1:1 to 6:1, initial conditions of the merger, and spins of the progenitors). In addition, sixteen binary merg-

ers between the merging remnants of the previous simulations were simulated, again varying the initial conditions.

Binary mergers can produce *Fast Rotators* for any initial mass ratio; while *Slow Rotators* can be formed only for mass ratios between 1:1 and 2:1. *Fast Rotators* never show kinematic distinct cores while most of the *Slow Rotators* do. In particular, the formation of a KDC not only appears connected to the initial mass ratio of the spiral-like progenitors, but also to the orientation of the initial spin axis of the progenitors with respect to the orbital angular momentum. Only a 1:1 merger with two retrograde progenitors (retrograde spin by respect to the orbital angular momentum) can form an intrinsically decoupled KDC. The amount of gas within a galaxy does not seem to affect significantly the kinematics of the remnant. With respect to the simulated re-merger events between ETGs-like remnants, they typically form objects classified as *Fast Rotators* or lying close to the dividing threshold between *Fast* and *Slow Rotators*. Possible KDCs in the progenitors tend to be destroyed during the re-merger event and are not recreated.

The kinematic features of the simulated *Fast Rotators* are close to those observed for the ATLAS<sup>3D</sup> galaxies, while some of the *Slow Rotators* can be associated to  $2\sigma$  ATLAS<sup>3D</sup> galaxies. All the other kinematic classes observed among ATLAS<sup>3D</sup> *Slow Rotators* are intrinsically rounder than any of the simulated merger remnants. A full cosmological context needs to be simulated to better reproduce the formation scenario of ETGs with special regard to *Slow Rotators*.

## 1.6 Modelling the formation and evolution of *Fast* and *Slow Rotators* within a $\Lambda$ CDM Cosmology

Khochfar et al. (2011) proposed a simple evolution model for *Fast* and *Slow Rotator* ETGs within a hierarchical  $\Lambda$ CDM scenario using the semi-analytical modelling approach. The difference between *Fast* and *Slow Rotators* was assumed to lie only in the mass fraction of the stellar disk: i.e. a *Fast Rotator* is assumed to be a galaxy with  $M_{disk}/M_* > 0.1$ . Indeed this assumption allowed to obtain a clear separation between the two galaxy categories, and the key event marking the final fate of a galaxy seems to be its ability to cool gas and rebuild a stellar disk. In agreement with the observations, *Slow Rotators* were mainly found to be galaxies with  $M_* > 10^{10.5} M_\odot$  representing  $\approx 20\%$  of the ETG population. For *Slow Rotators* a high fraction of the stellar mass (50% - 90%) is accreted from satellites, while their massive progenitors experience on average up to 3 major mergers. The last major merger for *Slow Rotators* was estimated to happen at  $z > 1.5$  and is followed by frequent minor mergers. *Fast Rotators*, on the other hand, are characterized by a lower fraction of accreted stellar mass (<50%) and by less than one major merger in their evolution history. The slowing down and/or the complete stop of the gas cooling in massive galaxies seems to be the key event for the formation of a *Slow Rotator*. When the cooling stops also the star formation in disks stops and the galaxy mainly accretes material via infall from satellites. Minor mergers are able to destroy the stellar disks via violent relaxation, and to lower the specific angular momentum of the stellar component.

The only opportunity to build a KDC was found to be during the last gas-rich major merger, then the following minor mergers build-up the envelope of the *Slow Rotator* and round its shape. Despite the clear separation between the two categories, the simulations

also showed that the two types of galaxies are transient: stellar disk growth or destruction by merger allows the galaxies to switch their state between fast and slow rotation. This is likely to happen more frequently at high redshift where gas cooling is more efficient and merging is more frequent.

## 1.7 The kinematic morphology-density relation

Cappellari et al. (2011) analyzed the morphology-density relation of local galaxies and revised the Hubble tuning-fork usually employed for the morphology classification of ETGs, using the entire ATLAS<sup>3D</sup> parent sample of 871 nearby galaxies. The main issues about the classic morphological classification concern the S0 class: S0 are considered as a transition class between the earliest type of spirals (Sa) and the ellipticals. Spitzer & Baade (1951) first reported that galaxies commonly classified as S0 “actually present a series of forms paralleling the series of normal spirals”. van den Bergh (1976) proposed a new trident-like classification scheme, in which S0a, S0b, S0c galaxies were introduced as a parallel series with respect to the spirals one. Due to the difficulty in the measurement of the flattening and bulge-fraction for non edge-on S0s, the classic Hubble scheme is however in general use. The kinematic information coming from the ATLAS<sup>3D</sup> sample, already provides a better classification of ETGs through the  $\lambda_R$  parameter, and is in good agreement with the findings of the aforementioned studies. Indeed, *Slow Rotators* are consistent with being purely elliptical-like objects with intrinsic  $\varepsilon \lesssim 0.4$ , and *Fast Rotators* usually have  $\varepsilon \gtrsim 0.4$  and morphologically resemble dust-poor spiral galaxies. *Fast Rotators* span the full range of bulge sizes of spirals and in some cases they look like flat ellipticals with disk isophotes. The revised Hubble tuning-fork scheme proposed by Cappellari et al. (2011) is shown in Figure 1.7.1.

Taking advantage of this new classification scheme, the morphology-density relation (Dressler 1980) was re-analyzed for the ATLAS<sup>3D</sup> parent sample. *Slow Rotators* are found to be nearly absent at the lowest densities and represent a  $\approx 4\%$  of the entire galaxy population in all the environments, with the exception of the Virgo Cluster Core. The formation process of *Slow Rotators* must therefore be inefficient in the field and in small groups.

A decrease of the spirals fraction, associated to an increase of the *Fast Rotator* ETG fraction was found as a function of the increasing galaxy surface density. Such trend is well described by a log-linear relation over nearly four orders of magnitudes of the galaxy surface density and is valid down to  $\Sigma_3 \approx 0.01 Mpc^{-2}$ .<sup>4</sup> The fact that such relation holds over a large range of galaxy densities suggests that processes taking place in cluster environments are unlikely to be the dominant ones in the apparent conversion from spirals to *Fast Rotator* ETGs. Using a less-local density estimator than the one previously described, the morphology-density relation becomes shallower and less well-defined. This suggests that the observed relation is driven by processes occurring at group-scale. Only in the largest density environments (like the Virgo Cluster Core) the decrease of spirals corresponds to an increase of *Slow Rotator* ETGs. Thus means that a different process must act in the densest environments. Hot gas and ram pressure stripping can transform

---

<sup>4</sup> $\Sigma_3$  is the surface density in  $Mpc^{-2}$  of galaxies inside a cylinder centered on a reference galaxy and containing its 3 nearest neighbours.

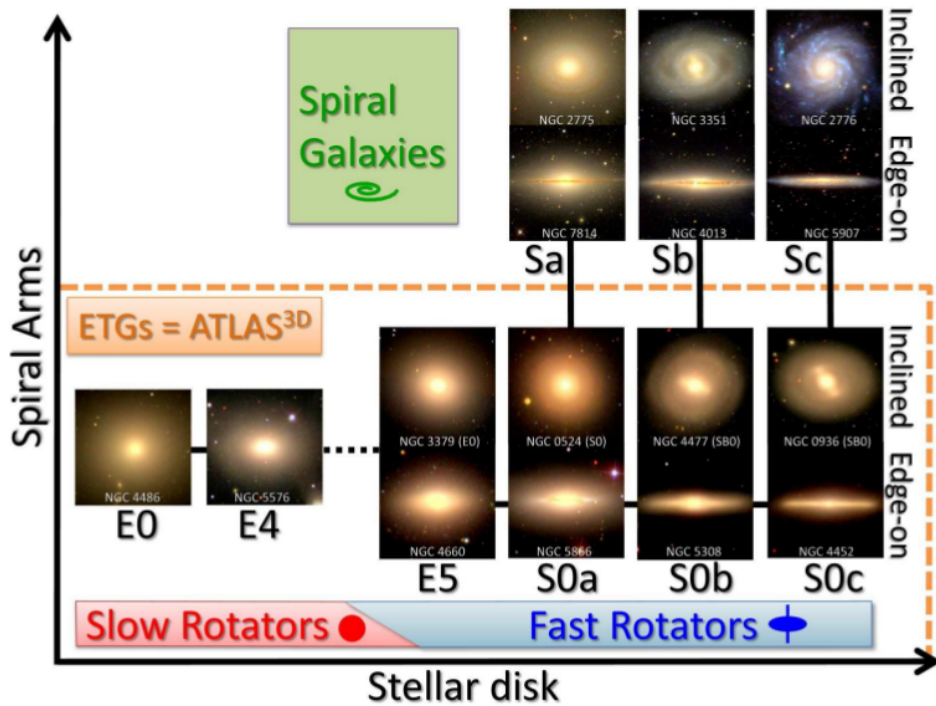


Figure 1.7.1: Morphology of nearby galaxies from the ATLAS<sup>3D</sup> parent sample. Edge-on *Fast Rotators* appear morphologically equivalent to S0s or flat ellipticals with disk isophotes. They form a parallel sequence to spiral galaxies. *Slow Rotators* are rounder ( $\epsilon \lesssim 0.4$ ) and mostly consistent with classical ellipticals. Solid black lines connecting galaxy panels indicate a possible empirical continuum, while dashes lines suggest a possible dichotomy.

spirals into anemic spirals and later into *Fast Rotator* ETGs, due to the lack of cold gas accretion. Later on, dry mergers would produce *Slow Rotators* and a subsequent large number of minor mergers can shape the galaxies to the morphologies currently observed.

## 1.8 Angular momentum and nuclear surface brightness profiles

Krajnović et al. (2013) derived the nuclear light profiles for 135 ATLAS<sup>3D</sup> galaxies and compared them to their kinematic properties in order to investigate if a correlation between the kinematic classification (*Slow* and *Fast Rotators*) and the nuclear profiles (core and coreless galaxies) obtained from HST imaging exists. Two classes of ETGs are commonly observed: core galaxies characterized by a flattening of the inner surface brightness profile and *power-law* galaxies that exhibit a steep rise in the surface brightness profile up to the HST resolution limit (0.1" or less). Faber et al. (1997) compared the nuclear light profile of a large sample of galaxies with their kinematic characteristics concluding that cores are found in luminous, boxy and slowly rotating galaxies, while power-law galaxies are less luminous disky and rapidly rotating objects.

The surface brightness profiles of the 135 ATLAS<sup>3D</sup> galaxies with HST observations were fitted by a “Nuker law” (Lauer et al. 1995):

$$I(r) = 2^{(\beta-\gamma)/\alpha} I_b \left(\frac{r_b}{r}\right)^\gamma \left[1 + \left(\frac{r}{r_b}\right)^\alpha\right]^{(\gamma-\beta)/\alpha} \quad (1.8.1)$$

where  $\gamma$  is the inner cusp slope and  $r_b$  is the so-called “break” radius at which the profile can change its slope. The galaxy profile classification is done by calculating the local logarithmic gradient of the luminosity profile at the HST angular resolution limit  $r'$  (typically 0.1"):

$$\gamma' = - \left. \frac{d \log I}{d \log r} \right|_{r=r'} = - \frac{\gamma + \beta (r'/r_b)^\alpha}{1 + (r'/r_b)^\alpha} \quad (1.8.2)$$

Core galaxies are those having  $\gamma' \leq 0.3$  while galaxies showing a steeper inner slope ( $\gamma' \geq 0.5$ ) are classified as *power-law*. When  $0.3 < \gamma' < 0.5$  the galaxies are referred to as *intermediate* type galaxies.

The largest part of the ATLAS<sup>3D</sup> galaxies (78/135 or 58%) was found to have power-law profiles, while the remaining part has core (24/135 or 18%) or intermediate (20/135 or 15%) profiles. For other 13 objects a certain classification could not be derived. All such galaxies have strong dust features in their nuclei that prevent from deriving a good profile fitting.

Galaxies with different nuclear slope overlap in luminosity, but a clear trend for brighter galaxies to have lower  $\gamma'$  slopes was found (see Figure 1.8.1, *top panel*). The mass dependence of the profile classification was also explored. As shown in Figure 1.8.1 (*bottom panel*) there is an overlap region in mass between  $\sim 8 \times 10^{10}$  and  $\sim 2 \times 10^{11} M_\odot$  with no core galaxies below and no power-law or intermediate galaxies (except one) above.

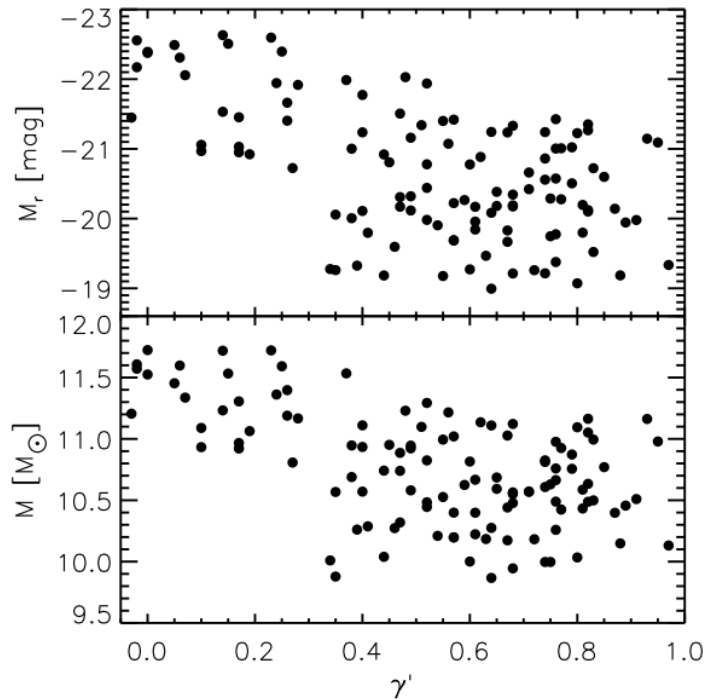


Figure 1.8.1: Distribution of the total r-band absolute magnitude (*top panel*) and of the dynamical mass (*bottom panel*) of ATLAS<sup>3D</sup> galaxies as a function of the calculated  $\gamma'$  inner slope of “Nuker” profiles.

In addition there seems to be a mass break at  $\gamma' \cong 0.3$  i.e. exactly at the dividing  $\gamma'$  value between core and core-less (power law and intermediate) galaxies.

The relation between galaxy mass and surface brightness profile was further explored in Figure 1.8.2 (*top panel*), when the  $\gamma'$  profile distribution is separately shown for massive ( $M > 2 \times 10^{11} M_{\odot}$ ) and less massive galaxies ( $M < 2 \times 10^{11} M_{\odot}$ ). Again we see that massive objects are always core galaxies, while core-less galaxies are associated with less massive systems. A very similar distribution was found for *Slow* and *Fast Rotators* (see Figure 1.8.2, *bottom panel*) indicating that the mass dichotomy corresponds also to a kinematic dichotomy. The latter, however, is less tight as there can be both core *Fast Rotators* and core-less *Slow Rotators*.

From the analysis of the  $\lambda_R - \varepsilon$  diagram (see Figure 1.8.3) it is clear that core *Fast Rotators* are mainly clustered around  $\varepsilon \sim 0.15$  and  $\lambda_R \sim 0.15$ , that is in a region where the isodensity contours of the simulated *Fast Rotators* show a marked deviation (see contours in *right panel*).

Figure 1.8.3 (*right panel*) also shows that galaxies with regular rotating structure can exhibit cores, and, similarly, core-less galaxies are possible in KDCs; remarkably non-rotating galaxies have always core profile. This indicates that plausibly core *Fast Rotators* experienced a different formation process with respect to the overall *Fast Rotator* population.

Galaxies with ordered rotation typically show an anti-correlation between the  $V/\sigma$  and  $h_3$ . This is true also for core *Fast Rotators*. *Slow Rotators*, on the other hand, never show such anti-correlation, this indicates that core *Fast Rotators* and *Slow Rotators* are really different despite the fact that core *Fast Rotators* lie close to the Fast/Slow dividing line.

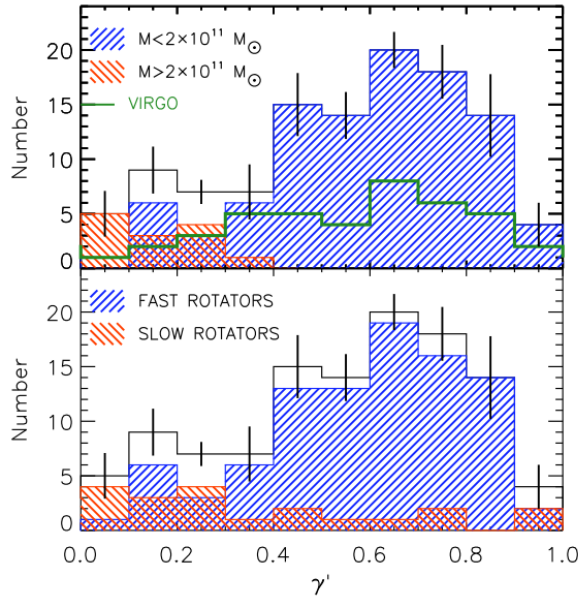


Figure 1.8.2: Distribution of the ATLAS<sup>3D</sup> galaxies as function of  $\gamma'$ . *Top panel*: galaxies are divided in two mass intervals as indicated in the plot. Virgo cluster galaxies are indicated by a green line. *Bottom panel*: galaxies are divided into *Fast* and *Slow Rotators*. Vertical bars represent systematic uncertainties.

As shown in Figure 1.8.4 core galaxies are found in massive and large ETGs. High mass *Slow Rotators* always have core profile. On the other hand, massive core-less *Fast Rotators* can exist. Both massive *Fast* and *Slow Rotators* ( $M > 8 \times 10^{10} M_{\odot}$ ), tend to be aligned along the lines of constant velocity dispersion. Various properties of ETGs remain constant along lines of constant  $\sigma$ . This is due to the fact that  $\sigma$  mainly traces the bulge fraction. A different distribution of the galaxies in the mass-size diagram appears thus related to a difference in the galaxy evolutionary process. Cappellari et al. (2012) suggested to two main processes:

- bulge growth which increases the galaxy  $\sigma$  and decrease  $R_e$
- dissipationless mergers which move the galaxies along lines of constant  $\sigma$ , increasing both  $R_e$  and  $M$ .

The majority of *Slow Rotators* and some core *Fast Rotators* are localized in the region of the diagram ( $M > 2 \times 10^{11} M_{\odot}$ ) that is expected to be dominated by evolutionary processes which do not change the  $\sigma$  of the galaxy but change its mass and size. Lower mass core galaxies ( $M < 2 \times 10^{11} M_{\odot}$ ), either classified as *Slow* or *Fast Rotators*, are in the regime where gas-rich processes also influence the evolution.

The Figure 1.8.5 shows the  $\lambda_R - \sigma_e$  diagram for core and core-less galaxies. It is interesting to note that core galaxies are clustered together in the lower right corner of the diagram, being characterized by  $\lambda_R \lesssim 0.25$  and  $\sigma_e \gtrsim 160 \text{ km s}^{-1}$ . In other words, core galaxies are typically found in galaxies with low specific angular momentum and high mass and the  $\lambda_R - \sigma_e$  diagram can be used as a good predictor to determine if a galaxy has a core profile.

The currently favoured scenario for the formation of cores is based on numerical models of binary black hole interactions: as black holes spiral down, the binary system loses its

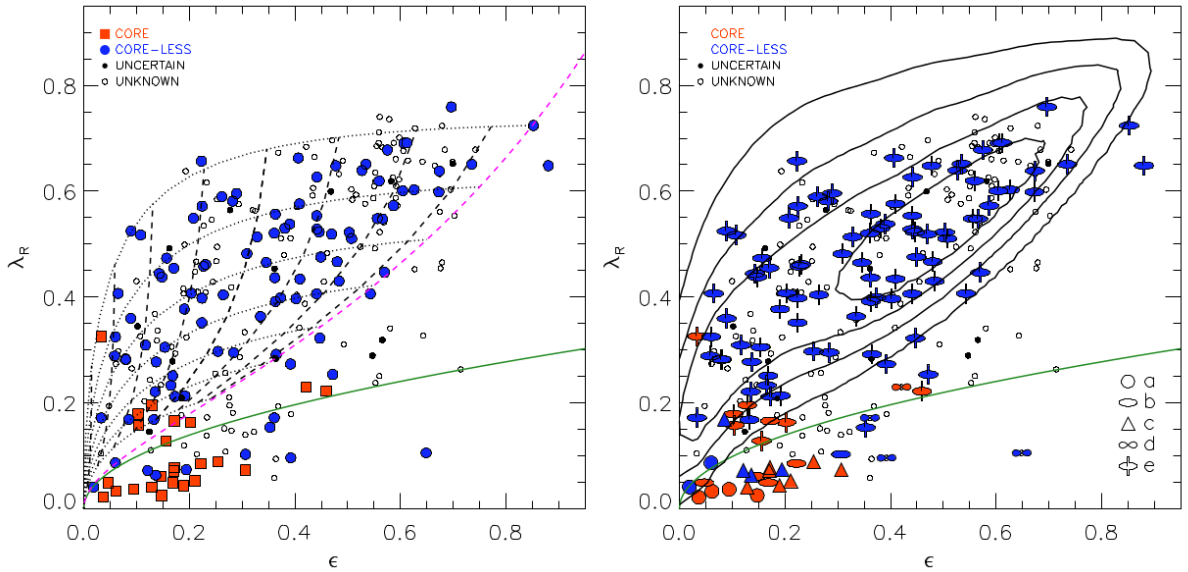


Figure 1.8.3:  $\lambda_R - \epsilon$  diagrams for the 260 ATLAS<sup>3D</sup> galaxies. *Left panel:* core and core-less galaxies are indicated with red and blue colors respectively, while the black filled symbols indicate uncertain classification category. Open circles indicate galaxies with no available HST images. The green solid line separates *Fast* and *Slow Rotators*. The dashed magenta line and the dotted black lines are as in Figure 1.4.1, the dashed black lines indicate the same relation of the magenta dashed line but for inclinations of 80°, 70°, 60°, 50°, 40°, 30°, 20° and 10° (from right to left). *Right panel:* the symbols indicate the kinematic group of the galaxy (as in Figure 1.4.2 and 1.4.3) while the contours show the distribution of a family of oblate objects with  $\epsilon_{intr} = 0.7 \pm 0.2$  as in Figure 1.4.3.

angular momentum by ejecting nearby stars and originates a core in the inner part of the galaxy. An equal mass merger is needed in order to guarantee a rapid evolution. If the merger event involves significant quantities of gas it is likely that the galaxy core will be again filled of stars created by the resulting star-burst events, preventing the formation of the core profile. An alternative scenario involves a rapid mass loss (due e.g. to supernovae feedback or AGN activity) in the galaxy nucleus that redistributes stars and flattens the central light profile.

Krajnović et al. (2013) concluded that major gas-poor mergers together with black hole binary evolution are not the only path that yields the formation of cores in ETGs. Different processes are probably involved in the formation and evolution of ETGs for the different combinations of profile/rotation galaxy properties, as summarized in Figure 1.8.6.

## 1.9 The ionized gas kinematics

The potentiality of the ionized gas kinematics study is illustrated through the main findings of Sarzi et al. (2006) on the SAURON project, while the ionized gas properties of the ATLAS<sup>3D</sup> sample are reported in Section 1.11 focusing on the misalignments of this component with respect to the molecular gas and the stellar population.

The ionized-gas kinematics was extracted from 48 SAURON ETGs using an improved

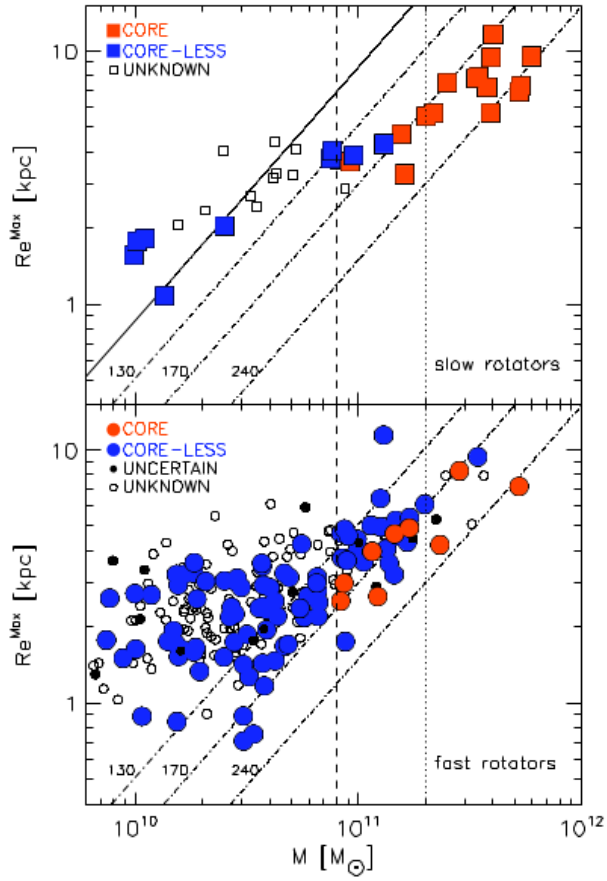


Figure 1.8.4: Mass-size diagram for ATLAS<sup>3D</sup> sources for Slow (*top*) and Fast (*bottom*) Rotators. Core and core-less galaxies are shown in red and blue respectively. Vertical lines mark the characteristic masses of  $0.8$  and  $2 \times 10^{11} M_{\odot}$  (see text); dashed-dotted lines indicate constant  $\sigma_e = 130, 170$  and  $240 \text{ km s}^{-1}$ .

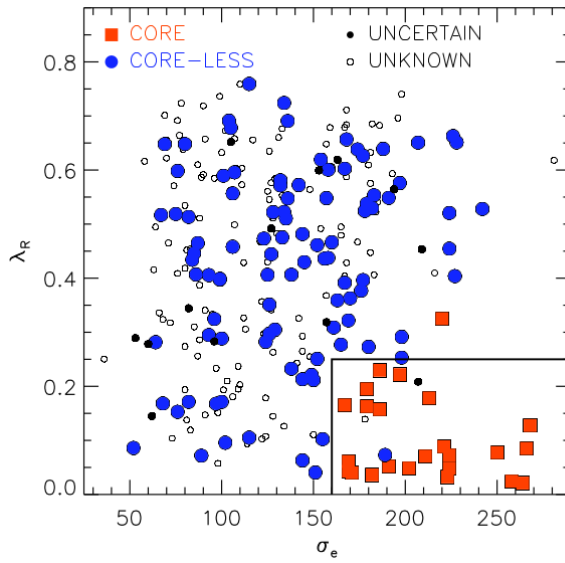


Figure 1.8.5: The parameter  $\lambda_R$  is plotted as a function of the velocity dispersion  $\sigma_e$ . Core galaxies are indicated with red squares, core-less galaxies with blue circles. Galaxies with uncertain nuclear profiles are indicated by filled black circles, galaxies with no HST data by open black circles. The region where most core galaxies are found is also indicated.

	CORE	CORE-LESS
FAST	<p><b>MERGER TYPE:</b></p> <ul style="list-style-type: none"> <li>•Dissipative major &amp; minor</li> <li>•Dissipationless minor</li> </ul> <p><b>CORE GROWTH/PRESERVATION:</b></p> <ul style="list-style-type: none"> <li>•BH binaries (longer duration than nuclear starburst)</li> <li>•Regulation of nuclear star formation (AGN feedback, morphological quenching)</li> </ul>	<p><b>MERGER TYPE:</b></p> <ul style="list-style-type: none"> <li>•Dissipative (range in mass fractions and amounts of gas)</li> </ul> <p><b>CUSP GROWTH:</b></p> <ul style="list-style-type: none"> <li>•Nuclear starburst</li> <li>•Subsequent interaction between BH and surrounding stars</li> </ul>
SLOW	<p><b>MERGER TYPE:</b></p> <ul style="list-style-type: none"> <li>•Dissipationless major &amp; multiple minor</li> </ul> <p><b>CORE GROWTH/PRESERVATION:</b></p> <ul style="list-style-type: none"> <li>•BH binaries</li> <li>•AGN induced</li> <li>•Adiabatic expansion</li> <li>•Hot halo gas</li> </ul>	<p><b>MERGER TYPE:</b></p> <ul style="list-style-type: none"> <li>•Dissipative major (retrograde orbits)</li> <li>•Accretion of gas</li> </ul> <p><b>CUSP GROWTH:</b></p> <ul style="list-style-type: none"> <li>•Nuclear starburst (refilling of existing core)</li> </ul>

Figure 1.8.6: Dominant processes that could shape the angular momentum of a host galaxy and its nuclear profile.

method, that simultaneously fits the stellar and ionized-gas components. The ionized gas emission lines could be detected down to an equivalent width (EW) of 0.1 Å. The reported errors on  $V_{gas}$  and  $\sigma_{gas}$  are respectively 14 and 20 km s<sup>-1</sup>, while for the flux of the H $\beta$  and [OIII] lines the uncertainty is on average 10% and 20% respectively. With only 5 objects not showing significant gas emission and 9 objects with faint or fragmented emission, the detection rate is 75% (33/48 galaxies). Two main classes of objects could be recognized. On the one hand there are objects with settled gaseous systems for which the gas kinematics is very regular and disk-like. Such objects show dust lanes and low [OIII]/H $\beta$  ratios, typically associated with occurring star formation. On the other hand there are objects showing loosely wound spiral features in the ionized-gas distribution and twists in the velocity maps. Despite the presence of complex structures in the extracted velocity maps, the gas generally shows smooth variations in angular momentum.

Measurements of the kinematic misalignment between the gas and the stars can shed light on the origin of the gas. The gas kinematics was found to be frequently decoupled from the stellar one. This however does not necessarily imply a purely external origin of the gas. The misalignments do not show trends with respect to either the galaxy Hubble type, the galactic environment or the galaxy luminosity; on the other hand they are strongly dependent on the apparent galaxy flattening. In principle the metallicity of the ISM can provide an additional constraint on the gas origin. If the gas is originated by stellar mass loss, the metallicity of the gas and that of the stellar population must be similar. However, to derive the metallicity, the ionizing source of the gas must be known. The heterogeneous values of the [OIII]/H $\beta$  ratios suggest a variety of mechanisms responsible for the gas excitation. The spectral classification of the galaxies is often consistent with LINER type, with [OIII]/H $\beta$  central gradients reaching values between 1 and 3. Other emission-line diagnostics are however needed to perform a better spectral classification of the galaxies.

Assuming the gas emission is not AGN-powered, several processes can produce gas ionization: shocks, thermal conduction and both young and post-Asymptotic Giant Branch (AGB) stars. Post-AGB stars are however the most likely candidates for the gas ionization, due to the good correlation between emission-line fluxes and stellar luminosities, as derived in the wavelength region of the emission lines themselves.

## 1.10 The cold gas content of ATLAS<sup>3D</sup> early-type galaxies

The cold gas content is tightly connected to the red sequence formation, due to the fact that it has to be depleted or made unsuitable for star formation, in order to allow the transition of a galaxy onto the red sequence. A major merger between two gas-rich galaxies is able to drive a large-scale loss of angular momentum dropping the gas to the centre of the merger remnant (Barnes 2002). Here the gas can fuel the black hole and/or be consumed in a star formation burst. Alternatively, an energy input into the Inter-Stellar Medium (ISM) from AGN activity or starburst could destroy and/or unbind the cold gas and/or prevent the hot gas from cooling. In addition, environmental effects have to be taken in account. Today it is well known that ETGs are not completely devoid of cold gas, however its origin is not well understood: in some cases the external origin of

the cold gas is very clear, due to a remarkable difference between the specific angular momentum of the gas and that of stars, while in other cases the gas kinematics are consistent with an internal origin (e.g. stellar mass loss). The connection of the cold gas to kinematic structures present in the galaxies and the influence of AGN activity and/or local environment appear therefore a key issues to better understand the formation history of ETGs. Young et al. (2010) studied the molecular gas content of ETGs through CO line observations of 259 of the 260 objects of the ATLAS<sup>3D</sup> sample. The 259 ATLAS<sup>3D</sup> galaxies were searched for <sup>12</sup>CO J=1-0 and J=2-1 emission with the IRAM 30m telescope. The observations are sensitive to H<sub>2</sub> masses of  $\gtrsim 10^7 M_{\odot}$  for nearby sample members ( $\leq 11$  Mpc) and to H<sub>2</sub> masses  $\gtrsim 10^8 M_{\odot}$  for most distant objects ( $\sim 40$  Mpc). For undetected galaxies  $3\sigma$  upper limits were calculated assuming linewidths of  $300 \text{ km s}^{-1}$ . H<sub>2</sub> masses were calculated following the equation:

$$\frac{M(H_2)}{M_{\odot}} = 6.0 \times 10^4 \left( \frac{D}{\text{Mpc}} \right)^2 \left( \frac{\int T_{mb} dv}{K \text{ km s}^{-1}} \right) \quad (1.10.1)$$

where D is the distance in Mpc and  $\int T_{mb} dv$  is the CO line intensity.

The CO detection rate is  $22 \pm 3\%$  (56/259), this has to be considered as a lower limit mainly due to three effects: 1) the molecular gas outside the central  $22''$  is not probed by the IRAM 30m CO(1-0) beam; 2) the measurements could be incomplete for linewidths much greater than  $300 \text{ km s}^{-1}$ ; and 3) very compact distributions may suffer strong beam dilution. The H<sub>2</sub> masses derived from the detected galaxies range from  $10^{7.1}$  to  $10^{9.3} M_{\odot}$ .

Molecular gas is often consistent with regular rotating disks, due to the observed double horn and/or asymmetric line profiles.

The molecular surface densities, averaged over the inner 2 or 4 kpc of the galaxies, are comparable to those in spiral galaxies. Some molecular masses are surprisingly high, reaching values greater than  $10^9 M_{\odot}$  in three particular cases.

The molecular gas content is expected to be correlated with dust, blue features and young stellar populations; the CO detection rate is indeed higher in galaxies with gas disks, dusty filaments or blue regions ( $77 \pm 6\%$ , 37/48). As shown in Figure 1.10.1 galaxies with significant amount of molecular gas also have evidence of young stars, as traced by the H $\beta$  absorption line strength index, indicating that the molecular gas does fuel star formation processes.

The relation between  $M(H_2)$  and H $\beta$  absorption strength is not tight. This probably reflects the difference between the two tracers. The H<sub>2</sub> mass should indeed trace instantaneous star-formation activity, while H $\beta$  traces a age weighted average star formation rate biased towards recent star-formation events. Another intriguing hypothesis is that the molecular gas reservoir is prevented from forming stars in some galaxies due to an ongoing heating process (e.g. AGN activity).

The CO detection rate is not a function of stellar luminosity over the range  $-21.5 \geq M_K \geq -26$  and the H<sub>2</sub> mass distribution does not seem to be correlated to stellar luminosity.

The lack of correlation between H<sub>2</sub> mass and stellar luminosity has often be interpreted as a feature indicating that the gas is unrelated to internal mass loss. However, if the mass loss material is heated in some way, (through environmental and/or feedback effects) it appears difficult to predict how much of it might be able to cool and re-form molecules.

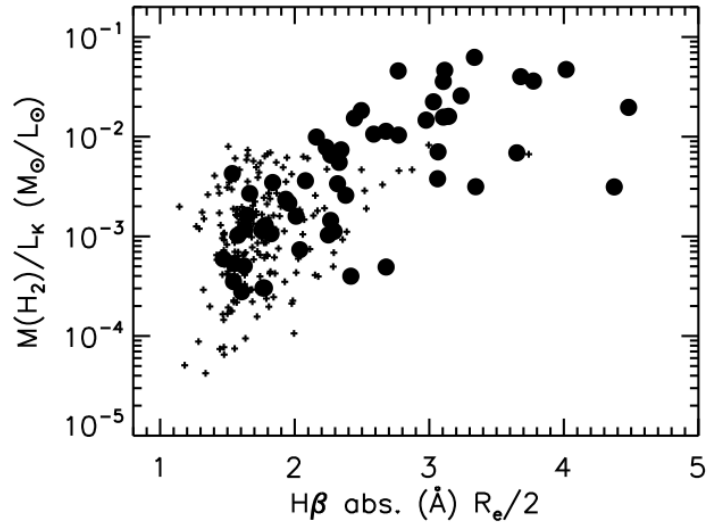


Figure 1.10.1: Molecular mass normalised for the  $L_K$  luminosity plotted as a function of  $H\beta$  line strength. Small crosses correspond to undetected ATLAS<sup>3D</sup> galaxies ( $M_{H_2}$   $3\sigma$  upper limits) and large filled circles indicate CO detected galaxies.

Thus, it is not possible to infer the internal or external origin of the gas, just from the presence or absence of a  $M(H_2)$ - $M_K$  relation.

On the other hand, the CO detection rate appears also strongly correlated with the star specific angular momentum. *Slow Rotators* are typically less rich in molecular gas than *Fast Rotators*. In other words, the molecular gas seems more tied to the kinematics of a galaxy than to its stellar mass.

Using interferometric HI observations Oosterloo et al. (2010) argued that ongoing accretion of cold atomic gas is quite common for field ETGs. In some cases the atomic gas is found in the central few kpc of the galaxy, in correspondance of the molecular disk. It was therefore argued that at least a part of the molecular gas can be accreted in form of atomic gas, settling in a regular disk, and then converted into molecular gas as its density increases. Assuming the gas has an internal origin, one would expect that mass loss related material should retain some memory of the specific angular momentum of the stars that expelled it. A slowly rotating system implies thus a compact molecular gas disk. This means that the gas is more likely to have dropped to the nucleus, where it gets consumed. On the other hand, kpc-scale disk is more likely to be formed in fast-rotating galaxies. Alternatively, if the formation process of *Fast* and *Slow Rotators* is assumed to be different, a formation scenario that inevitably destroys or removes the molecular gas, can explain the lack of cold gas for *Slow Rotators* content.

Serra et al. (2012) studied the HI properties of 166 ETGs of the ATLAS<sup>3D</sup> sample, using data taken with the Westerbork Synthesis Radio Telescope and were able to detect HI down to  $5 \times 10^6$ - $5 \times 10^7 M_\odot$  within the survey volume. The HI detection rate appears to be strongly dependent on the environment density: the detection rate in the Virgo cluster is  $10 \pm 5\%$  while in the field is  $39 \pm 6\%$ . In the majority of the cases, the gas is settled in the form of regular rotating disks or rings, although also unsettled configurations and gas clouds not associated to the galaxy are found. The variety of gas morphologies could be related to different times since the last major episode of gas accretion or stripping.

Regular rotating systems are divided in two classes: large disks/rings (containing  $10^8$ - $10^{10} M_{\odot}$  of gas out to tens of kpc) with equal probability to be aligned or misaligned with respect to the stellar component; small disks (with typically  $M_{H_2} < 10^8 M_{\odot}$ ) which are kinematically aligned to the stellar component. The HI gas seems to be related to star formation. HI detected galaxies which show a high concentration of HI within  $\sim 1R_e$ , exhibit signatures of on-going star formation in  $\sim 70$  percent of the cases, about 5 times more frequently than galaxies with no HI in their centres. The ISM in the centre of these galaxies appears however to be dominated by molecular gas. The morphology-density relation found for the HI appears to confirm the crucial importance of processes on galaxy-group scale, as already noted by Cappellari et al. (2011).

## 1.11 On the origin of the molecular and ionized gas in ATLAS<sup>3D</sup> early-type galaxies

Davies et al. (2011) investigated the origin of the molecular and ionized gas in the ETGs of the ATLAS<sup>3D</sup> sample. In the standard hierarchical scenario it is usually assumed that ETGs join and remain on the red sequence due to the lack of cold gas. However a sizable cold gas reservoir is often present in ATLAS<sup>3D</sup> galaxies. On the other hand the stellar population in these galaxies is old ( $\gg 1Gyr$ ), and the stellar kinematics of the majority of ETGs in the ATLAS<sup>3D</sup> sample is typically relaxed. Both evidences point toward a scenario where the last major merger originating such systems occurred several Gyrs ago. The cold gas reservoir seen today has therefore two possible origins: it is either regenerated and/or reacquired, or alternatively it is stable against star formation.

The regeneration of cold gas is possible through *internal* stellar mass loss. Such process should be occurring in ETGs at all times, and therefore molecular gas should be observed in many of such galaxies. However, the measured CO detection rate in ATLAS<sup>3D</sup> galaxies seems to exclude that this process is the dominant one.

Alternatively, galaxies can reacquire cold gas via an *external* process like merging and/or cold accretion mode from the Inter Galactic Medium (IGM). Minor mergers or cold accretion do not shock all the gas during an event; a gas fraction can indeed fall to the centre of the galaxy and cool. In major mergers the ejected gas can be reacquired over the course of cosmic time.

A different scenario has been proposed to explain the presence of cold gas: the so-called “morphological quenching” (Martig et al. 2009). When they are formed, red sequence galaxies do not lose/consume entirely the cold ISM component, but a fraction of it becomes stable against gravitational collapse. In this way a low star formation rate can favour the persistence of this gas for many billion years.

To probe such scenarios, Davies et al. (2011) searched for angular momentum alignments or misalignments between the ISM and the underlying stellar population. Stellar mass loss should produce gas which is kinematically aligned with the stellar component. External accretion on the other hand, should produce at least, at first order, a kinematically misaligned gas component. The data analysis by Davies et al. (2011) includes stellar and ionized gas velocity maps from SAURON optical IFS, CO kinematics maps (CARMA and literature data), and HI velocity maps from WSRT. Such analysis was carried out for the brightest  $\approx 2/3$  of the ATLAS<sup>3D</sup> sample CO detections (36/56 galaxies). The

kinematic position angle  $\phi$  was derived for stars, ionized gas and molecular gas. The misalignment between the three components was quantified through the difference of the relative PA following the equations:

$$\psi_{mol-star} \equiv |\phi_{moleculargas} - \phi_{star}| \quad (1.11.1)$$

$$\psi_{mol-ion} \equiv |\phi_{moleculargas} - \phi_{ionizedgas}| \quad (1.11.2)$$

$$\psi_{ion-star} \equiv |\phi_{ionizedgas} - \phi_{star}| \quad (1.11.3)$$

The main findings are summarized below:

- Molecular gas and stars. Two populations are present:  $24 \pm 7\%$  of the galaxies have their molecular gas misaligned ( $\Psi > 30^\circ$ ) with respect to stars, while for  $76 \pm 7\%$  of the galaxies a  $\Psi < 30^\circ$  is reported consistent with an internal origin.
- Molecular gas and ionized gas. The two components have always smaller misalignments than  $\Psi = 40^\circ$  and generally much lower than this. The kinematic alignment points towards a common origin.
- Ionized gas and stars. The ionized gas detection rate for the ATLAS<sup>3D</sup> sample is  $\approx 73 \pm 3\%$  and  $\approx 47 \pm 6\%$  in the field and in the Virgo cluster respectively. *Slow Rotators* display a flat distribution of misalignments (Figure 1.11.1) that suggests an external origin for the ionized gas (merger and/or accretion). For *Fast Rotators* a  $\Psi > 30^\circ$  is reported only for  $36 \pm 5\%$  of the galaxies (Figure 1.11.2).

The analysis of HI shows that atomic and molecular gas are always kinematically aligned, and 38% of the HI detected galaxies with gas kinematically aligned with stars shows HI disturbed structures at large radii suggesting an ongoing accretion.

In general, the ionized, atomic and molecular gas components appear to have similar kinematics in local ETGs. This is probably the proof of their common origin. In the field  $\approx 42\%$  of galaxies show kinematic misalignments for the ionized gas component confirming a key role of mergers and accretion. In the Virgo cluster, the molecular and ionized gas is often kinematically aligned with the star components in line with an internal origin. Another interesting result is that most massive *Fast Rotators* always show ionized and molecular gas aligned with the star velocity field, independently of environment. This suggests a galaxy scale process (e.g. AGN feedback, the presence of a hot X-ray gas halo, or a halo mass threshold) as a proxy for the alignment and supports the picture that fast-rotating ETGs have a different formation process from slow-rotating ones. However, the various scenarios to which the environmental dichotomy could be ascribed cannot relate the kinematic misalignments with the constant CO detection rate observed inside and outside cluster environment.

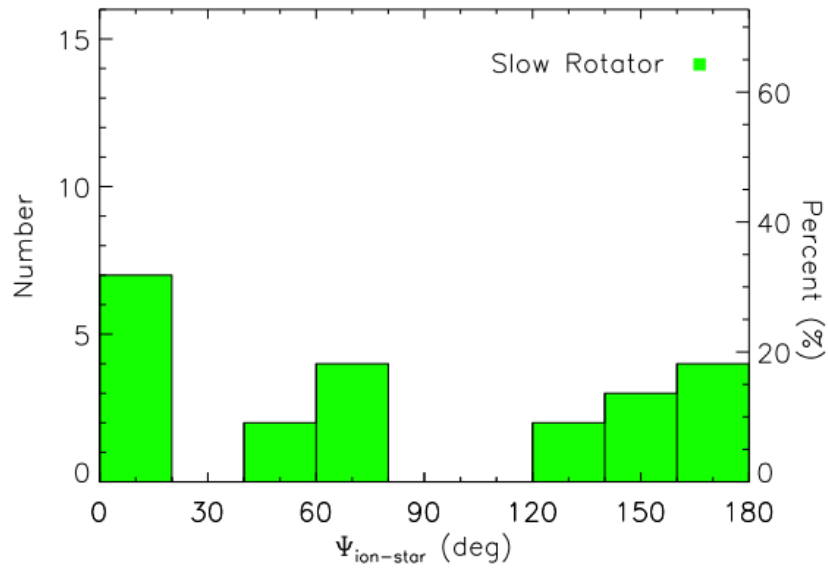


Figure 1.11.1: Histogram for the kinematic misalignment angle between ionized gas and star for *Slow Rotators* with measurable kinematic misalignments.

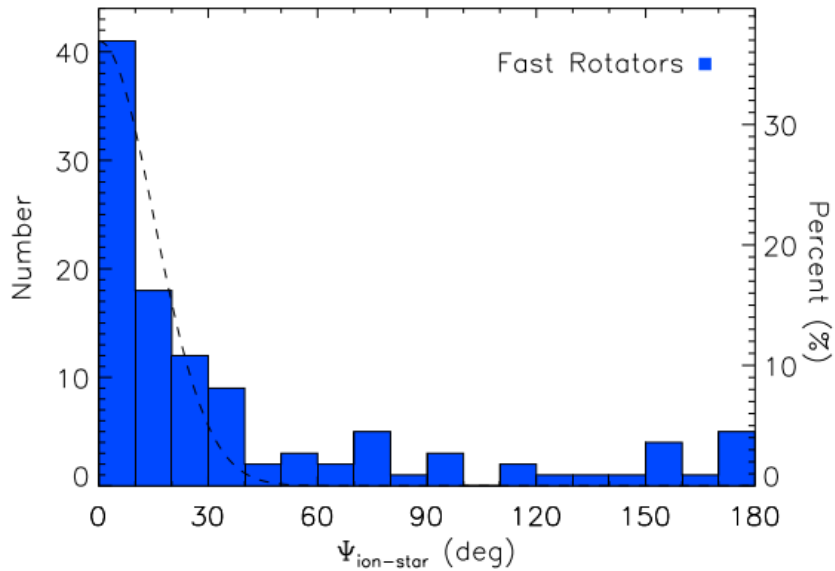


Figure 1.11.2: Histogram for the kinematic misalignment angle between ionized gas and star components for *Fast Rotators*. The overplotted dashed line is a normalized Gaussian distribution with zero centre and a standard deviation of  $15^\circ$ .

# Chapter 2

## Linking radio-loud to radio-quiet Early-type Galaxies

This thesis is part of an international project (involving INAF-IRA, ESO and Oxford University) aimed at extending the analysis of the warm and cold gas and stellar properties to radio-loud early type galaxies, mainly associated to radio galaxy phenomenon. In particular this project is focused on *low power* ( $<10^{25}$  W Hz<sup>-1</sup>) radio galaxies, for which a clear picture is still missing of their formation/accretion scenario.

In the following we present the general scientific framework of this project, the radio galaxy sample on which we are focusing our analysis, the current status of the observations, and the results obtained so far. Finally we introduce the source (NGC 3557) selected for the VIMOS/IFU analysis carried out as part of this thesis.

### 2.1 AGN classification and radio galaxies

The term “Active Galactic Nucleus” (AGN) generally indicates an extremely energetic phenomenon in the nucleus, or in the central region, of a galaxy.

The basic structure of an AGN is listed below.

- A central *black hole* (BH) with mass ranging from  $10^6 M_{\odot}$  up to  $10^{9-10} M_{\odot}$ , probably spinning at some level.
- An *accretion disk* formed by matter attracted by the gravitational potential of the BH.
- A *corona* sandwiching the accretion disk and particularly active in emitting X-ray light.
- A region filled by small clouds distant less than one parsec from the BH. This is the so-called *Broad Line Region (BLR)*. It absorbs  $\sim 10\%$  of the radiation from the disk and re-emits it in the form of emission lines with typical velocity dispersions of  $\sim 3000$  km s<sup>-1</sup>.
- An obscuring *torus* located at several parsec from the BH, that reprocesses part of the nuclear radiation and re-emits it in the infrared band.

- A more distant region ( $\sim 100$  pc) where less densely sparsed clouds are moving with characteristic velocities of  $\sim 300\text{-}500$  km s $^{-1}$  named *Narrow Line Region (NLR)*.
- Two opposites *jets* (observed in  $\sim 10\%$  of AGNs) tracing the rotational axis of the BH and expelling matter at relativistic speeds. AGNs whose jets are pointing at us are called *blazars*. When the jets point elsewhere the AGN is indicated with the name of *Radio Galaxy (RG)*.

It should be noted that the emission lines coming from the *BLR* are usually originated by permitted transitions, the most relevant belonging to Balmer and Lyman Hydrogen series. The *NLR* emits both forbidden and permitted lines, the most evident among the former being the lines produced by ionized Oxygen and Neon.

There is a large diversity in the observed properties of AGNs. A basic classification scheme divides AGN in radio-loud and radio-quiet depending on their radio properties.

Radio-loud AGNs show two collimated jets of plasma feeding extended lobes or a halo, both emitting in the radio continuum. On the other hand, radio-quiet AGNs show weak or no large scale jets.

According to the Unification Model (Antonucci (1993), Urry & Padovani (1995)) the observed AGN properties depend on the inclination of the system with respect to the line of sight to the observer. When the observing angle is large the torus hides the emission from the inner parts of the system including the BLR. Only the NLR is visible and the object is classified as a Type 2 AGN. When the AGN is viewed at intermediate inclination the inner regions, together with the NLR is visible and the AGN is classified as a Type 1 object. A schematic representation of the classification is shown in Figure 2.1.1, where different terminology is used depending on whether the AGN is radio-loud or radio-quiet. In the following we focus on radio galaxies which are the subject of the present thesis.

The classic scheme of a radio galaxy includes the following components:

- Radio Lobes, extended structures with almost elliptical shape and symmetrical locations with respect to the central object. The distance of the lobes spans from few kpc up to 1 Mpc and their luminosity usually decreases going from the edges to the centre.
- Hot Spots, regions with little extension and higher luminosity compared with the lobes. The hot spots usually marks the end point of a well collimated jet for a high power radio galaxy.
- Core, central compact component that usually gives little contribution to the overall radio emission. Its contribution is typically larger in *low power* radio-galaxies.
- Jets, elongated and narrow structures typically starting from the core. Their end is marked by the hot spots where the material, expelled from the core and funneled by the jets, hits the surrounding medium. The appearance of the jets depends on their radiative efficiency. A well collimated jet does not show large radiative losses, and virtually all the energy is channeled toward the hot spot, while a radiative efficient jet loses a large amount of its energy on its way and is generally associated to weak or no hot spot.

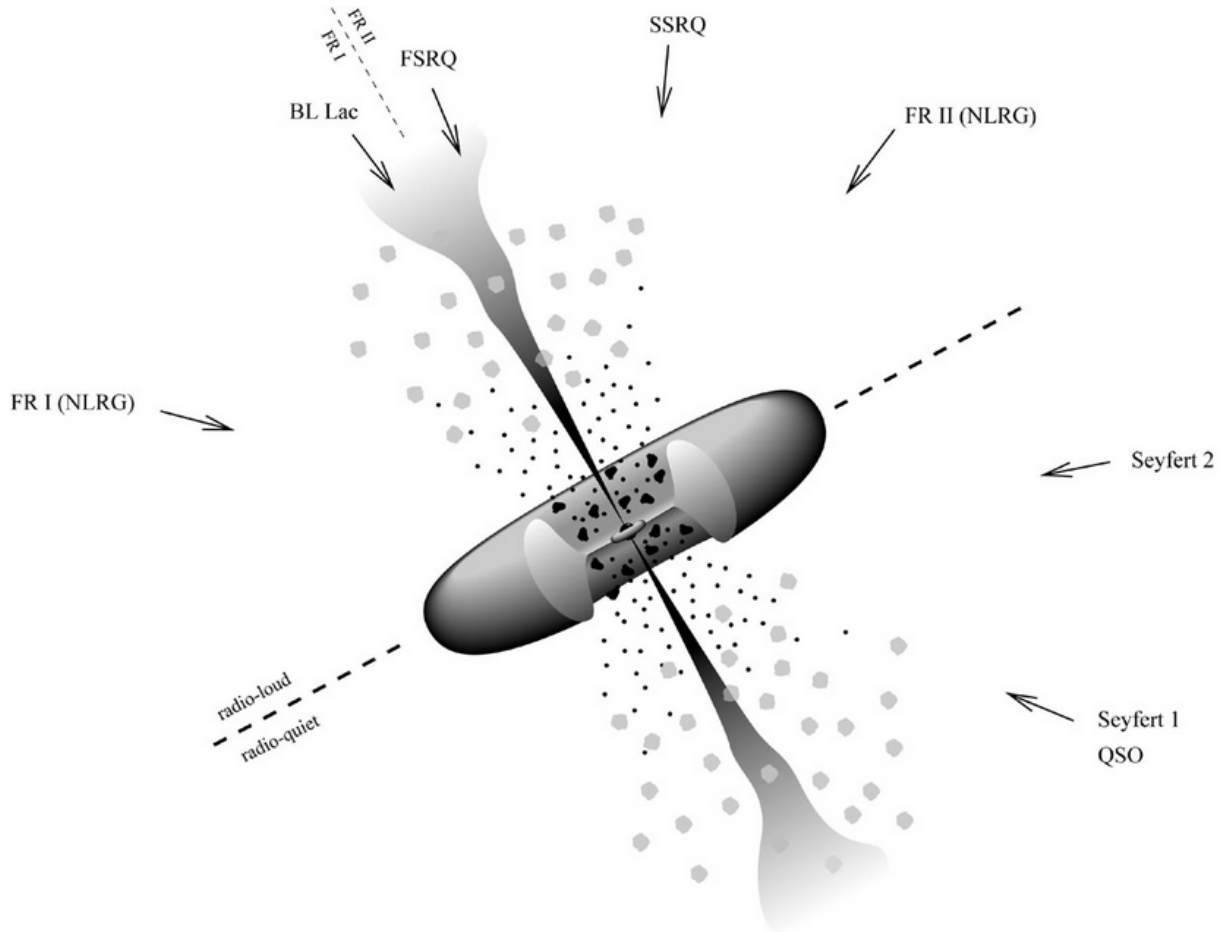


Figure 2.1.1: The unification model for AGNs. Blazars are those AGNs for which the jets are close to line of sight. They are divided in BL Lacertae objects (BL Lac) and Flat Spectrum Radio Quasar (FSRQ). A regular quasar (QSO), a Steep Spectrum Radio QSO (SSRQ) or a Seyfert 1 galaxy is observed if the orientation angle is  $\sim 30^\circ$ , where both the narrow-line and broad-line regions are visible. At larger angular offsets, the broad-line region is hidden by the torus, and the corresponding class is called Seyfert 2 galaxies. Perpendicular to the jet axis, the full extent of the jets (when present) may be seen, giving rise to a morphology typical of radio galaxies (RG).

Radio galaxies are generally hosted by ellipticals and/or S0 galaxies.

Fanaroff & Riley (1974) divided the radio galaxies in two classes, now known with the names of FRI and FR II. The classification was initially performed looking at the morphology of the large-scale radio emission, in particular they looked at the distance between the brightest points in the radio emission. FRI sources appear brighter toward the centre (edge-darkened), while FR II are brighter at the edges (edge-brightened). Fanaroff & Riley (1974) furthermore noted that the two classes were characterized by different luminosities. Sources with luminosity  $L(178 \text{ MHz}) \lesssim 2 \times 10^{25} \text{ W Hz}^{-1} \text{ sr}^{-1}$  were generally FRI, while brighter sources were FR II.

FRI and FR II types seems to be related also to different environments. In the nearby universe ( $z < 0.5$ ) FRI RGs are more often located in dense environments (e.g. galaxy groups and clusters) while FR II RGs are often hosted by field galaxies. At larger redshifts both types are found in rich environments (Hill & Lilly 1991). The galaxies hosting FR II are typically bluer than the hosts of FRI RGs and often shows signs of mergers (e.g. Ramos-Almeida et al. 2012). On the other hand, the host galaxies of FRI RGs are found to be more massive (Govoni et al. 2000) than FR II hosts. An important development in this area was represented by the Owen-Ledlow diagram (Owen 1993, Owen & Ledlow 1994), where FRI and FR II types are plotted in the total radio power versus host optical luminosity plane. The radio power is assumed to be representative of the jet energy while the optical luminosity of the host galaxy is related to its mass, and so to the ambient pressure in which the jets propagate. The diagram shows that for higher ambient pressures (and hence for more luminous elliptical galaxies) the FR-I/II jet transition occurs at higher radio power jet energy. This finding was crucial in determining the role of the ambient in producing the two different radio source morphologies.

Other studies have been carried out in order investigate FRI and FR II RGs properties, and in particular in their optical spectra (Laing et al. 1994, Buttiglione et al. 2010). The two morphological types clearly show different behaviour. The FRI radio galaxies hosts typically exhibit optical spectra with absorption lines and/or low  $\text{O[III]} / \text{H}\alpha$  ratios ( $< 0.2$ ). Following the classification of Laing et al. (1994) these galaxies are classified as Low Ionization Emission Line Radio Galaxies (LERGs). On the other hand, FR II host galaxies appear as a mixed class: they can show either FRI-like features or spectra with strong high ionization emission lines characterized by  $\text{O[III]} / \text{H}\alpha > 0.2$  (High Ionization Emission line Radio Galaxies, HERGs).

Baum et al. (1992, 1995) observed that most FR II RGs appear to have a rotating disk of line-emitting gas on large scales, while this was not found to be the case in FRI RGs. The favoured model links the morphological type to a different accretion rate. High resolution optical imaging with HST (e.g. Chiaberge et al. 2002) revealed unobscured, radiatively inefficient accretion disks for FRI RGs and, again, mixed characteristics for the FR II RGs. The latter show both FRI-like disks or radiatively efficient accretion disks, together with dust torii.

## 2.2 Gas accretion in Radio Galaxies: the LERG and HERG paradigms

It is commonly believed that the AGNs are powered by accretion of the interstellar medium (ISM) onto super massive black hole (SMBH) (Antonucci 1993, Urry & Padovani 1995). Recent studies have propose a different source for accreting gas for low and high accretion rate systems. Allen et al. (2006) suggested that accretion in LERGs located in the centre of clusters may be attributed directly to the hot phase of the intra cluster medium (ICM). Such systems are also known to accrete in a radiatively inefficient way. Hardcastle et al. (2007) confirmed that LERGs may be powered by Bondi accretion (spherical accretion of the hot X-ray emitting ICM) but an extra gas component (cold gas) is needed for HERGs, i.e. radio sources typically classified as FR II and with prominent optical emission lines, which accrete in a radiatively efficient way.

X-ray and IR-band observations (e.g. Best & Heckman 2012) together with optical spectroscopic studies (Buttiglione et al. 2010, Mahony et al. 2011) further support the division of radio galaxies based on line ratios and, again, link the two classes to different accretion modes and fuel sources. LERGs appear more likely to accrete hot gas at low accretion rates; the origin of the hot gas is suggested to be the hot corona of the hosts and the gas deriving from the stellar mass loss in the host galaxy. On the other hand, an efficient accretion of cold gas is supposed to characterize the HERGs; the cold gas is likely to be originated from a gas-rich mergers

It should be noted however, that the Bondi mechanism is rather unrealistic, since it assumes a perfectly spherical symmetric accretion. In addition cold gas is often found in large amounts in both high and low luminosity RGs and is detectable via emission and absorption in the form of dust, HI and CO in their cores.

The cold gas is often associated to dusty disks and can be clearly seen in high resolution HST images (e.g. de Ruiter et al. 2002). Dust is observed in 53% of the B2 sample of nearby, mostly FRI, RGs and its mass seems to be correlated with the radio power (de Ruiter et al. 2002). Similar results are reported by de Koff et al. (2000) with respect to a sample of nearby 3CR radio galaxies: in at least 30% of the sources there is evidence for dust absorption. Dust in FRI galaxies is generally situated in well-defined disks on small scales ( $<2.5$  kpc), and the radio source axis is nearly perpendicular to the dust disk (de Ruiter et al. 2002, Verdoes Kleijn & de Zeeuw 1999). In addition, the derived dust masses of FRI galaxies are typically larger than the dust masses found in matched samples of radi-quiet ellipticals (de Koff et al. 2000). Numerous samples of nearby low luminosity radio galaxies (mostly FRI) were observed in CO (Prandoni et al. 2007, 2010, Lim et al. 2003, Leon et al. 2003, Ocaña Flaquer et al. 2010) all producing high detection rates. Very often a double-horn line profile consistent with a rotating disk is reported. Okuda et al. (2005) performed interferometric observations in CO of the source 3C 31 and showed that the CO emission and the dust disk (observed with the HST) are spatially coincident. They suggested that the cold gas is in stable orbits and the actual accretion rate is consequently very low. The association of CO and dust suggests that accretion of cold gas may power the radio jets and that in general a cold component could accrete onto the central BH in low luminosity RGs as well. Indeed Prandoni et al. (2010) showed that the derived masses of molecular gas appear to be adequate to power the jets, in at least some cases (e.g. 3C 31). If this cold gas component is an extra component or the

cooled-down counterpart of an initially hot gas phase is still an open question.

The same molecular gas fueling AGN could also give rise to decoupled stellar components (depending on its mass, origin and ability to turn into stars). The kinematic misalignment of the central gas and stars is a key ingredient for nuclear activity (Dumas et al. 2007). An optical integral-field spectroscopic analysis of molecular gas-rich RGs (with still active jets) would therefore provide a crucial comparison with the well studied radio-quiet ETGs (see Chapter 1), unveiling the role of the AGN in the overall formation and evolution scenario of ETGs, and providing important clues on the formation paradigm of RGs themselves, and on triggering mechanisms of their radio jets.

Systematic Integral-field spectroscopy is however missing for radio galaxy samples, and a comprehensive study of the stellar and gas properties of radio-loud early type galaxies has yet to be done. We have therefore built a complete volume-limited ( $z < 0.03$ ) sample of 11 *low power* RGs in the Southern sky, associated with ETGs, and observed it with the Visual Multi-Object Spectrograph (VIMOS) mounted on VLT UT3 in IFU (Integral Field Unit) observing mode. All the galaxies have also been observed in CO with APEX, and will be proposed for CO imaging with ALMA.

## 2.3 The Southern radio galaxy sample

Our Southern radio galaxies sample (hereafter referred to as the Southern Sample) was selected from the Parkes 2.7-GHz survey, which collects 191 RGs located in the declination range  $-17^\circ < \delta < -40^\circ$ ; down to a radio flux-density limit of 0.25 Jy at 2.7 GHz and down to an optical magnitude limit of  $m_V \leq 17.0$  (Ekers et al. 1989). The two selection criteria applied are:

- association of the source with an Elliptical or S0 galaxy
- host galaxy redshift  $z < 0.03$

The eleven selected sources have low or at most intermediate radio powers and show FRI radio morphology.

The main characteristics of the Southern Sample galaxies are listed in Table 2.1.

The sample is very similar to a complete sample of B2 (Colla et al. 1975) radio galaxies built in the Northern hemisphere, and consisting of 23 low luminosity radio galaxies, with  $z < 0.03$ . Sixteen of these were observed in CO with IRAM 30m telescope (Prandoni et al. 2007).

## 2.4 The role of molecular gas in low power radio galaxies

Prandoni et al. (2010) and Senatore et al. (2013) carried out CO line observation for 10 of the 11 RGs in the Southern Sample with the APEX single dish telescope. One source (NCG 1316) was already observed and detected in CO by Horellou et al. (2011). The emission in the CO(2-1) transition at 230 GHz rest frequency was investigated. The 27 arcsec APEX Half Power Beam Width probes the presence of molecular gas in the inner 2.7-16.2 kpc of the host galaxies (depending on redshift). This allows a direct comparison

Radio source	Host galaxy	$z$	$S_{1.4\text{GHz}}$ mJy	$\text{Log } P_{1.4\text{GHz}}$ (W Hz $^{-1}$ )	FR type	$m_K$ mag	$M_K$ mag	$\sigma$ km s $^{-1}$	dust	$T_{\text{dust}}$ Kelvin	$M_{\text{dust}}$ $M_{\odot}$
PKS 0007-325	IC 1531	0.025641	582	23.9	FRI	9.554	-25.70	222.6	—	—	—
PKS 0131-31	NGC 612	0.029771	4980	25.0	FRI/II	9.575	-26.01	—	dust lane <sup>a</sup>	38.8	7.2
PKS 0320-37	NGC 1316	0.005871	314	22.4	FRI	5.587	-26.44	225.9	dust patches <sup>b</sup>	38.4	6.0
PKS 0336-35	NGC 1399	0.004753	632	22.5	FRI	6.306	-25.25	341.9	no dust <sup>b</sup>	<24.4	<5.3
PKS 0718-34	—	0.028353	2050	24.6	FRI	9.969	-25.59	—	dust patches <sup>c</sup>	—	—
PKS 0958-314	NGC 3100	0.008813	541	23.0	FRI	8.077	-24.85	199.9	dust lane <sup>d</sup>	33.3	5.7
PKS 1107-372	NGC 3557	0.010300	777	23.3	FRI	7.203	-26.08	269.5	face-on disk <sup>b</sup>	35.9	5.6
PKS 1258-321	ESO 443-G 024	0.017042	1465	24.0	FRI	8.507	-25.87	274.7	no dust <sup>e</sup>	37.1	<5.1
PKS 1333-33	IC 4296	0.012465	64282	25.4	FRI	7.502	-26.18	333.2	edge-on disk <sup>b</sup>	49.7	4.8
PKS 2128-388	NGC 7075	0.018479	963	23.9	FRI	9.562	-24.98	259.9	—	22.7	7.4
PKS 2254-367	IC 1459	0.006011	1273	23.0	FRI	6.805	-25.27	306.1	dust lane <sup>b</sup>	40.9	5.1

Table 2.1: General properties of the Southern Sample radio galaxies: radio source name (*col 1*), host galaxy name (*col 2*), redshift (*col 3*), radio flux density at 1.4GHz and corresponding radio power (*cols 4 and 5*), FR type (*col 6*), the apparent and absolute magnitudes in K band (*cols 7 and 8*), velocity dispersion (*col 9*), optical dust morphology (*col 10*), dust temperature and mass from IRSAS observations (*cols 11 and 12*). The optical dust information come from: (*a*) Bettoni et al. (2001); (*b*) Lauer et al. (2005); (*c*) Colbert et al. (2001); (*d*) Sandag & Brocato (1979), (*e*) Govoni et al. (2000).

with the dust structures on similar scales imaged with HST. All sources were detected at either 40 or 80 km s $^{-1}$  velocity resolution (see Figure 2.4.1 and Figure 2.5.2 *right panel*). For the majority of the sources the CO lines show double horn or flat profiles, consistent with ordered rotation. The Southern Sample RGs typically show large linewidths ( $\geq 500$  km s $^{-1}$ ), and the derived molecular masses span a range between  $10^7$ - $10^9 M_{\odot}$ , in line with the results obtained for other RGs samples (see Table 2.2).

A first comparison between radio galaxies and the ATLAS<sup>3D</sup> optically selected ETGs was performed on the basis of the available CO observations. To increase the available statistics for radio galaxies a master radio galaxy sample was built by merging the following Northern samples:

- 24 low luminosity RGs with  $z < 0.03$  from B2 sample (Prandoni et al. 2007, Evans et al. 2005, Ocaña et al. 2010)
- 23 nearby ( $z < 0.031$ ) 3C RGs (Lim et al. 2003),
- 18 nearby ( $z < 0.0233$ ) RGs from the Uppsala General Catalogue (UGC) (Leon et al. 2003),
- 52 RGs, with  $z \leq 0.1$  and 1.4 GHz radio power  $> 10^{22}$  W Hz $^{-1}$ , from the TANGO sample (Ocaña et al. 2010).

Due to the overlap between the selected samples the total effective number of sources is 67. The majority of sources of the master sample have low or intermediate radio powers, they are mostly classified as FRI sources and have all been observed in CO. The CO detection rates are  $58\% \pm 16\%$ ,  $17.4\% \pm 8.7\%$ ,  $44.4\% \pm 15.7\%$ ,  $57.7\% \pm 10.5\%$  respectively. Reported line widths are in the range 150-800 km s $^{-1}$  while molecular gas masses span the range  $10^7$ - $10^9 M_{\odot}$ .

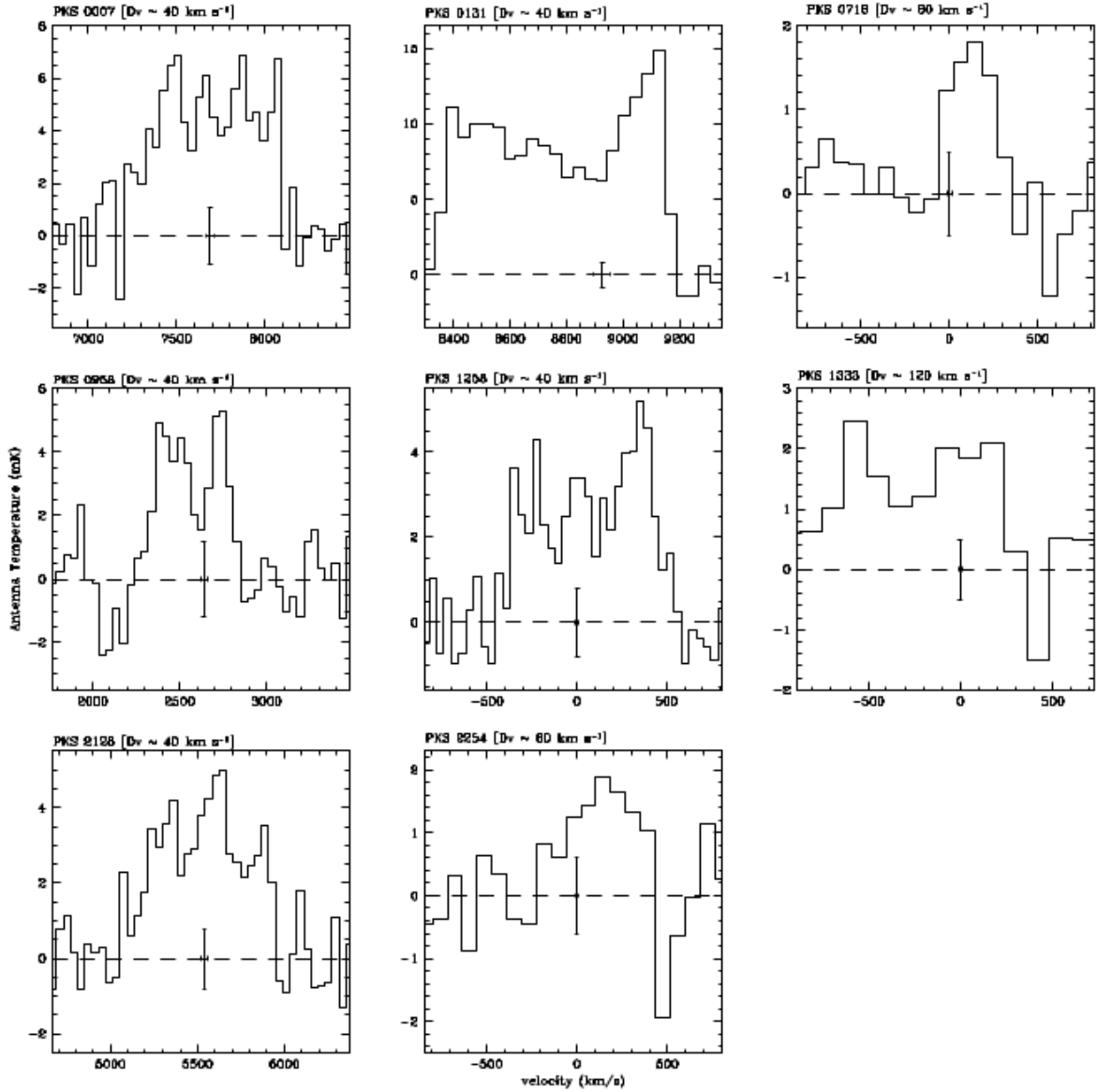


Figure 2.4.1: CO(2→1) APEX spectra for eight radio galaxies of the Southern Sample. *Top panel:* PKS 0007-325 and PKS 0131-31 are plotted with a velocity channel width of  $\approx 40 \text{ km s}^{-1}$ , while PKS 0718-34 is plotted with a velocity channel width of  $\approx 80 \text{ km s}^{-1}$ . *Middle panel:* PKS 0958-314 and PKS 1258-321 are plotted with a velocity channel width of  $\approx 40 \text{ km s}^{-1}$ , PKS 1333-33 with a velocity channel width of  $\approx 120 \text{ km s}^{-1}$ . *Bottom panel:* PKS 2128-388 is plotted with a velocity channel width of  $\approx 40 \text{ km s}^{-1}$ , PKS 2254-367 with a velocity channel width of  $\approx 80 \text{ km s}^{-1}$ . The horizontal dashed line indicate  $T_a=0$ ; the vertical and horizontal error bars at the systemic velocity ( $\sigma_{sys}$ ) indicate  $\pm T_a^{rms}$  and the error on  $\sigma_{sys}$  respectively.

Source	$t_{ON}$ min	$T_{sys}$ K	$\Delta v_{res}$ km s <sup>-1</sup>	$T_a^{rms}$ mK	$T_{peak}$ mK	$S/N$	$\Delta v_{FWHM}$ km s <sup>-1</sup>	$\Sigma T_a dv$ K km s <sup>-1</sup>	$M_{H_2}$ $10^7 M_\odot$	R kpc
PKS 0007-325	34	192	40	1.1	6.9	6.3	771	3.83	18.8±6.7	13.9
PKS 0131-31	64	190	40	0.8	15.0	18.8	774	7.19	284.9±32.9	16.2
PKS 0718-34	83	214	80	0.5	1.8	3.6	334	0.50	18.0±5.0	15.4
PKS 0958-314	62	191	40	1.2	5.3	4.4	446	1.68	6.1±1.1	4.9
PKS 1258-321	106	195	40	0.8	4.6	6.0	786	2.39	31.4±0.4	9.3
PKS 1333-33	55	207	120	0.5	2.5	5.0	864	1.50	10.0±0.2	6.9
PKS 2128-388	52	199	40	0.8	5.0	6.3	650	2.18	36.6±4.8	10.1
PKS 2254-367	79	227	80	0.6	1.9	3.2	492	0.70	0.8±0.3	3.4
PKS 0336-35 <sup>a</sup>	108	272	120	0.4	1.3	3.5	365	0.39	2.0±0.9	2.7
PKS 1107-372 <sup>a</sup>	18	316	40	2.0	7.0	3.5	248	1.52	31.6±6.7	5.6
PKS 0320-37 <sup>b</sup>	—	—	—	—	—	—	500	—	~35.0	3.9

NOTE (a) Sources studied by Prandoni et al. (2010), (b) Source studied by Horellou et al (2001).

Table 2.2: APEX-1 CO(2→1) line measurements of the Southern Sample.

The radio-quiet ETG sample selected as comparison sample consist of 52 ATLAS<sup>3D</sup> galaxies detected at 1.4 GHz from the NRAO VLA Sky Survey (NVSS). Condon, Cotton & Broderick (2002) classified such galaxies as “AGN powered” or “STAR-powered”, depending on whether the dominant source of the radio emission is an AGN or star formation.

The CO detection rate of the latter sample (48% ± 10%) is higher with respect to the total detection rate of the overall ATLAS<sup>3D</sup> sample (22% ± 3%) indicating that CO is more likely to be detected in galaxies with radio emission.

The Southern RG sample and the Northern RG master sample properties were then compared with those of the ATLAS<sup>3D</sup> subsample, in order to investigate the possible role of cold gas in fueling the AGN and to shed light on the formation history of *low power* RGs with respect to radio-quiet ETGs.

Both RGs and optically selected ATLAS<sup>3D</sup> ETGs show a strong correlation between molecular gas and warm dust masses as estimated from IRAS 60 $\mu$  and 100 $\mu$  fluxes (see Figure 2.4.2).

However, IRAS and CO line observations cover a different galaxy scale (the whole galaxy and the galaxy core respectively), so a more reliable comparison can be made between CO line observations and HST images. Indeed, four of the five galaxies in the Southern Sample showing dust disks or lanes are associated to double horn/flat CO line profiles, confirming the findings of Prandoni et al. (2010) for Northern radio galaxy samples.

It should be noted that also a galaxy not showing dust features seems to have a CO disk, suggesting that the molecular disks are a common feature in the cores of RGs.

In order to disentangle the role of cold gas from the role of stellar mass in producing powerful radio jets, the molecular gas mass was normalized with respect to the stellar mass ( $M_{star}$ ) as derived from the K-band. This normalization was done using the formula:

$$\log M(H_2)/M_{star} = \log M(H_2) + 0.4 \cdot M_K \quad (2.4.1)$$

where  $M_K$  is the absolute magnitude in the K-band.

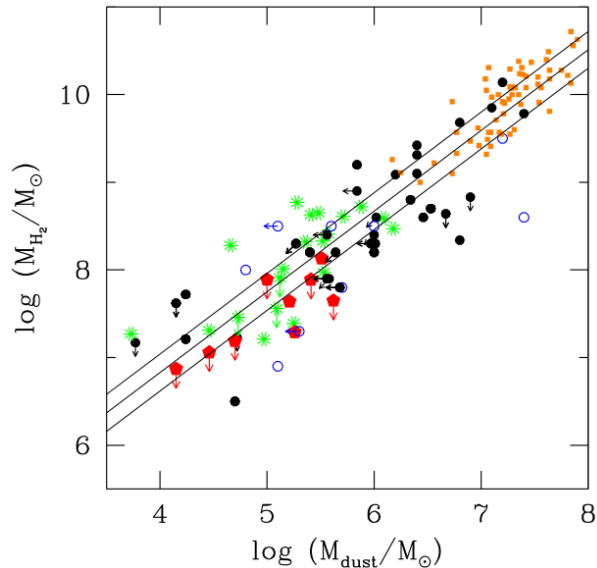


Figure 2.4.2:  $\log M(H_2)$  as a function of  $\log M_{dust}$ . Northern RGs are indicated with filled black circles while Southern RGs are shown as empty blue circles. The galaxies from the ATLAS<sup>3D</sup> sample are indicated with red pentagons (AGN-powered) and green asterisks (STAR-powered); IRAS selected infrared luminous galaxies are plotted as orange squares. Arrows indicate upper limits. A linear fit is also shown (black diagonal lines), together with its  $\pm 1\sigma$  tolerance.

Figure 2.4.3 shows that RGs have on average a higher content of molecular gas than the ATLAS<sup>3D</sup> AGN-powered sources. STAR-powered ATLAS<sup>3D</sup> galaxies, on the other hand, typically have the largest content of molecular gas, in line with the presence of young stars in molecular gas rich regions.

A similar analysis was repeated taking into account the BH mass. Figure 2.4.4 shows that, for any given BH mass, radio galaxies have a larger CO content than AGN-powered ATLAS<sup>3D</sup> galaxies.

This results suggest that cold gas may play a role in triggering the phenomenon of radio jets, through cold mode accretion, also in low luminosity radio galaxies.

Senatore et al. (2013) have also investigated possible correlations between AGN radio power and surface brightness profile. RGs always have a core profile (de Ruiter et al. 2005, Capetti et al. 2005, Capetti et al. 2006). Core profiles are commonly associated to at least a major merger and consequently to binary BH growth (Milosavljević et al. 2002). All RGs seem therefore to share a common evolution history.

The profile properties of radio galaxies and AGN-powered ATLAS<sup>3D</sup> galaxies are compared in Figure 2.4.5, as a function of radio power. It is clear that AGN-powered ATLAS<sup>3D</sup> galaxies have typically core profiles when their radio power exceeds  $\sim 10^{21} \text{ W Hz}^{-1}$ , while at lower powers power law profiles become dominant.

This suggests a common formation history scenario for both *low power* RGs and the most powerful ATLAS<sup>3D</sup> AGN-powered galaxies, indicating a possible relation between major mergers and AGN-driven radio emission also in cases where a classic large-scale “radio galaxy” morphology is missing. Core profile AGN-powered galaxies could be AGN whose activity has recently turned off.

The kinematic information of the ATLAS<sup>3D</sup> sample is finally considered. Senatore et

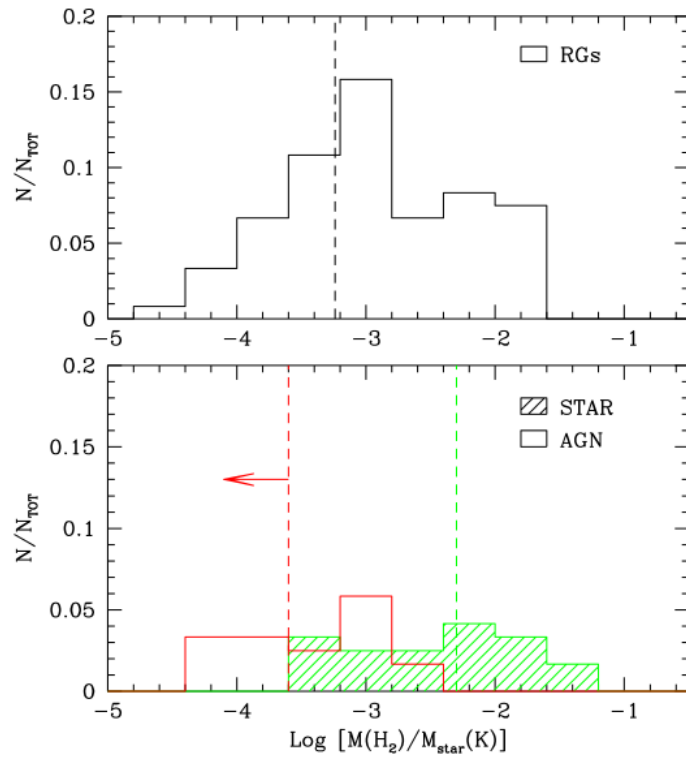


Figure 2.4.3: Histogram of the  $\text{Log} M(\text{H}_2) / M_{\text{star}}$  (from K band) ratio. *Top panel:* radio galaxies; the vertical dashed line indicates the median value. *Bottom panel:* ATLAS<sup>3D</sup> galaxies: AGN-powered galaxies (red histogram); STAR-powered galaxies (green histogram). The red and green vertical dashed lines represent the median values of AGN-powered and STAR-powered galaxies respectively.

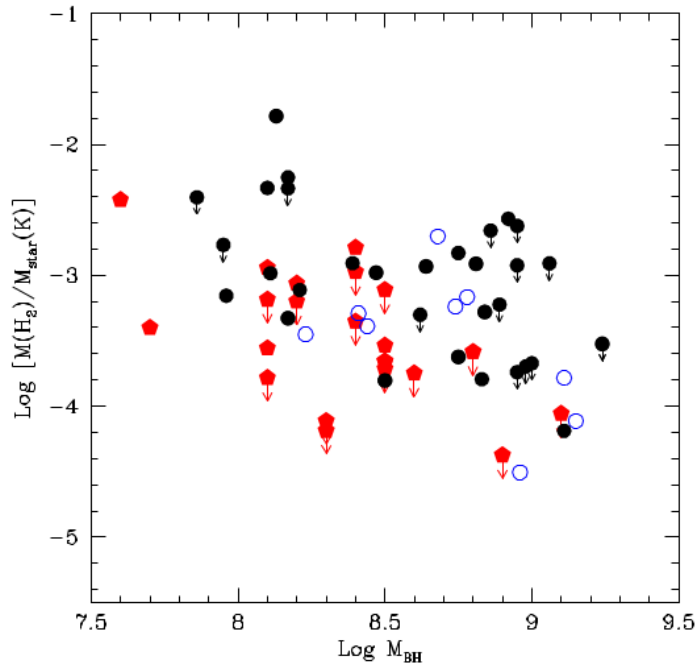


Figure 2.4.4:  $\text{Log } M_{\text{H}_2} / M_{\text{star}}(\text{K})$  ratio versus  $\text{Log } M_{\text{BH}}$ . Northern RGs are indicated by filled black circles, southern RGs by (blue) empty circles. Galaxies of the ATLAS<sup>3D</sup> sample classified as AGN-powered are represented by (red) pentagons.

al. (2013) notice that four radio galaxies in the Northern master sample are part of the ATLAS<sup>3D</sup> sample. Two are *Fast Rotators* and two are *Slow Rotators*. Despite the limited statistics, this seems to indicate that the radio galaxy phenomenon can be produced in both cases.

Figure 2.4.6 shows the distribution in radio power for both *Fast* and *Slow* AGN-powered ATLAS<sup>3D</sup> rotators. Also included are three radio galaxies for which both profile and kinematic information is available.

Again a correlation is found, with *Slow Rotators* having average higher radio powers than *Fast Rotators*.

A common formation history scenario (major mergers) for both radio galaxies and the most powerful (*Slow Rotators*) ATLAS<sup>3D</sup> AGN-powered galaxies seems to be plausible. However, a more detailed analysis taking into account both kinematic and profile properties, as well as molecular gas properties (plausibly connected to wet/dry merger scenarios), could not be performed due the very poor statistics available for RGs.

This calls for integral field spectroscopy for larger samples of radio galaxies, and motivates our VIMOS/IFU observations of the Southern RG sample.

## 2.5 The case of NGC 3557

NGC 3557 ( $z = 0.0103$ ) is one of the eleven RGs in our Southern Sample for which VIMOS/IFU observations were acquired. NCG 3557 is an isolated radio galaxy which does not show signs of recent mergers, interactions, and ongoing star formation ( $< 1$

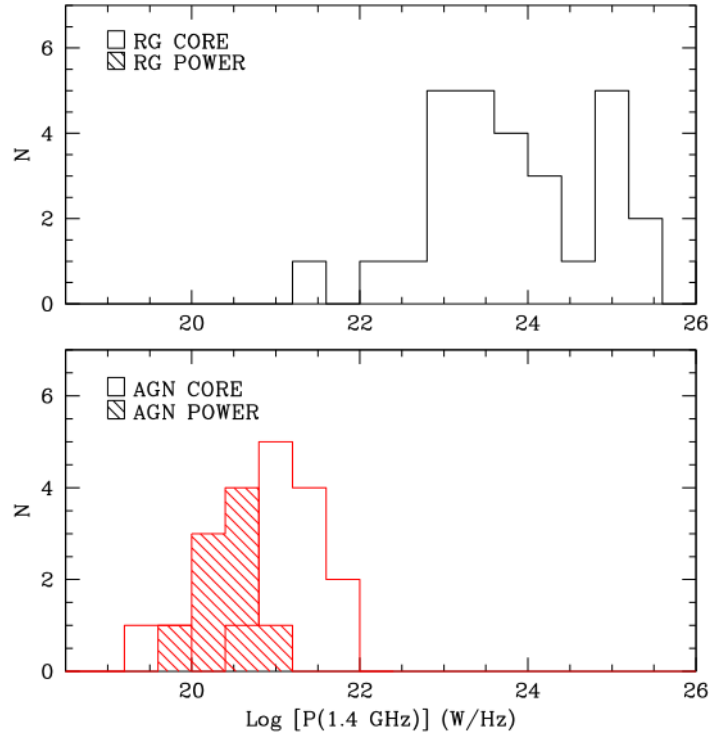


Figure 2.4.5: Distribution in radio power for core and power law galaxies. *Top panel*: radio galaxies (all with core profiles). *Lower panel*: ATLAS<sup>3D</sup> AGN powered galaxies. Galaxies with core or intermediate profiles are shown by the empty histogram while those with power-law profiles are indicated by the shaded histogram.

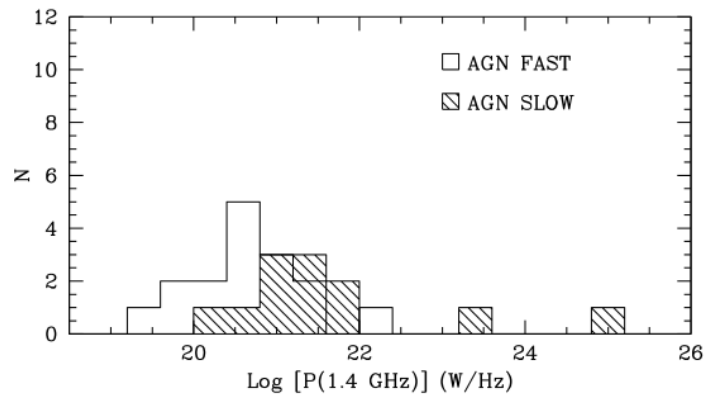


Figure 2.4.6: Histogram of the logarithm of radio power according to kinematical properties for ATLAS<sup>3D</sup> AGN-powered and radio galaxies. Empty histogram represents *Fast Rotators*, shaded histogram *Slow Rotators*.

<b>Radio Source</b>	PKS 1107-372
<b>Host Galaxy</b>	NGC 3557
<b>RA (J2000)</b>	11:09:57.65
<b>DEC (J200)</b>	-37:32:21.0
<b>z</b>	0.010300
$D_A$ [Mpc]	43.6
$D_L$ [Mpc]	44.5
$S_{1.4GHz}$ [mJy]	777
<b>Log <math>P_{1.4GHz}</math></b>	23.3
<b>Radio Morphology</b>	FRI
<b>T-Type</b> <sup>1</sup>	-4.8±0.4
$m_B$ [mag]	11.50
$m_V$ [mag]	10.40
$m_R$ [mag]	9.79
$m_K$ [mag]	7.203
<b>AB [mag]</b> <sup>2</sup>	0.426
$M_K$ [mag]	-26.08

NOTE 1) Extracted from HyperLeda catalogue; 2) AB is the galactic extinction (Schlegel et al. 1998)

Table 2.3: Radio/Optical properties of NGC 3557.

$M_{\odot} \text{ yr}^{-1}$  from Spitzer spectral observations). It is therefore an excellent case to assess the possible mechanisms triggering the radio emission in *low power* radio galaxies, as a merger scenario does not obviously apply.

The main radio/optical properties of NGC 3557 are summarized in Table 2.3.

In Figure 2.5.2 (*left panel*) the VLA radio continuum image of NGC 3557 is shown. NGC 3557 hosts a twin-jet and can be classified as a FRI radio source.

Govoni et al. (2000) performed a detailed analysis of the morphological and photometric properties of a sample of nearby radio galaxies including NGC 3557. The NGC 3557 luminosity profile (see Figure 2.5.1) is fairly well fitted by a simple de Vaucouleurs law:

$$I(r) = I_0 \cdot \exp \left\{ -7.67 \left[ \left( \frac{r}{R_e} \right)^{\frac{1}{4}} - 1 \right] \right\} \quad (2.5.1)$$

where  $I_0$  is the surface brightness at  $r = 0$  and  $R_e$  is the effective radius.

NGC 3557 shows an evident flattening with respect to the  $r^{1/4}$  law in the inner part ( $r < 2$  kpc) that could be ascribed to a substantial deviation from isothermal distribution of stars or to a significant diffuse dust absorption. For NGC 3557 extra components (in the inner and/or the outer regions of the profile) are not needed to obtain a good surface brightness fit.

In Table 2.4 summarizes the effective radius  $R_e$  and the magnitude  $mag_{R_e}$  estimated within it, and derived from Equation 2.5.1. The central velocity dispersion  $\sigma_v$ <sup>1</sup> and the mass of the BH are also reported. The BH mass was derived from the equation:

<sup>1</sup>Extracted from HyperLeda Catalogue

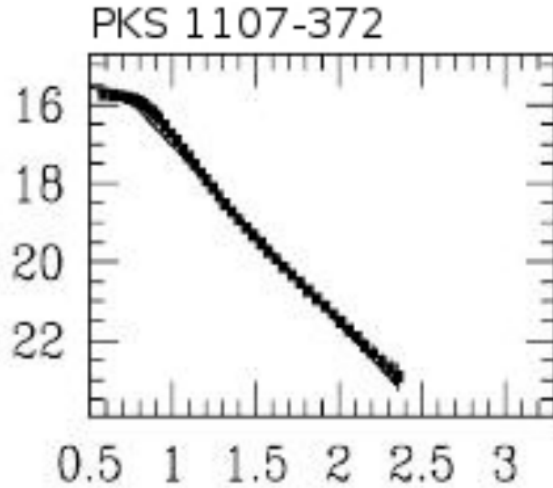


Figure 2.5.1: Luminosity profile of NGC 3557. The  $x$  axis reports  $r^{1/4}$  (kpc), while the  $y$  axis reports  $\mu_R = \ln I(r)$  (mag/arcsec<sup>2</sup>).

<b>Radio Source</b>	PKS 1107-372
<b>Host Galaxy</b>	NGC 3557
<b>Profile <math>R_e</math> [arcsec]</b>	40.4
<b>Profile <math>mag_{R_e}</math></b>	10.16
<b><math>\sigma_v</math> [km s<sup>-1</sup>]</b>	$267.7 \pm 8.3$
<b><math>\log(M_{BH}/M_{\odot})</math></b>	8.74

Table 2.4: Photometric and structural parameters of NGC 3557.

$$\log(M_{BH}/M_{\odot}) = (8.23 \pm 0.08) + (3.96 \pm 0.42) \cdot \log(\sigma_v/200). \quad (2.5.2)$$

Lauer et al. (2005) imaged the core of a sample of ETGs, including NGC 3557, with the HST. The inner surface brightness profile was fitted using a “Nuker law” that, as discussed in Chapter 1, allows to classify the galaxy profiles in core or power law. Unfortunately, due to dust obscuration of the galaxy centre, the surface photometry profile could not be derived. As shown in Figure 2.5.2 (*central panel*), the dust is located in a well defined nuclear disk in the very centre of the HST image.

NGC 3557 was observed with in the CO(2-1) line, as part of the science verification programme of the APEX-1 receiver by Prandoni et al. 2010. The CO line parameters are shown in Table 2.2.

NGC 3557 was detected at a channel resolution of  $\Delta v_{res} \approx 40$  km s<sup>-1</sup>, and, as shown in Figure 2.5.2 (*right panel*), it display a double-horned CO line profile. If confirmed, the presence of CO in ordered rotation would be consistent with the strong dusty disk seen in the HST image.

Annibali et al. (2007; 2010) studied the stellar population and ionized gas properties of a sample of 65 nearby ETGs including NGC 3557. The analyzed long-slit spectra cover the 3700-7250 Å wavelength range with a spectral resolution of  $\approx 7.6$  Å at 5550 Å.

In Annibali et al. (2007) ages, metallicities, and  $[\alpha/\text{Fe}]$  ratios were derived using

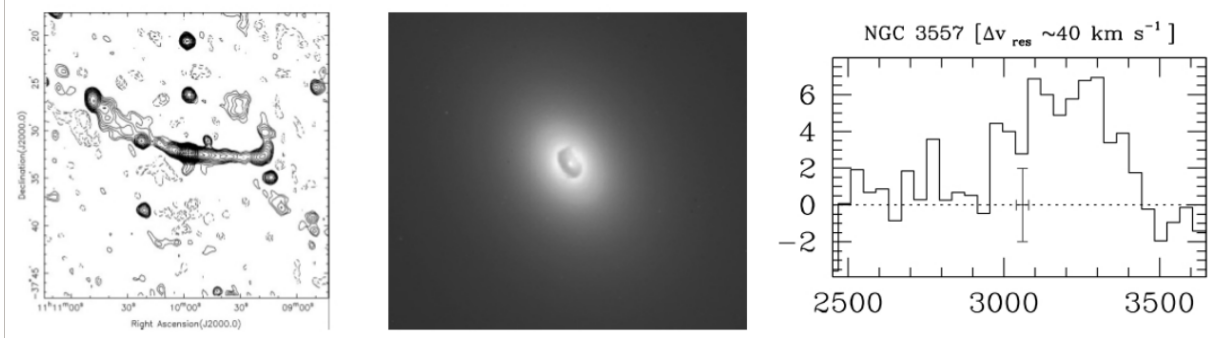


Figure 2.5.2: Observations of NGC 3557. *Left*: 1.4 GHz VLA radio continuum image ( $30' \times 30'$ ), showing the large-scale radio source from NVSS. *Middle*: NGC 3557 optical HST image ( $15'' \times 15''$ ) showing the central dust disk. North is at the top on both images: the disk normal is not aligned with the radio jets. *Right*: APEX CO(2–1) integrated line profile, consistent with a double-horned profile as expected for a disk. Antenna temperature (mK) vs. velocity ( $\text{km s}^{-1}$ ).

Object	$\sigma_c$ [ $\text{km s}^{-1}$ ]	Age Gyr	Z	$[\alpha/\text{Fe}]$
NGC 3557	265	$5.8 \pm 0.8$	$0.034 \pm 0.004$	$0.17 \pm 0.02$

Table 2.5: Object name, velocity dispersion  $\sigma_c$  (from HyperLeda), and average age, metallicity, and  $\alpha/\text{Fe}$  ratios for a  $R_e/8$  aperture.  $Z=0.018$  is the solar value. The latter values are obtained combining the information from  $\text{H}\beta$ ,  $\text{H}\gamma$ ,  $\text{H}\delta$ ,  $\text{Mgb}$  and  $\langle Fe \rangle$  indices.

new simple stellar population (SSP) models accounting for the  $\alpha/\text{Fe}$ -enhancement. The stellar population parameters are derived using an algorithm that provides the most likely solution in (age, Z,  $[\alpha/\text{Fe}]$ ) space together with the probability density function along the age-metallicity degeneracy. The reported results for NGC 3557 are summarized in Table 2.5.

In Annibali et al. (2010) the ionized gas emission lines were extracted from the galaxy spectra after an accurate subtraction of the underlying stellar continuum (accounting for the effects of the age-metallicity degeneracy). Galaxies were first classified according to the intensity of their nuclear emission lines: no emission galaxies (N), when no emission lines were detected; weak emission-line galaxies (W), when equivalent widths  $\text{EW}(\text{H}\alpha + [\text{NII}]\lambda 6584) < 3 \text{ \AA}$  were measured; and strong emission-line galaxies (H) when  $\text{EW}(\text{H}\alpha + [\text{NII}]\lambda 6584) > 3 \text{ \AA}$  were found.

A second classification was made by using the standard  $[\text{OIII}]\lambda 5007/\text{H}\beta$  versus  $[\text{NII}]\lambda 6584/\text{H}\alpha$  BPT diagnostic diagram (Baldwin, Phillips and Terlevich 1981) and its following revisions (Kewley et al. 2001, Kauffmann et al. 2003, Kewley et al. 2006). In such a diagram galaxies which are likely to be dominated by an AGN can be separated from galaxies dominated by star formation. In addition Seyfert galaxies can be distinguished from Low Ionization Nuclear Emission Regions (LINER) galaxies.

The classification obtained by Annibali et al. (2010) in the nuclear ( $r \leq R_e/16$ ) region for NGC 3557 defines the galaxy as a weak emission-line (W) LINER galaxy.

A kinematic classification of the galaxy was also obtained: the  $(V/\sigma)_e$  parameter was extrapolated from the  $(V/\sigma)_{scaled}$  parameter, obtained from long-slit measurement by

assuming  $(V/\sigma)_{scaled}=0.57 \times (V/\sigma)_{slit}$  (Cappellari et al. 2007), where the ellipticity  $\varepsilon$  was taken from the literature. From the obtained values ( $(V/\sigma)_{scaled}=0.3$  and  $\varepsilon=0.21$ ) the galaxy was classified as a *Fast Rotator* with respect to the  $(V/\sigma)_e$  vs  $\varepsilon$  diagram presented in Cappellari et al. (2007).

From the statistical analysis of the whole sample, Annibali et al. (2010) could not exclude a LINER scenario in which more than a source for the ionizing photons is present at different galaxy radii. In the galaxy centre post-AGB stars fail to account alone for the ionizing photon budget, while in more extended regions, they may do well the job, in agreement with the findings of Sarzi et al. (2009). They thus investigated photoionization by sub-Eddington accretion rate AGNs and fast shocks, finding good results in terms of reproducing the central emission line ratios of their LINER sample.



# Chapter 3

## The VLT, VIMOS and the IFU observing mode

### 3.1 VLT and the Unit Telescopes

The ESO Very Large Telescope (VLT) is an array composed of four Unit Telescopes and four Auxiliary Telescopes. It is located on the top of the Cerro Paranal mountain, in the midst of Atacama desert of northern Chile. The main mirror diameters are 8.2m and 1.8m for the Unit and the Auxiliary telescopes respectively. They can work together as a giant interferometer (the so-called VLT Interferometer VLTI) reaching milliarcsec resolution, but the Unit telescopes are mainly employed for individual observations. Two additional telescopes are also available for imaging surveys: the Visible and Infrared Survey Telescope for Astronomy (VISTA, 4m) and the VLT Survey Telescope (VST, 2.6m). The four Unit telescopes (UT1, UT2, UT3 and UT4) are very similar in terms of structure, features and capabilities, while they host different receivers and backends. In the following a single Unit telescope will be described as reference. Figure 3.1.1 show the telescopes at Paranal with their suite of current and future receivers/instrumentation.

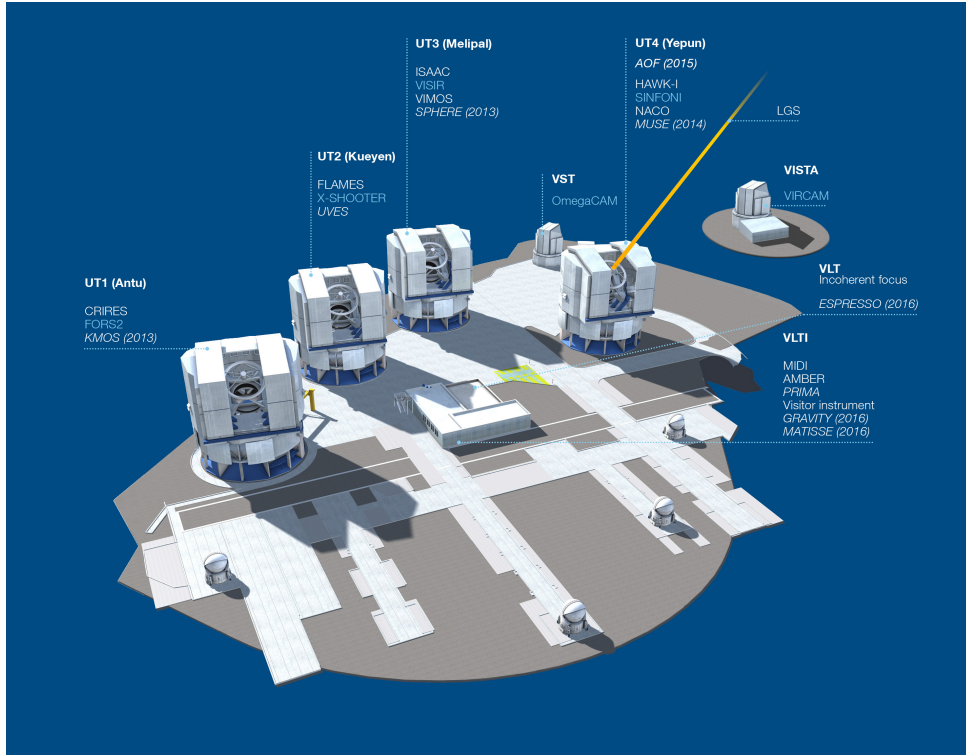


Figure 3.1.1: The current and future (indicated in italics) instrumentation available at the telescopes at Paranal site.

The Unit telescope has an alt-azimuth mount and it can observe the entire southern sky moving along two axes: the vertical axis, called azimuth axis, and the horizontal one, called elevation axis. The main telescope components are outlined in Fig 3.1.2 and Fig 3.1.3. The supporting structure of the telescope is composed of two main components: the M1 Cell and the M3 Tower. The M1 Cell is a metallic structure supporting the main telescope tube: on the upper side is located the primary mirror, while the lower side supports the Cassegrain adapter/rotator. The M3 tower is mounted at the centre of M1 Cell and supports the elliptical tertiary mirror. A mechanism allows to change its position moving it out from the light optical path when the telescope observes in Cassegrain mode. The secondary mirror (M2) is located on the upper side of the telescope tube.

The so-called M2 Unit is an optomechanical system including the M2 mirror, the mechanisms to support the mirror and control its position and the related electronics. The secondary mirror can be moved along five degrees of freedom in order to optimize its performances in terms of focusing (affected by gravity induced deflections) and pointing.

The VLT Enclosure is the cylindrical structure containing the entire Unit Telescope; it protects the telescope against hostile weather conditions, it allows the access and the maintenance of its different components, provides for active/passive thermal control and air flow control within the Enclosure itself.

The optical scheme is of Ritchey-Chretien type: the light collected by the primary hyperbolic mirror (M1) is focused on the secondary hyperbolic mirror (M2) and from here into one of the four foci. The Cassegrain focus is located in the central hole of the primary mirror and directly illuminated by the M2 light. The two Nasmyth foci are reached by means of a central elliptical tertiary mirror (M3). The Coudé focus is reached

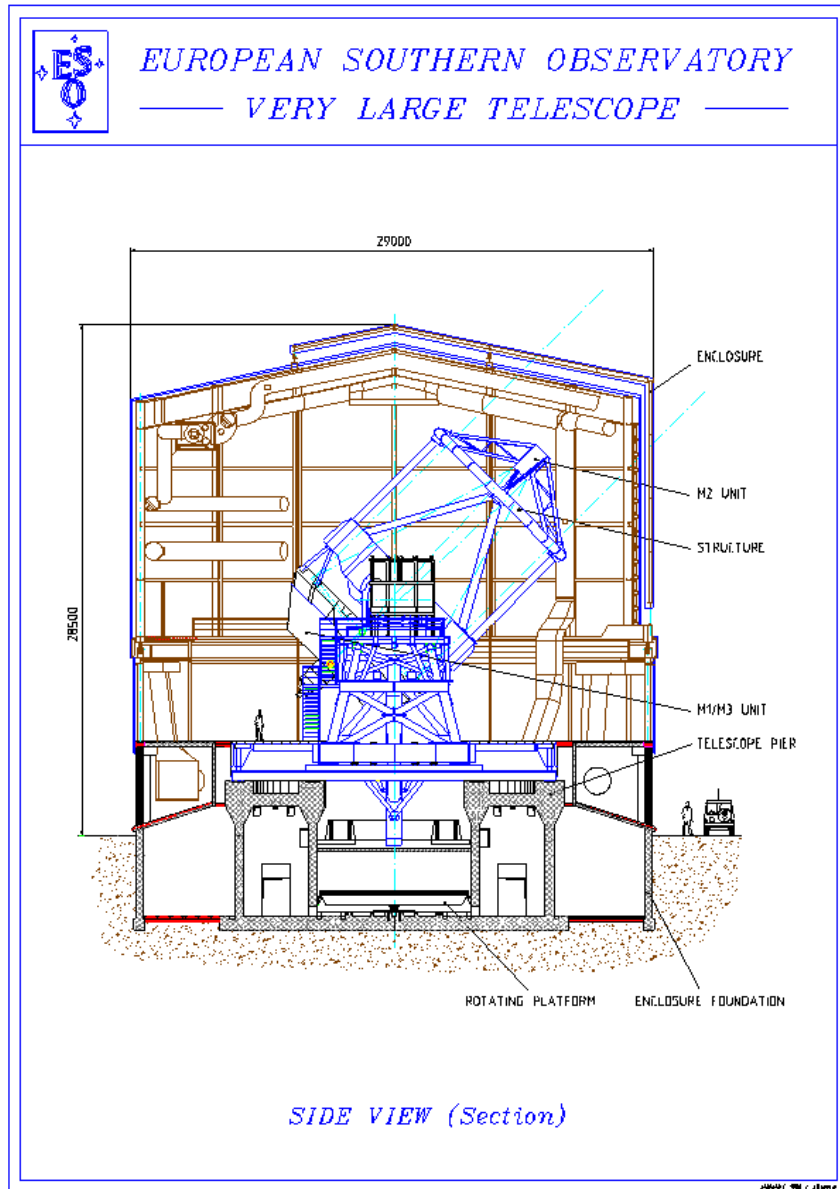


Figure 3.1.2: A schematic side view of one unit telescope of the VLT.

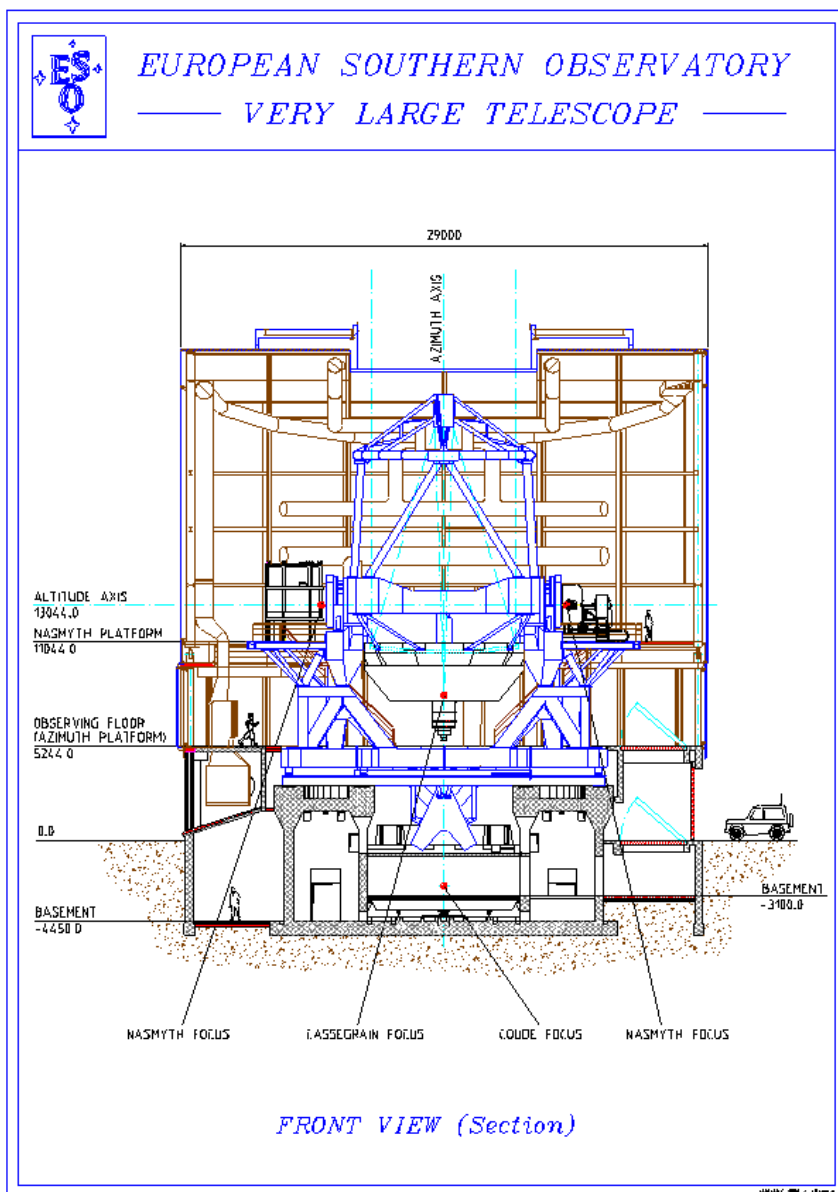


Figure 3.1.3: A schematic front view of one unit telescope of the VLT.

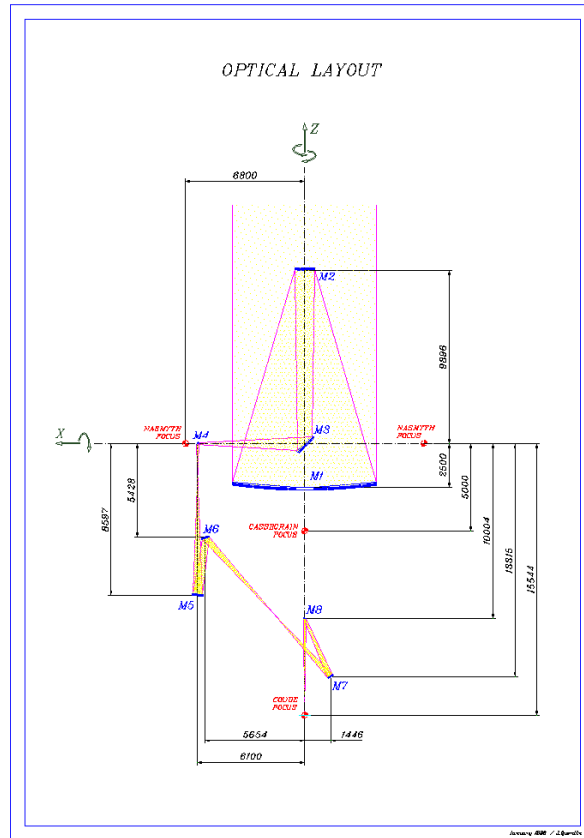


Figure 3.1.4: Unit optical layout scheme.

thanks to a lens system that transfer the light beam from one of the Nasmyth foci down to the telescope basement. The optical layout scheme is shown in Fig 3.1.4.

The primary mirror temperature can be actively controlled using the black plate cooling system; this is useful in presence of temperature drops during an observation. The cooling system cools down the bottom side of M1 via radiative exchange reducing the temperature difference with respect to the environment and providing a better mirror seeing.

The Unit Telescope is equipped with an Active Optics System able to modify both the M1 shape and the M2 position. This system can compensate for static or slowly varying deformations mainly due to wind pressure, inclination of the telescope or manufacturing errors. The Active Optics System is composed by four main elements: the primary mirror and its active support system (a system of 150 actuators), the M2 Unit, the CCD Shack-Hartmann wavefront sensor (WFS), and the wavefront analysing system. A schematic view is shown in Fig 3.1.5. The image of a reference star in the field of view is periodically analyzed by the CCD wavefront sensor; monitoring its position and shape with respect to a given better quality image of the same star, a computer evaluates the various optical deformations that affect the image and defines the mechanical corrections to be applied. In absence of a guide star the applied corrections are based on theoretical predictions.

The interface between the telescope and the scientific instrumentation is an annular Adapter-Rotator placed at each focus. The Adapter CCD sensor allows the object visual identification (Field Acquisition) and the pointing of a guiding star during the

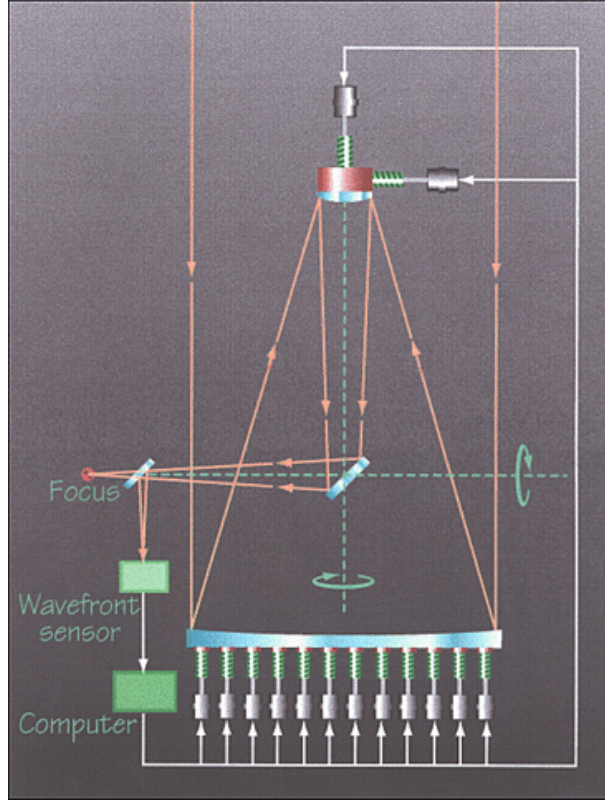


Figure 3.1.5: The Active Optics System main components.

Telescope	Focus			
	Nasmyth A	Cassegrain	Nasmyth B	Interferometric
<b>UT1</b> (Antu)	CRIRES	FORS2	KMOS	VLTI Visitor Instrument AMBER; MIDI;
<b>UT2</b> (Kueyen)	FLAMES	Visitor Instrument	UVES	
<b>UT3</b> (Melipal)	ISAAC	XSHOOTER	VIMOS	
<b>UT4</b> (Yepun)	HAWK-I	SINFONI	NACO	

Table 3.1: Instruments currently available at Unit Telescopes.

observation (Guiding). A wavefront sensor is able to monitor and correct the primary mirror deformations due both to gravity and to slow effects like thermal gradients (Wave front Sensing). The field rotation during the observation is compensated by rotating the scientific instrumentation in the same way as the field (Instrument Rotation).

All the instruments available at the Units telescopes are listed in Table 3.1. In the following sections we will focus on the VIMOS spectrograph, and in particular on its Integral Field Unit (IFU) operation mode, as this is the observational mode relevant for this thesis.

For further details about the VLT see the ESO web page:

<https://www.eso.org/sci/facilities/paranal/telescopes/ut/index.html>

Instrument Location	Nasmyth B VLT-UT3 (Melipal)
Opto-mechanical layout	4 beams, each a complete focal-reducer, F/1.88 output
Wavelength coverage	0.37 to 1 microns
Detectors	$4 \times 2048 \times 4096$ , 15 $\mu\text{m}/\text{pixel}$ Deep-depletion E2V 44-82 (new)
Spectral Resolution	$R = 180$ to $2500$ (1 arcsec slit)
Filters	10 per channel, $U'BVRIZ$ , OS-red, OS-blue, GG435, GG475, 170mm diameter
Grisms	6 per channel, LR red, LR blue, MR, HR blue, HR orange, HR red
Flexures	Active compensation: positioning accuracy $< 0.3$ pix during acquisition
Masks	10 masks simultaneously loaded in instrument (practical) maximum (per channel)
	Slits of any position and shape, width $> 0.6''$ , length $< 30''$ .
Multiplex	840 simultaneous slits, $10''$ long at $R = 200$ 210 simultaneous slits, $10''$ long at $R = 2000-2500$
Integral Field Unit	$54'' \times 54''$ field, 6400 fibers with $0.67''$ sampling $27'' \times 27''$ field, 6400 fibers with $0.33''$ sampling

Table 3.2: VIMOS opto-mechanical characteristics.

## 3.2 The Visual Multi-Object Spectrograph (VIMOS)

The Visual imager and Multi-Object Spectrograph (VIMOS) is mounted at the VLT-UT3 Nasmyth B focus. Because of the large field of view, VIMOS optical path is split into four channels. The four quadrants of the instrument are operated in parallel. The total field of view of the four channels is  $4 \times 7' \times 8'$  in IMG and MOS and up to  $54'' \times 54''$  in IFU mode. Each channel is connected to a  $2048 \times 4096$  pixels, deep depletion, backside illuminated, double layer coating, CCD. The VIMOS covers the spectral range range from 0.37 to  $1.0 \mu\text{m}$  and it can operate in three different modes: direct Imaging (IMG), multi-slit spectroscopy (MOS) and integral field spectroscopy (IFU). The mean VIMOS opto-mechanical characteristics are indicated in Table 3.2 while the VIMOS Opto-Mechanical layout is shown in Figure 3.2.1 and Figure 3.3.1.

At the focal plane each of the four channels is equipped with mask units in order to rearrange the incoming light in a useful way to produce the required spectra when observing in MOS or IFU mode. The folding mirrors channel the light to the Filters/Camera Section. The Filters/Camera Section hosts the filter exchange units (FEU) with 10 different filters, the grism exchange unit (GEU) with six grism permanently mounted, the camera and the exposure shutter in front of the CCD. In Direct imaging mode (IMG) wide field images can be obtained with 10 different broadband filters. The IMG mode is also used for the preparation of the masks to be used for multislit spectroscopy.

The Multi-Object Spectroscopy mode (MOS) can be used with different grism + filter combinations. Slits can be positioned all over the  $4 \times 7' \times 8'$  field of view, but constraints apply, to avoid overlaps in both positional and spectral dispersion directions on the CCD. With the low resolution grisms up to four slits can be positioned along the dispersion direction while with the intermediate resolution grisms the maximum number of available slits is two (spectra must be short enough to allow stacking). With the high-resolution grisms, only one slit can be placed along the dispersion direction.

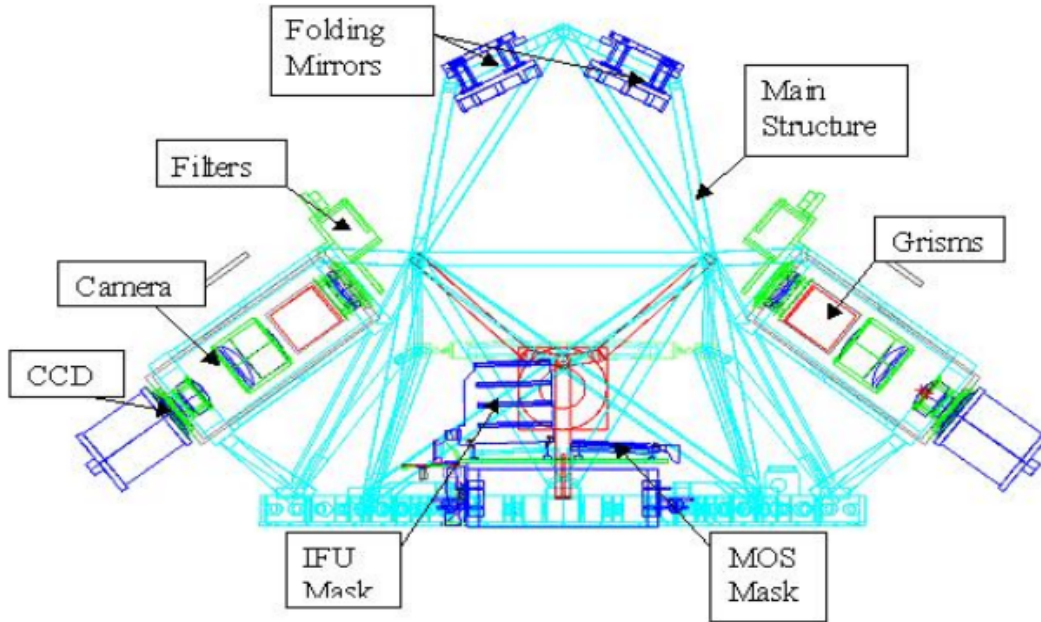


Figure 3.2.1: VIMOS opto-mechanical layout scheme. The main components are shown.

Parameter	Value
Number of pixels	2048×4096
Pixel size ( $\mu\text{m}$ )	15
Dark current at $-120^\circ\text{C}$ ( $e^-/\text{px}/\text{h}$ )	<7
Deviation from Linearity (Full well; %)	< 0.5
Charge transfer efficiency	>0.999995

Table 3.3: Basic characteristics of the new VIMOS CCDs.

The Integral Field Spectroscopy mode (IFU), the most relevant for this thesis, is described in detail in the following section.

### 3.2.1 Detectors

The four current 2048x4096 pixels CCDs were installed in August 2010. This new set of CCDs have better sensitivity performances in the red part of the spectrum and reduce also the fringing instrumental effect<sup>1</sup>. The new Quantum Efficiency curve (solid line) is compared with the old one (dotted line) in Fig 3.2.2. The main CCD characteristics are listed in Table 3.3.

There are two read-out ports, although only one is used. This increases the read-out time but keep the gain and the read-out noise (spurious events during the read out of

<sup>1</sup>Fringes arise from the interference, in the CCD detection layer, between incident light and the light reflected from the interfaces of the CCD layers.

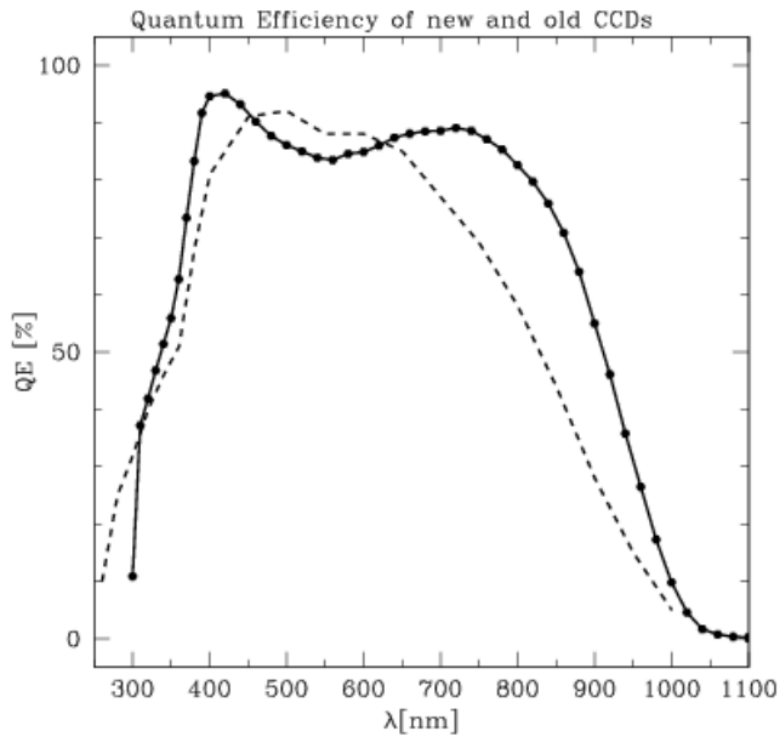


Figure 3.2.2: Quantum efficiency curves of the new (thick line) and old (dashed line) VIMOS CCDs.

the information on the CCD) constant. The readout mode currently in use is a high gain mode with binning factor  $1 \times 1$  and velocity  $225 \text{ kpxs}^{-1}$ . For more details on CCDs performances see the ESO web page:

<http://www.eso.org/sci/facilities/develop/detectors/optdet/docs/reports/EEV-report.html>

The CCD controller (named FIERA) is a new generation controller developed by ESO; it allows to run a large number of CCD outputs at fast readout rates and uses low noise, high speed amplifiers. For more informations the ESO reference page is:

<http://www.eso.org/sci/facilities/develop/detectors/controllers/fiera.html>

IFU mode positional acquisition accuracy is  $\sim 3$  arcsec i.e. the accuracy of the telescope pointing.

The Active Flexure Compensation System (AFC) controls image shifts due to instrument flexures under gravity. The FoV image is positioned on the detector with an accuracy better than 0.3 pixels and can be maintained there to within  $\sim 1.5$  pixels for the duration of a typical exposure. A problem that remains still unsolved is a fringing effect due to internal reflections in the IFU unit. It is negligible at 400 nm, but increases with wavelength. For details about these issues and other technical information we refer to the VIMOS User Manual.

A calibration screen is placed at the back of the Nasmyth shutter and illuminated by three calibration units. Each Unit is equipped with a halogen lamp for IFU screen flats and three Arc lamps (He, Ar, Ne) whose spectral lines for all gratings can be found at the following link:

<http://www.eso.org/sci/facilities/paranal/instruments/vimos/inst/atlas/index.html>

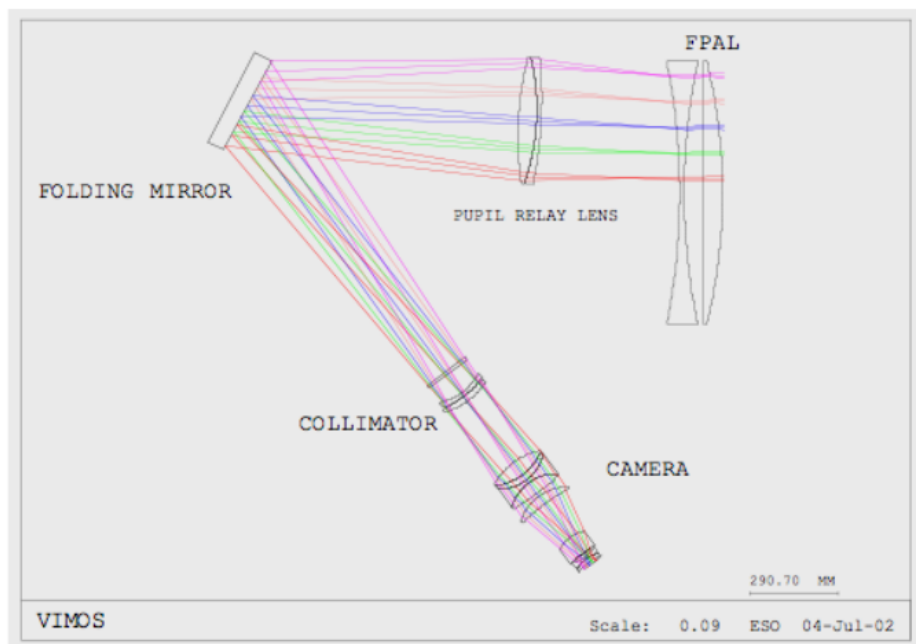


Figure 3.3.1: VIMOS optical layout for one of the four Quadrants. The Focal Plane Adaptation Lens (FPAL) corrects astigmatism and field curvature and together with the Pupil Relay Lens (PRL) provides for pupil chromatism correction. A folding mirror channels the light to the collimator and to an active flexure compensation system.

<http://www.eso.org/sci/facilities/paranal/instruments/vimos/news.html>

### 3.3 The Integral Field Unit mode

The Integral Field Unit (IFU) is able to produce spectra for contiguous sky regions up to a  $54 \times 54$  arcsec<sup>2</sup> field of view divided in four quadrants (see Figure 3.3.2). In IFU mode the full CCD area is read-out even if the illuminated CCD area is slightly smaller (about  $1970 \times 4096$  pixels<sup>2</sup>). A focal elongator provides two spatial samplings: 0.33"/fiber and 0.67"/fiber. Along its optical path, the light pass through the lens system shown in Fig 3.3.1 that corrects for optical aberrations and collimates the light toward the Filter/Camera Section.

At the focal plane an IFU fiber-head and an IFU mask are associated to each of the four channels in order to rearrange the incoming light in a useful way to produce an ordered grid of spectra on the CCD. In particular, as the light enters the instrument, the observed sky region is projected onto a micro-lens array where each micro-lens is coupled to an optical fiber. Each quadrant is associated to a single mask on the IFU head and receive one fourth of the 6400 total fibers.

Following the scheme illustrated in Fig 3.3.3, a single quadrant is further divided in four squared zones each associated to a bundle of 400 optical fibers.

To reproduce an entrance slit to the spectrograph, the so called pseudo-slit, the light from each fiber bundle is redistributed on a linear set of micro-lenses. In this way each

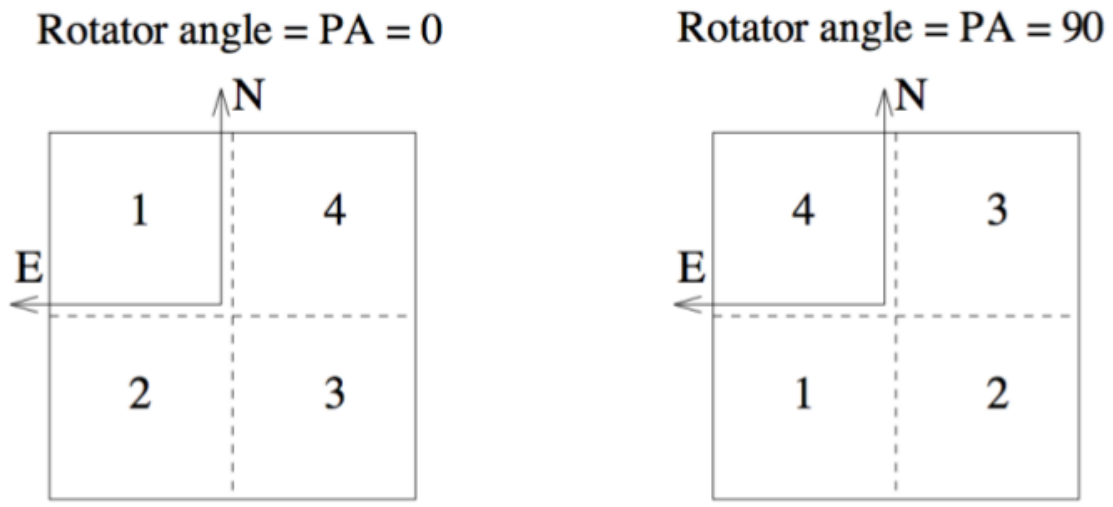


Figure 3.3.2: The four quadrants covering the entire VIMOS IFU FoV and their orientation on sky for PA = 0° and PA=90°.

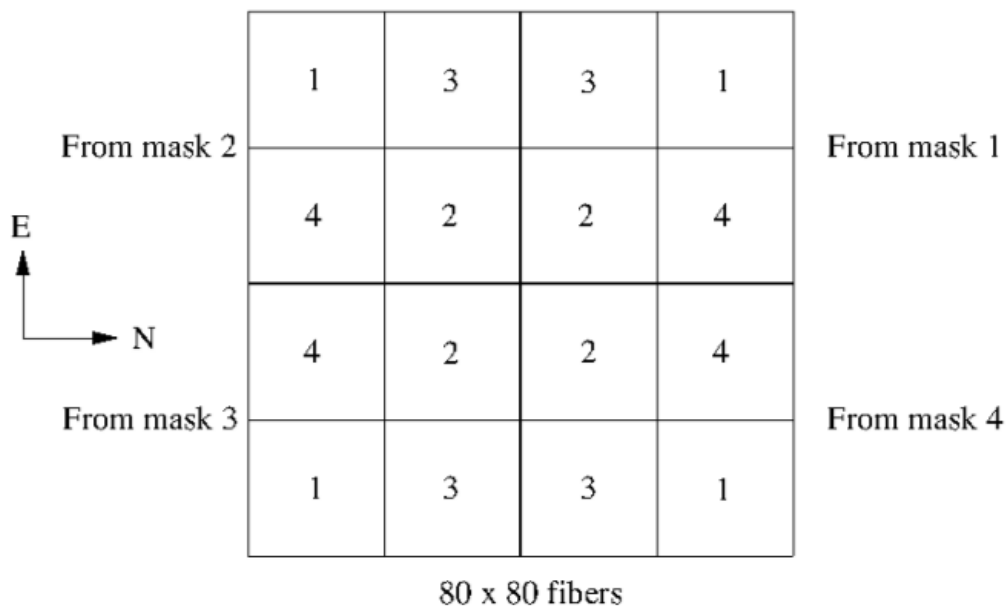


Figure 3.3.3: Arrangement of the four bundles of optical fibers. In each quadrant four spectra bundles are positioned as indicated by the numbers from 1 to 4. The same numbers can be used to indicate the pseudo-slit.

Grism	Shutter	Spatial sampling (arcsec/fibre)	Field of view arcsec <sup>2</sup>	Number of fibres	Pseudo-slits per quadrant
LR blue, LR red	OFF	0.67"/fibre	54" x 54"	80 x 80	4
LR blue, LR red	ON	0.67"/fibre	27" x 27"	40 x 40	1
LR blue, LR red	OFF	0.33"/fibre	27" x 27"	80 x 80	4
LR blue, LR red	ON	0.33"/fibre	13" x 13"	40 x 40	1
MR, HR blue, HR orange, HR red	ON	0.67"/fibre	27" x 27"	40 x 40	1
MR, HR blue, HR orange, HR red	ON	0.33"/fibre	13" x 13"	40 x 40	1

Table 3.4: IFU spatial characteristics.

pseudo-slit corresponds to a region of  $20 \times 20$  pixels on the IFU head. An example of raw spectra on the CCD is shown in Figure 3.3.4: the vertical direction is the wavelength dispersion direction while the horizontal one is called cross-dispersion direction. The 400 spectra associated to a single bundle are arranged along the cross-dispersion direction following a given scheme and covering its entire length. The exact position of each pixel spectrum on the CCD can be found in the *IFU position tables* distributed with the data release. In the most general case, when all the fibers of a quadrant are illuminated, four blocks of spectra (one for each bundle) are created. The different blocks are arranged along the vertical direction on the CCD.

It is worth noticing that when observing with the Low Resolution (LR) Grisms all the pseudo-slits can be illuminated (multiplexing=4). In Medium and High Spectral Resolution mode (MR and HR respectively), a masking shutter is employed and only the central 1/4th of the IFU head is used. This means that only one pseudo-slit for each quadrant is illuminated.

The characteristics of the different IFU grism settings are illustrated in Table 3.4.

Due to the offset position of the IFU by respect to the pointing centre, the pointing coordinates in the header (RA and DEC) correspond to the centre of the VIMOS FoV while the relevant IFU pointing coordinates are indicated by the header keywords HIERARCH ESO TEL TARG ALPHA and HIERARCH ESO TEL TARG DELTA.

The spectral coverage and resolution of the six available grisms are shown in Table 3.5 and in Table 3.6, where the variations in spectral coverage from quadrant to quadrant are shown. Such variations depend on the exact position of the pseudo-slit in the focal plane.

The grism efficiency curves and the filter transmission curves associated to each observation mode can be found on the VIMOS user manual on the web page:

<https://www.eso.org/sci/facilities/paranal/instruments/vimos/doc/>

The efficiency curve of the new HR\_blue grism is shown in Figure 3.3.5. This grism is the one used to obtain the data presented in this thesis. It should be noted that the observations with the HR\_blue grism are filter free.

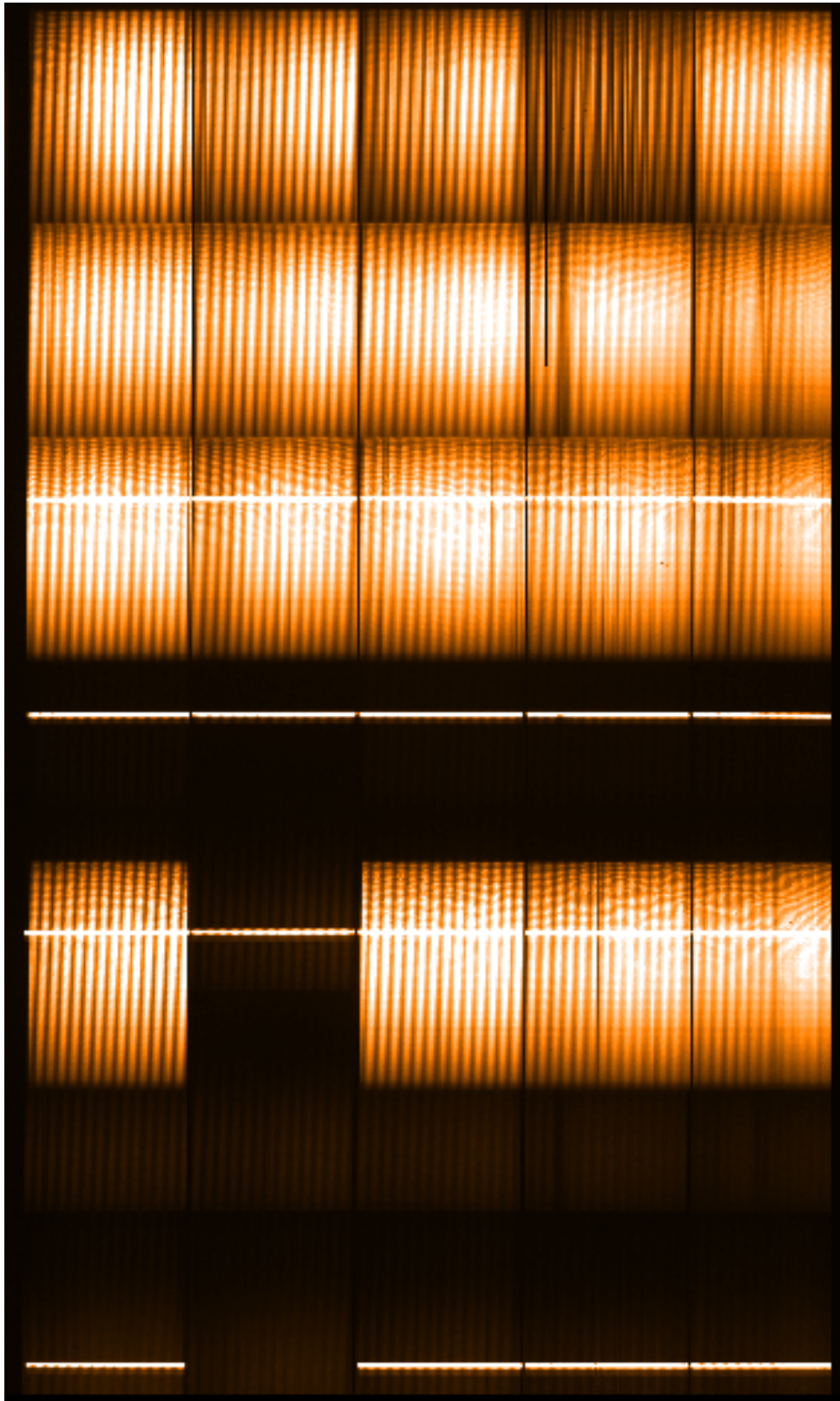


Figure 3.3.4: IFU raw spectra in one quadrant produced by a flat field exposure with a low resolution grism. As can be seen in the image, when all the pseudo-slits are illuminated the multiplex spectra belonging to different pseudo-slits contaminate each other to some extent.

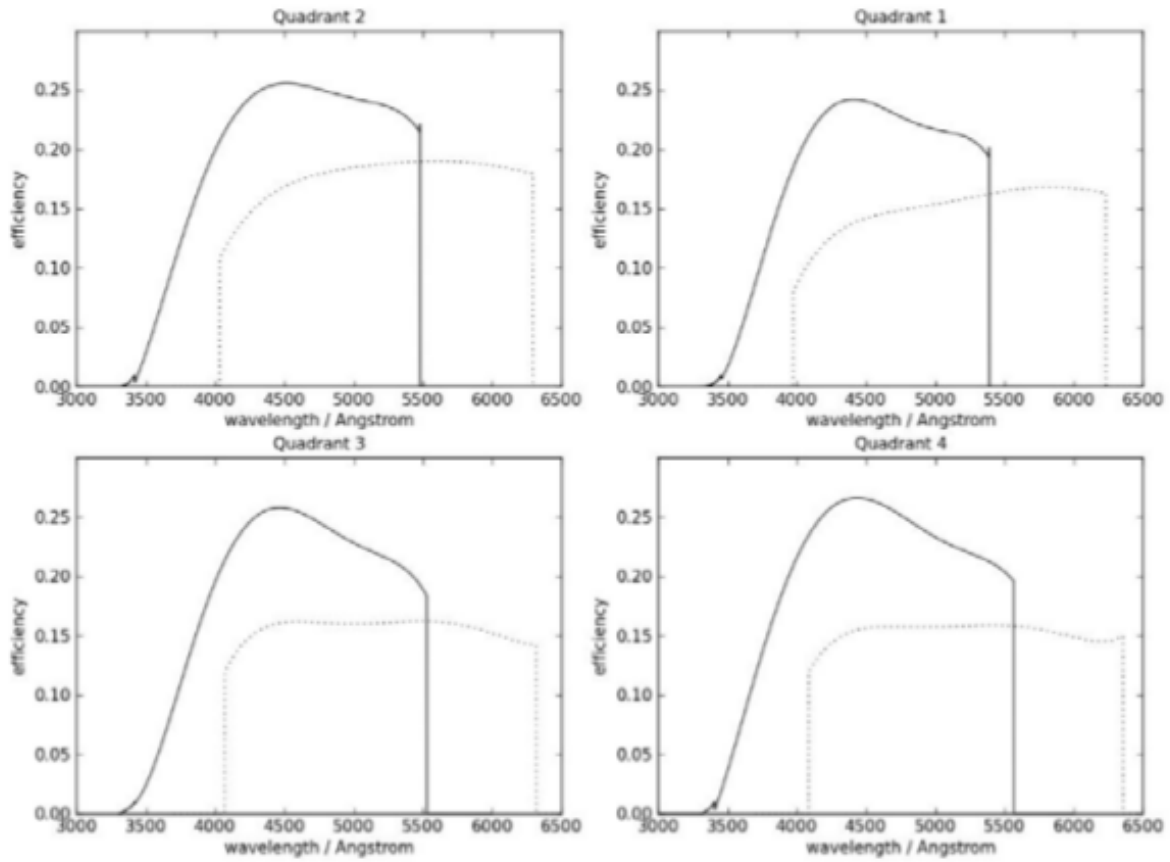


Figure 3.3.5: The efficiency of the old (dotted) and new (solid) HR\_blue gratings. The peak efficiency has increased by about 65% and has moved to approximately 440 nm.

Grism	Order sorting filter	Wavelength coverage common to all quadrants	Spectral resolution (1 fibre)	Dispersion (Å/pix)	Multiplex
LR blue	OS blue	400-670 nm	220	5.3	4
LR red	OS red	590-915 nm	260	7.3	4
MR	GG475	490-1015 nm	720	2.5	1
HR blue (NEW)	Free	370-535 nm	1440	0.71	1
HR orange	GG435	525-740 nm	2650	0.6	1
HR red	GG475	645-860 nm	3100	0.6	1

Table 3.5: IFU spectral coverage and resolution for each grism.

Grism	Q1	Q2	Q3	Q4
LR blue + OS blue	390 - 670 nm	395 - 675 nm	400 - 680 nm	400 - 680 nm
LR red + OS red	570 - 915 nm	580 - 930 nm	590 - 930 nm	585 - 930 nm
MR + GG475	485 - 1015 nm	490 - 1020 nm	490 - 1020 nm	490 - 1015 nm
HR blue (NEW) + free	370 - 537 nm	370 - 535 nm	370 - 550 nm	370 - 563 nm
HR orange + GG435	525 - 745 nm	525 - 745 nm	525 - 745 nm	525 - 740 nm
HR red + GG475	635 - 860 nm	635 - 865 nm	635 - 860 nm	645 - 875 nm

Table 3.6: IFU spectral coverage for each quadrant and each available grism.

## 3.4 VIMOS IFU observations: NGC 3557

### 3.4.1 IFU data calibration plan

NGC 3557 was observed on April 27 2012 at the VLT Unit3 Telescope equipped with VIMOS in IFU observing mode. The total exposure time is 3 hr including overhead. Given the maximum Observing Block (OB) length of 1 hr, the observation is splitted into three OBs, each including  $2 \times 17$  min on source and 26 min on overheads.

For a single Observation Block only one filter+grism configuration is allowed and the attached nighttime calibrations (arcs and flats) are mandatory for all IFU OBs. In order to take into account for instrumental flexures, arcs and flats are taken at the same rotator position as the science target. The so-called spectro-photometric standard stars can be observed within few nights before or after the science target observations using the same instrument setting used for the latter.

The OB files were inspected using GASGANO<sup>2</sup>, a software developed at ESO, able to handle data taken with all VLT telescopes.

Each OB includes data for all the four quadrants. For each quadrant a single Observation Block thus includes:

- Two science exposures ( $17' + 17'$ )
- Five Bias exposures
- Three Flat exposures
- One He + Ne Lamp exposure

A separate OB provides the data of the spectro-photometric standard star Feige110. The spectro-photometric standard star observation was performed on July 19 2012. This OB includes:

- One exposure of Feige110
- Five Bias exposures
- Three Flat exposures

---

<sup>2</sup>For a more accurate description and further informations refer to the webpage <http://www.eso.org/sci/software/gasgano/#Manual>.

All the observations were performed using the new HR\_blue grism<sup>3</sup> (see efficiency curves in Fig 3.3.5). The tabulated spectral resolution  $R = \frac{\lambda}{\Delta\lambda}$ <sup>4</sup>, given for the undeviated wavelength of 401.6 nm, is  $\sim 1440$  see Table 3.5. Spectra obtained with the HR\_blue grism cover a large part of the CCD area. For this reason a shutter masks the outer zone of the VIMOS FoV and only the central  $40 \times 40$  fibers are used (i.e. only one pseudo-slit is illuminated). The pseudo-slit centering can differ from quadrant to quadrant, due to this the spectral coverage can slightly vary depending on the quadrant (see Table 3.6). In Chapter 4 the actual spectral coverage obtained after wavelength calibration will be reported for each quadrant (see Table 4.1)

The spatial sampling selected for these observations is 0.67 arcsec/pixel resulting in a  $27'' \times 27''$  FoV, covering the central region of NGC 3557.

A flat field exposure is shown in Fig 3.4.1. The wavelength dispersion direction on the CCD is the vertical one, and the spectra cover about 60% of the entire CCD length in this direction. On the other hand, the CCD cross-dispersion direction is fully covered by the 400 spectra of each quadrant, with only a few outer pixels on both sides not illuminated (the so-called prescan regions), see *top panel* of Figure 3.4.2. The correspondence between the position of a spectrum on the CCD and a pixel in the FoV, is given in the so-called position tables distributed with the data release. The FWHM of a single spectrum on the CCD is about 4.5 pixels and the mean separation between adjacent spectra is 5 pixels (see Fig 3.4.2, *bottom panel*).

### 3.4.2 VIMOS/IFU performance

At Eso Headquarters in Garching calibration datasets are continuously processed in order to monitor the performance of the different instruments at Paranal. Quality Control plots for VIMOS are thus regularly produced and uploaded on the webpage:

<http://www.eso.org/observing/dfo/quality/VIMOS/qc/qc.html>.

Table 4.2 reports frequency and typical accuracy of the various IFU calibration observations.

In this section the performance of the VIMOS/IFU is described based on the Quality Control (QC) plots obtained during the period of our IFU observations.

The Bias level is continuously monitored, and is about 200 ADU<sup>5</sup> for all the quadrants showing in general a stable trend, with little instabilities present for Q2 only. The Gain (conversion factor from ADU to electrons), also shows a quite stable trend with time. In April 2012 its value is about 1.85 e<sup>-</sup>/ADU for all the quadrants. The lamp stability plots check for the quality of arc and flat field lamps. The QC plot for the arc lamp shows the He line flux for the different quadrants: while this value is comparable for Q3 and Q4, it increases in the remaining quadrants reaching the largest values for Q1. The flat field lamp performance is monitored using IFU spectroscopic flats: the QC plot is shown in Fig 3.4.3. In April 2012 the flux for Q1, Q3 and Q4 is about  $14\text{-}15 \times 10^5$  ADU/sec, while for Q2 the value is slightly below  $12 \times 10^5$  ADU/sec.

<sup>3</sup>A new set of four holographic HR\_grisms installed on March 15 2012.

<sup>4</sup>The resolution is given by the ratio between a line wavelength and its Full Width at Half Maximum

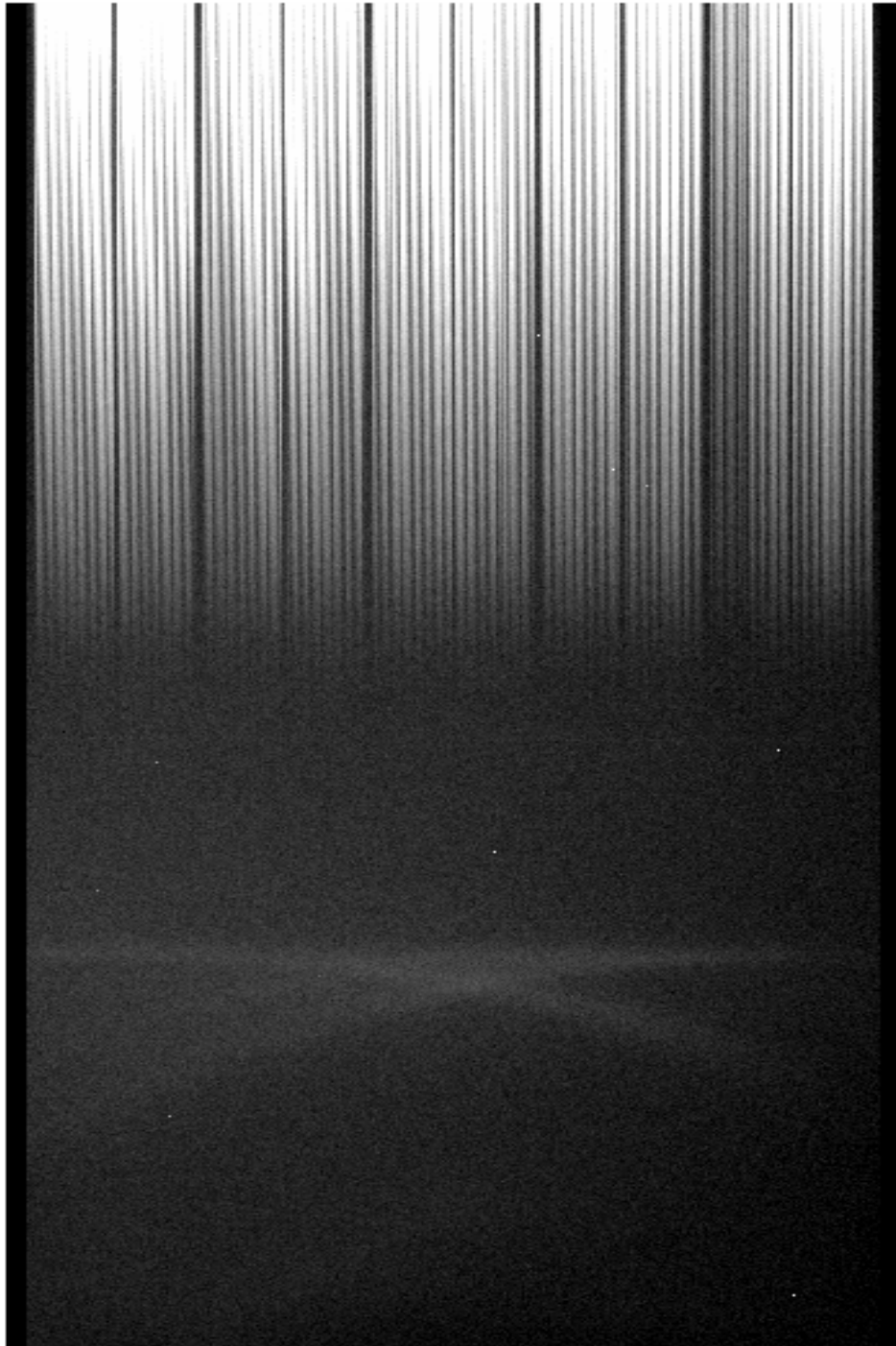


Figure 3.4.1: Flat Field exposure for Q1. In the lower part of the CCD scattered light is visible. This part of the CCD is masked during the data reduction. The few saturated pixels are Cosmic Rays events.

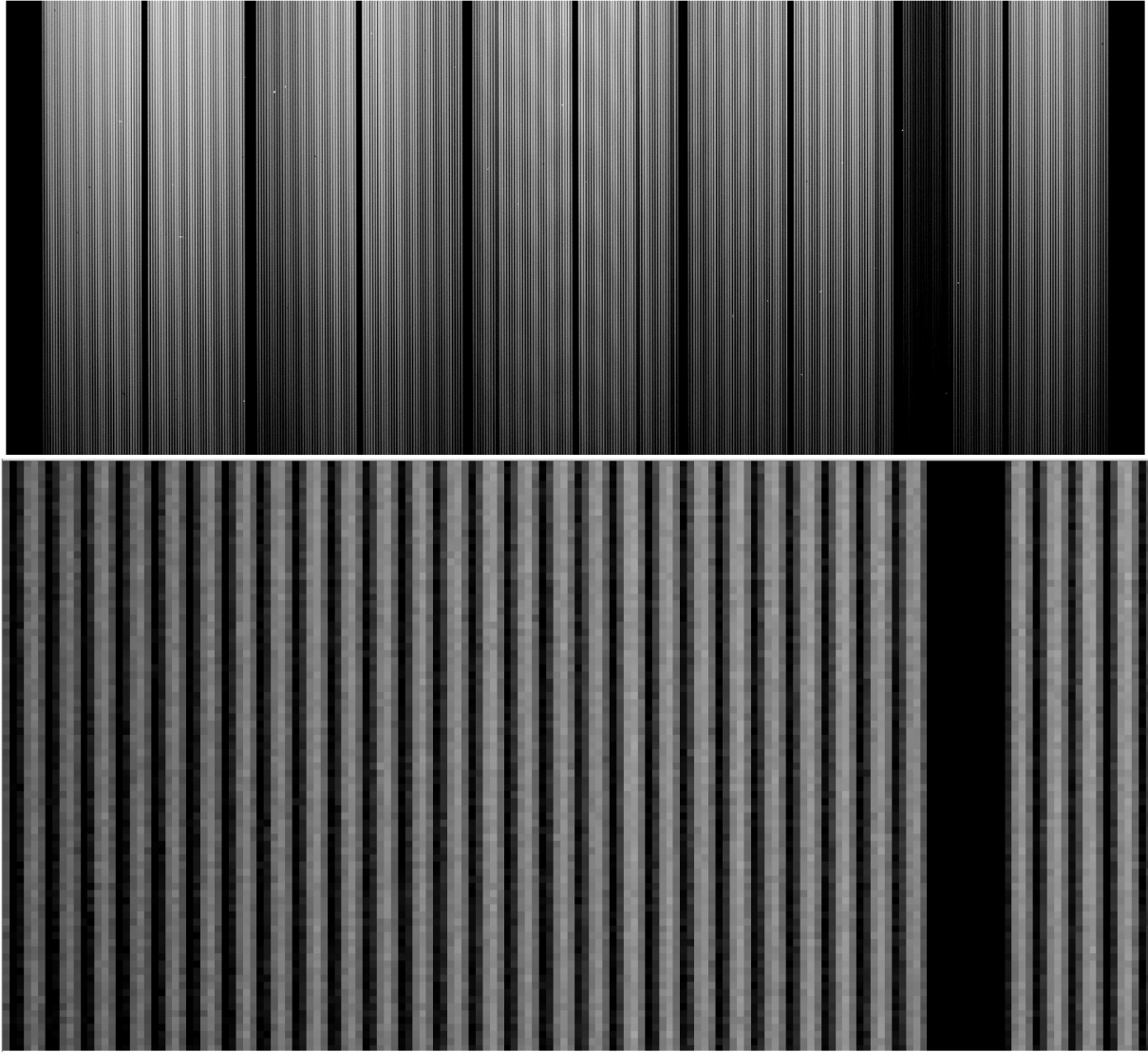


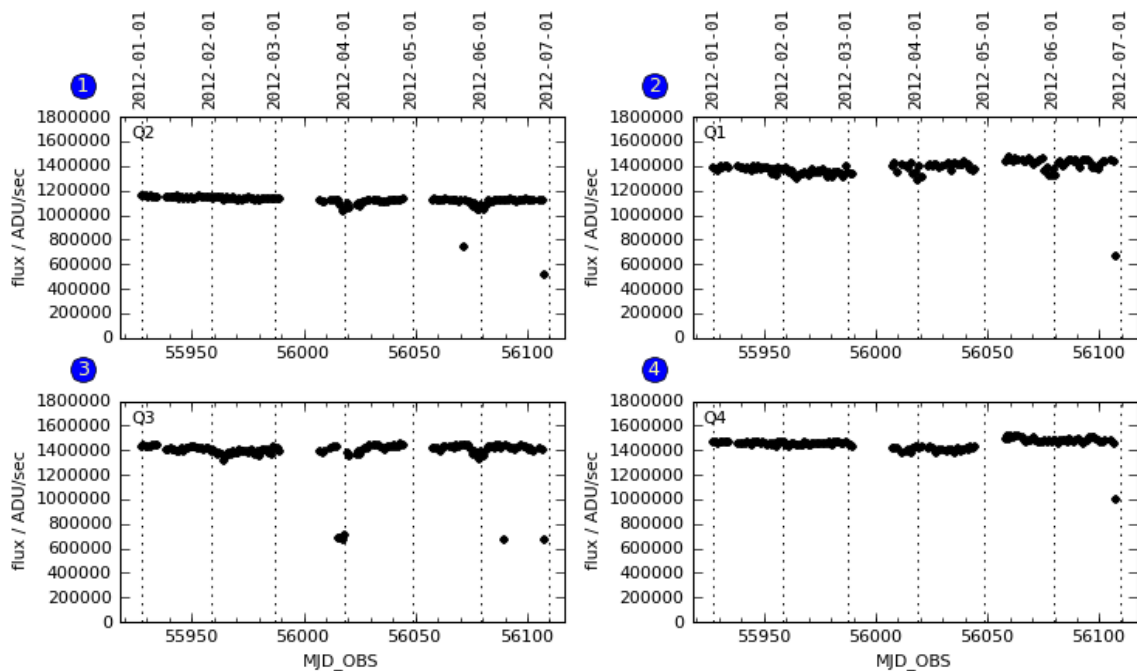
Figure 3.4.2: Two different zooms of a restricted area of the Flat Field exposure shown in Fig 3.4.1. In the *top panel* the outer prescan regions are visible, while the *bottom panel* shows the typical spectrum width and separation between adjacent spectra.

Calibration	Number	Frequency	When?	Products	Accuracy <sup>1</sup>	Comment
Bias	5	Daily	Day time	Master Bias	RON	
Darks	3	Monthly	Day time	Dark current		
Screen Flats	3	Daily	Day time	IFU Flat with HR Orange		Monitoring
Screen Arc	1	Daily	Day time	IFU Arc with HR Orange		Monitoring
Screen Flats	1 to 3	Attached to all science OBs		IFU Flat	5 %	
Screen Arcs	1	Attached to all science OBs		Dispersion coeff.	0.3 pix	
Specphot. Standard Star	4 quadrants	Weekly	Night time	Response function	10%	All grism+filter setups used

<sup>1</sup>The reported accuracy does not consider the instrument flexures.

Table 3.7: In the table is described the nature, frequency and accuracy of different calibrations.

VIMOS: QTH50 FF lamp (180 days period)  
QC data range: 2012-01-01 ... 2012-06-30



powered by QC: [www.eso.org/HC](http://www.eso.org/HC)

created by trendPlotter v3.0.1 on 2012-07-15T03:10:00

Figure 3.4.3: QC plot for the flat field lamp. The quadrant is indicated at the top-left side of each plot. The flux level is measured in ADU/sec and plotted against time from January 01, 2012 to July 01, 2012.

VIMOS: rms of IDS, IFU HR\_blue (90 days period)  
 QC data range: 2012-04-01 ... 2012-07-01

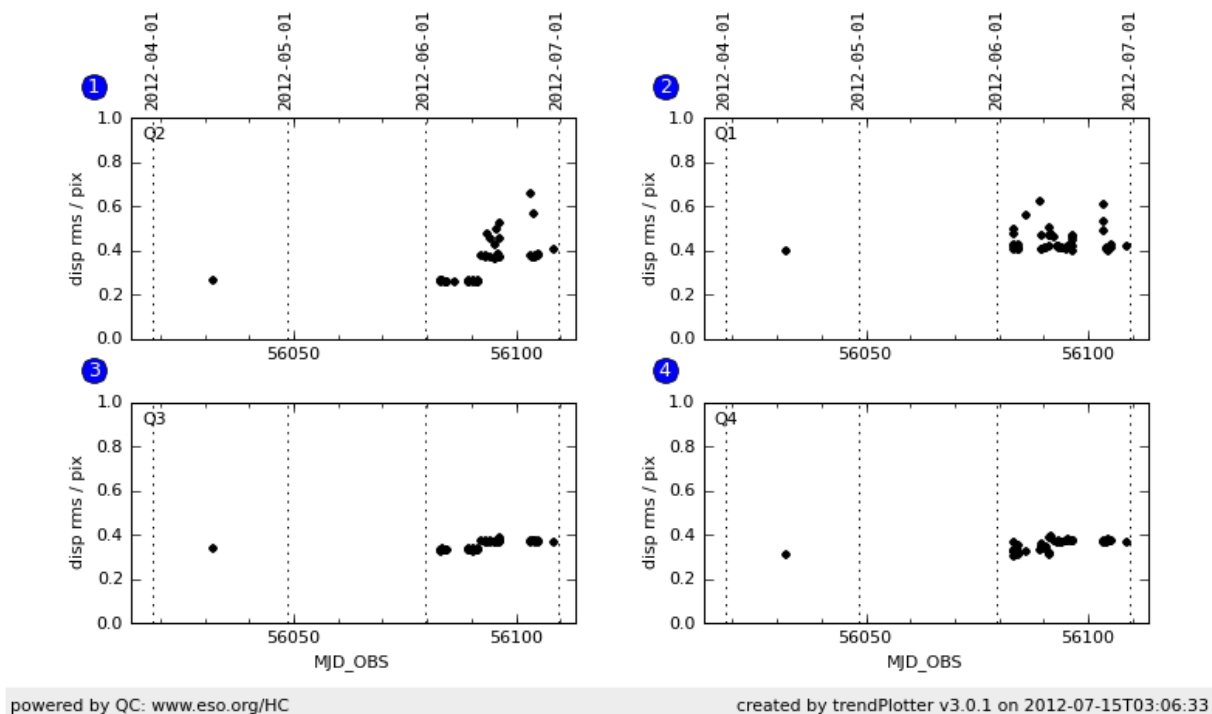


Figure 3.4.4: QC plot for the rms of the dispersion solution for IFU HR\_blue calibrations. The quadrant is indicated at the top-left side of each plot.

The RMS of the wavelength dispersion solution is reported in Fig 3.4.4. As can be seen little variations in the accuracy of the dispersion solution are found between different quadrants although they remain confined within  $<1\text{px}$ . However, since the dispersion solution is usually very stable, any values above 0.4 pixels (depending on the setting) can be a concern.

Due to instrumental effects the spectra on the CCD can display curvature along the Y direction. For IFU spectra curvatures are typically in the range  $\pm 10$  pixels.

The QC plot relative to spectral resolution is shown in Fig 3.4.5, the R value is extracted from IFU arc lamp measurements for different sections of the observed spectral range. The mean resolution is  $R = \frac{\lambda}{\Delta\lambda} = 1650$  at about  $4400 \text{ \AA}$ , it corresponds to  $2.7 \text{ \AA}$ .

A fiber is defined “lost” when it is not successfully found, traced, and wavelength-calibrated during IFU calibrations. The number of lost fibers per quadrant lies in the range 20-40 fibers, these are typically fibers associated to the edge of the FoV. During the observation period (April 2012) the second quadrant shows a larger number of lost fibers (reaching the value of 100 fibers) in QC plots, this was confirmed during our data analysis.

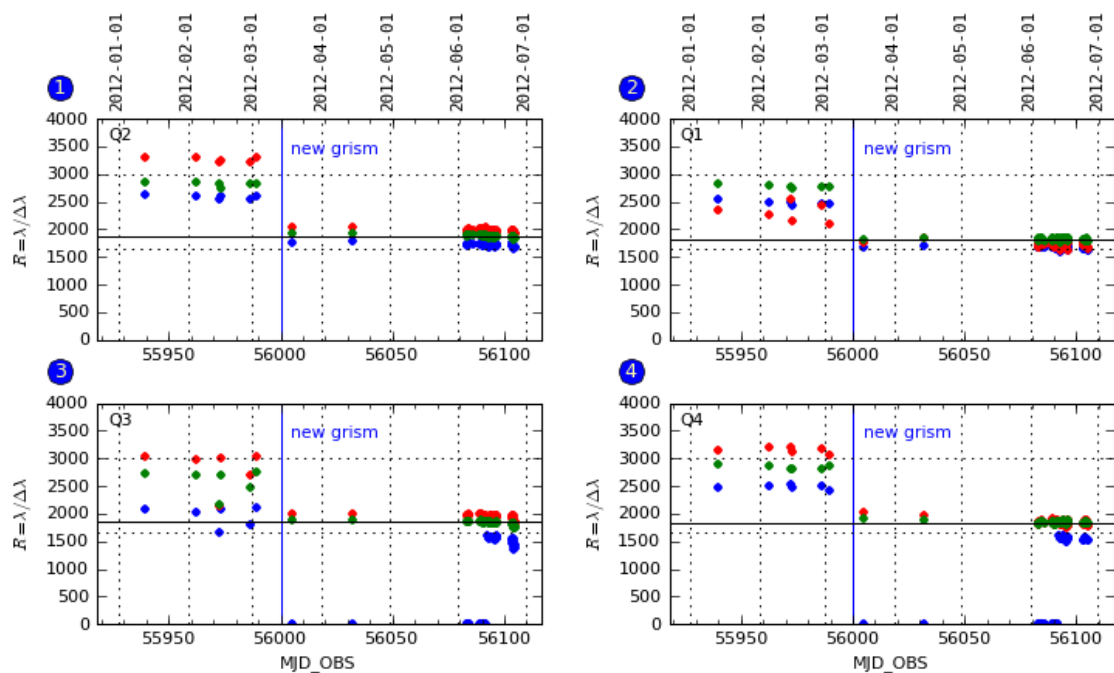
The last relevant parameter is the overall IFU efficiency measured using spectrophotometric standard stars. As can be seen in Fig 3.4.6, the efficiency varies from quadrant

(FWHM, Gaussian fit), averaged over all arc lamp lines.

<sup>5</sup>The intensity of the signal is provided in counts, using the analog-to-digital unit (ADU).

## VIMOS: resolving power, IFU HR\_blue (180 days period)

QC data range: 2012-01-01 ... 2012-06-30

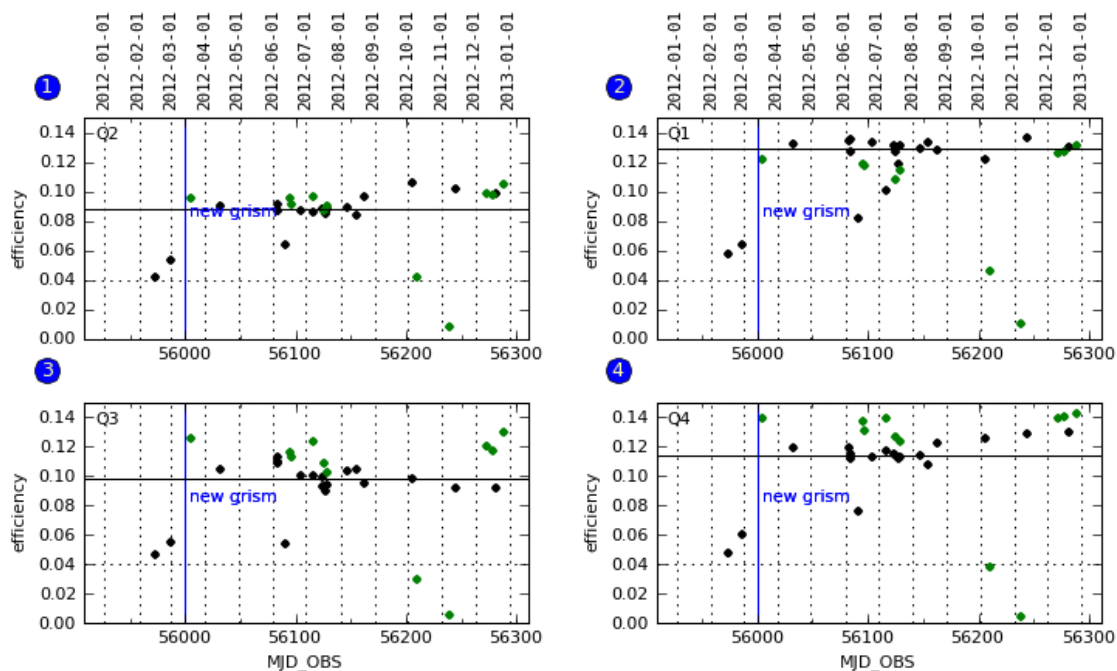


powered by QC: [www.eso.org/HC](http://www.eso.org/HC)

created by trendPlotter v3.0.1 on 2012-07-15T03:07:49

Figure 3.4.5: QC plot showing the spectral resolution of the HR\_blue grism. The measurements are performed in different sections of the spectral range. The blue, green and red points indicate the R value for the bluest, the central and reddest parts of the spectral range respectively. The vertical blue line corresponds to the date when the new HR\_blue grism was installed, the average R value for the new grism is indicated by a solid line. The quadrant is indicated at the top-left side of each plot.

VIMOS: IFU efficiency, HR\_blue (365 days period)  
 QC data range: 2012-01-01 ... 2013-01-01



powered by QC: [www.eso.org/HC](http://www.eso.org/HC) created by trendPlotter v3.2 on 2013-01-13T03:14:24

Figure 3.4.6: IFU efficiency at 4500 Å using HR-blue grism. Both IFU magnification configurations are plotted: 0.67 arcsec/pixel correspond to black dots, 0.33 arcsec/pixel correspond to green dots. The average is indicated by the solid line while the vertical blue line corresponds to the date when the new HR\_blue grism was installed. The quadrant is indicated at the top-left side of each plot.

to quadrant due to the fact that different instrumentation is used for each quadrant. This turned out to be a crucial issue for the flat fielding and flux calibration of our target (see Chapter 4 for more details).

The seeing measured for the different exposures during our observations (two exposures for each Observing Block) is reported in Table 3.8. The seeing values are reported in the keywords HIERARCH ESO TEL AIRM START and HIERARCH ESO TEL AIRM END in the Header of each exposure file.

Exposure	Initial seeing (")	Final seeing (")
OB1-Exposure1	1.08	0.95
OB1-Exposure2	1.01	0.71
OB2-Exposure1	1.46	1.30
OB2-Exposure2	1.36	1.36
OB3-Exposure1	0.80	1.15
OB3-Exposure2	1.25	0.96

Table 3.8: Seeing in arcsec measured at the beginning and at the end of each exposure.

# Chapter 4

## NGC 3557: VIMOS/IFU Data Reduction

### 4.1 P3D

The data reduction of the IFU NGC 3557 dataset was carried out using P3D<sup>1</sup>, a data reduction tool optimized for Integral Field Unit data. A collaboration with the Potsdam group was established in the framework of this thesis to update P3D, and configure it to work with the new VIMOS Hr\_blue grism data. The new version of P3D (version 2.2.1) was released on January 21 2013.

P3D routines are written using the Interactive Data Language (IDL) programming language and are able to perform the following tasks:

- Creating a master-bias image (alternatively prescan and overscan regions can be used, if available).
- Removing cosmic-ray hits from the raw data.
- Automatically find and trace spectra on the detector.
- Creating a dispersion mask for wavelength calibration.
- Creating a dataset that is used to normalize (flat field) the extracted spectra.
- Extracting science-object data, using different extraction methods.
- Deriving a sensitivity function from a summed standard-star spectrum.
- Flux calibrating extracted data using a sensitivity function.
- Combining extracted images of separate detectors into a single image.
- Correcting data for effects introduced by differential atmospheric refraction (DAR).

---

<sup>1</sup>P3D is a general data-reduction tool for fiber-fed Integral-field spectrographs developed at the Astrophysikalisches Institut in Potsdam (Germany). It can be freely downloaded at the project web site <http://sourceforge.net/projects/p3d/>.

- Converting RSS-formatted<sup>2</sup> P3D outputs to data cubes.
- Combining extracted images from different exposures of the same region.

P3D also provides graphical tools e.g. the so-called *Spectrum Viewer* and the *Image Viewer*, for data inspection.

The main reduction steps (Master Bias, Trace Mask, Dispersion Mask, Fiber flat, and Extract object) can be performed using the *Graphical User Interface* (GUI). The flux calibration and other operations are performed from the command line. The setting of the parameters used by the different routines is managed by two files: the *Instrument-Parameter File* and the *User-Parameter File*. In the *Instrument-Parameter File* are listed the main parameters for the instrument setting. It is selected by the *Quick instrument setup tab* when the GUI starts. The *User-Parameter File* contains all the modifiable entries that are used by P3D tasks. A set of tables is attached to P3D the package, which contain the needed informations to rearrange the spectra of each quadrant in the correct way, and reconstruct the entire FoV.

## 4.2 Data reduction steps

### 4.2.1 Overview

The various reduction steps are illustrated in the following sections in the order they are performed. The same reduction scheme is applied both for the NGC 3557 dataset and for the spectro-photometric standard star. Here is a summary of the reduction steps performed for each OB.

1. Master Bias creation
2. Tracing of the spectra
3. Dispersion-mask creation for wavelength calibration
4. Extraction of flat field spectra, used to estimate the correction for flat field and for transmission efficiency
5. Extraction of the spectra and application of the previously derived calibrations and corrections
6. Measure of the sensitivity function
7. Flux calibration
8. Combination of the extracted spectra in the four quadrants into a single RSS file covering the entire FoV
9. Differential Atmospheric Refraction (DAR) correction
10. Combination of the different exposures

---

<sup>2</sup>In a raw exposure, each spectrum is 4-5 pixel wide on the CCD, after the extraction the spectrum is concentrated in a single pixel (Raw Stacked Spectrum RSS format).

Quadrant	Spectral Coverage
Q1	3750-5300 Å
Q2	3750-5300 Å
Q3	3850-5500 Å
Q4	3650-5600 Å

Table 4.1: Spectral coverage for each quadrant as derived from the wavelength calibration of our data.

#### 11. Conversion of the final RSS file into a Datacube

The reduction process for the spectro-photometric standard star Feige110 includes steps (1-6) while for NGC 3557 all the steps are performed (1-11) except step (6). Steps (1-7) are performed for each quadrant separately, the final images are then combined in step (8). For NGC 3557 step (5) and steps (7-9) are performed separately for the two available exposures in each OB.

As mentioned in Section 3.4.1, the pseudo-slits on the four quadrants are positioned in a slightly different way, resulting in slightly different spectral coverages. This effect was quantified for our dataset and the actual spectral coverage of each quadrant is reported in Table 4.1. It is worth noticing that this effect is most notable for quadrant Q4, where all the spectra are shifted along the Y axis and cover a larger wavelength range with respect to the other quadrants.

Due to this, the Instrument Parameter File was edited in order to make it possible to read a longer portion of the CCD along the Y direction.

### 4.2.2 Master Bias and Tracing of the spectra

The first step is the creation of a master bias image from the five bias exposures available for each OB. The latter are selected through the P3D GUI and combined using the min/max average method. Before performing the average of the counts in a single pixel, the minimum and the maximum values are discarded. In this way a Master Bias image is created. The Master Bias is then subtracted from all images produced by the reduction steps.

A crucial step in the data reduction is the correct localization of each spectrum on the CCD in both cross-dispersion and dispersion direction. This process is called “spectral tracing”. It essentially creates a trace-mask image that is then used as a guide when extracting the spectra from the science exposures. The spectral tracing is carried out using a well illuminated exposure where spectra are clearly visible across the full wavelength range: flat field exposures are thus used for this scope. The three flat field exposures available of each OB are first combined using the min/max average method, the Master Flat is then used as the input file to the tracing routine.

An important effect to take into account working with Integral Field Spectroscopy data is the so-called fiber to fiber cross-talk. Tightly packing the fibers into the pseudo-slit (and consequently the spectra on the CCD), in order to maximize the number of available fibers, comes at a price. The overlap between spectra of adjacent fibres can lead to a significant cross-contamination (cross-talk) between fibers, that compromises the extraction process. Sharp & Birchall (2010) report an extraction method that takes into account the interaction between adjacent fibres and provides a statistically optimized

estimate of the true intensity for each fiber spectrum. This method is named multi-profile deconvolution (MPD) optimal extraction method (see Sharp & Birchall 2010 for a more accurate description of the cross-talk effect and the MPD algorithm). In order to use the MPD optimal extraction method it is necessary to derive very accurate line profiles during the tracing.

The tracing process is split into two steps. First all the spectra are identified as local maxima along the cross dispersion direction for a given pixel along the dispersion axis (approximately the central one). To optimize the extraction and reduce the effect of noise, cosmic ray hits or detector sensitivity variations the spectra are searched for in a set of adjacent pixels with respect to the given one.

The sequence of maxima found in this way is then cross-correlated with a pre-defined instrumental pattern. The latter contains information about the expected separation and number of spectra. The routine can indeed fail in finding some spectra on the flat field exposure due to dead, low transmission or unused fibres. The positions of missing spectra are thus interpolated or extrapolated from the nearest spectrum found in order to have a total number of spectra equal to the expected one. Spectra positions related to dead or low transmission fibers are stored in specific tables, and are excluded in the following steps of the reduction. Finally a more accurate position for each spectrum is calculated by weighting the identified sequence of local maxima with the cross-dispersion profile of the data (see Sandin et al. 2010 for a full description).

As a second step, the routine starts from the just identified weighted positions to calculate the position of each spectrum along the entire dispersion direction. After grouping the 400 spectra in a single quadrant in 5 groups of 80 spectra each, a cross-dispersion profile fit is performed for each group of spectra. Starting from the first pixel, the cross-dispersion profiles are determined every 20 pixels along the dispersion direction. The widths and the intensities for all the remaining pixels are interpolated. A trace-mask is thus created and stored; such mask will be used to localize and correctly extract the spectra from all the exposures in the further reduction steps.

At the end of the first tracing step it is possible to graphically inspect the result of the cross-dispersion fit performed for the selected pixel, in order to visually identify possible failures of the routine. Fig 4.2.1 shows an example extracted from one of the plots produced by the routine.

### 4.2.3 Creation of the Dispersion-mask

A very important step of the data reduction is the creation of a dispersion-mask using the He + Ne arc lamp exposures in order to calibrate the science data. A raw lamp exposure is shown in Fig 4.2.2. A tabulated spectrum of the same arc lamp is shown in Fig 4.2.3.

Using the trace-mask, the spectra of the raw lamp exposure are first extracted with a MPD optimal extraction method. The extracted spectra are then visually inspected in order to check the accuracy of the extraction process. When the extraction is fine tuned, the dispersion-mask creation GUI tool is launched. Before the GUI is started both a line-list file and a spectral coverage range are selected following the Instrument-parameter File setting in order to determine a first-guess solution with a constant dispersion across the wavelength direction.

As shown in Fig 4.2.4, the dispersion-mask creation tool GUI is constituted of two

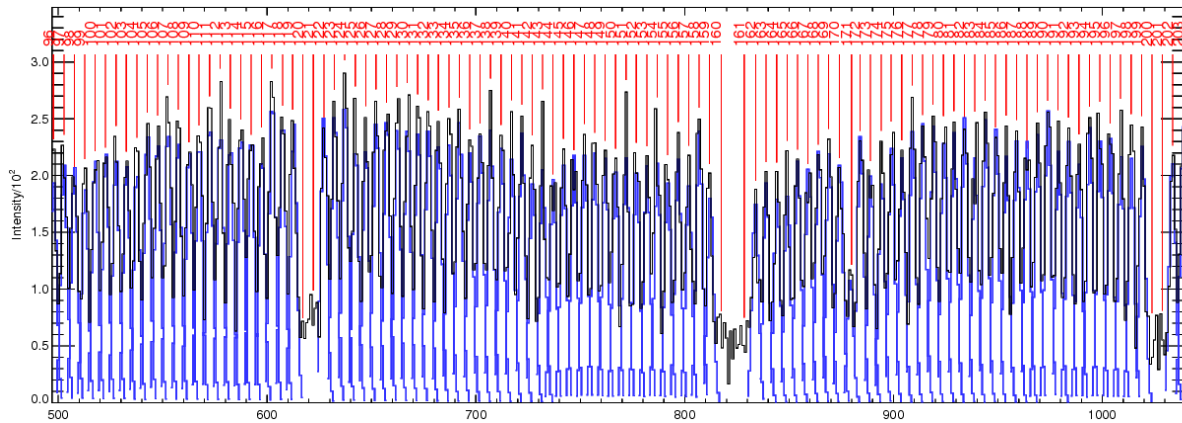


Figure 4.2.1: An example of the plots created by the tracing routine showing the results for a group of spectra along the cross-dispersion direction. The intensity of the spectrum profiles [ADU] is plotted against the pixels along the cross-dispersion axis of the CCD (black line). The cross-dispersion profile fit (blue line) is shown together with the fitted centre of each spectrum (red vertical line).

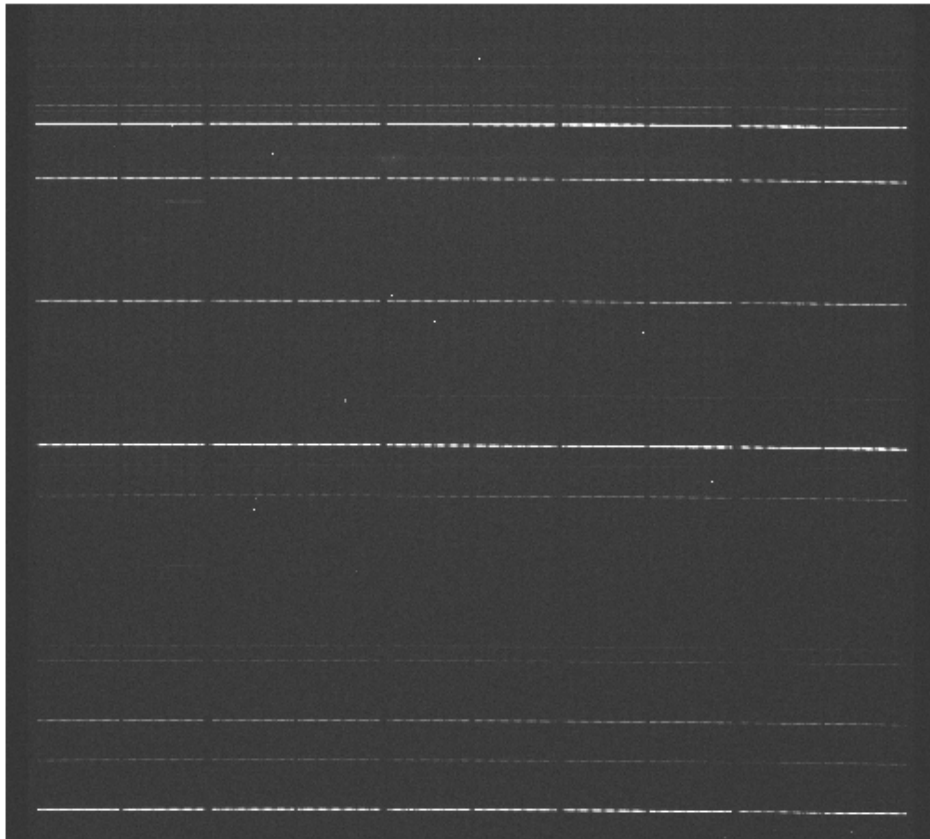


Figure 4.2.2: A raw arc lamp exposure relative to the first quadrant. Emission lines are clearly visible crossing the entire cross-dispersion direction on the CCD.

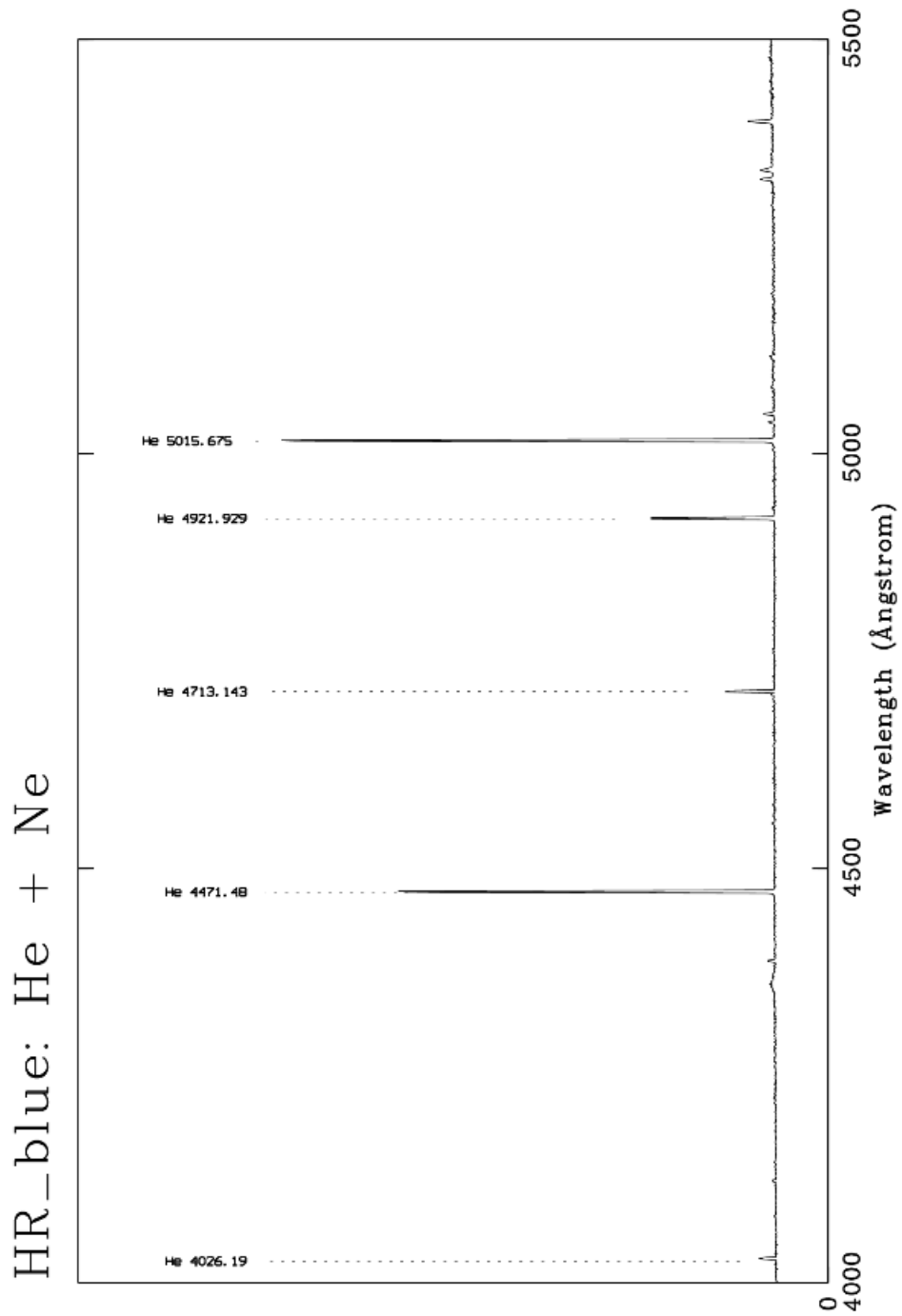


Figure 4.2.3: HR blue arc line spectrum from 4000 to 5500 Å. The tabulated lines are indicated.

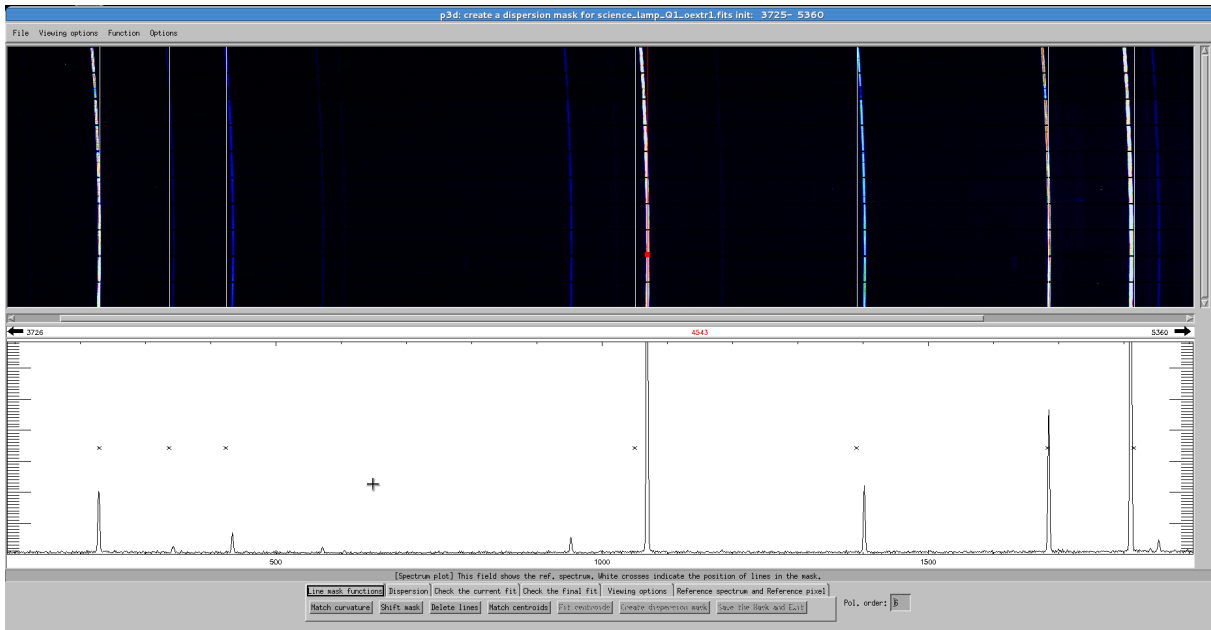


Figure 4.2.4: The dispersion-mask GUI tool.

panels.

The top panel shows the Raw Stacked Spectrum (RSS) image of the arc lamp extracted spectra (shorter wavelength are on the left side). The vertical white lines represent the position assigned by the first-guess solution to each input spectral line. A reference spectrum is shown in the lower panel. The first-guess solution line positions are here marked by crosses. As can be clearly seen in Figure 4.2.4, the spectra show a significant curvature (upper panel) and the first guess positions (crosses in the bottom panel) do not always match the actual position of the emission lines. In order to get a better dispersion-mask, one can interactively make a number of changes through a set of control buttons (see lower part of the plot).

The main actions controlled by the control buttons are:

- Shift mask

The line mask can be linearly shifted along the dispersion axis to match a larger number of spectral lines.

- Delete Lines

Saturated and faint arc-line entries can be deleted together with lines that are not present in the spectra. In Table 4.2 the input line entries are listed, the ones employed for the final dispersion-mask creation are also indicated.

- Manual Dispersion

The instrument does not have a constant dispersion across the wavelength range, and just shifting the first-guess dispersion solution does not help in matching more lines. A manual dispersion solution can be therefore created by manually shifting each cross symbol closer to the actual position of its related emission arc line (see Figure 4.2.5). Then a rational spline is fitted to create a better pixel-wavelength correspondence.

Wavelength [Å]	Number	Located
3888.649902	1	yes
3964.729004	2	no
4026.189941	3	yes
4471.479980	4	yes
4713.143066	5	yes
4921.929199	6	yes
5015.674805	7	yes
5290.740	8	no
5316.776	9	no

Table 4.2: Input line entries used for the first-guess solution. The ones actually employed for the final mask creation are indicated in the last column. The 3964 Å line is too faint to be used to create an accurate dispersion solution, while the other not used lines are not present in the spectra.

- Match Curvature

The spectrum curvatures shown in Figure 4.2.4 (upper panel) are due to differences in the light optical paths to each fiber. Two arc lines, one in the red part and the other in the blue part of the spectrum, are selected on the RSS image. The curvature is then calculated by maximising the flux along the selected lines and assuming that the dispersion changes linearly with wavelength. At the end of the procedure the white vertical lines appear curved, and provide a better match of the curvature of the arc lines (see Figure 4.2.5).

- Match Centroids

The function “Match Centroids” calculates the distance between an intensity peak and the assigned line pixel position. This distance is checked against tolerance values set in the *User-Parameter File*. New arc line positions, weighted by their relative intensities are then calculated.

- Fit Centroids

Once the line positions are optimised, a more accurate fitting is performed for each line in the spectrum. Using a Gaussian profile a cross-dispersion line centre position is calculated, and is substituted to the previously estimated peak position.

- Check the current mask fit

This is a consistency check. This function allows to check the dispersion solution for the reference spectrum. The polynomial fit to the arc line pixel positions and the fit residuals (see Figure 4.2.6) can be inspected in order check to understand if the polynomial order is appropriate and if the fitting is sufficiently accurate. The residuals are calculated following the relation:

$$Residual = \lambda_{tabulated} - \lambda_{fitted} \tag{4.2.1}$$

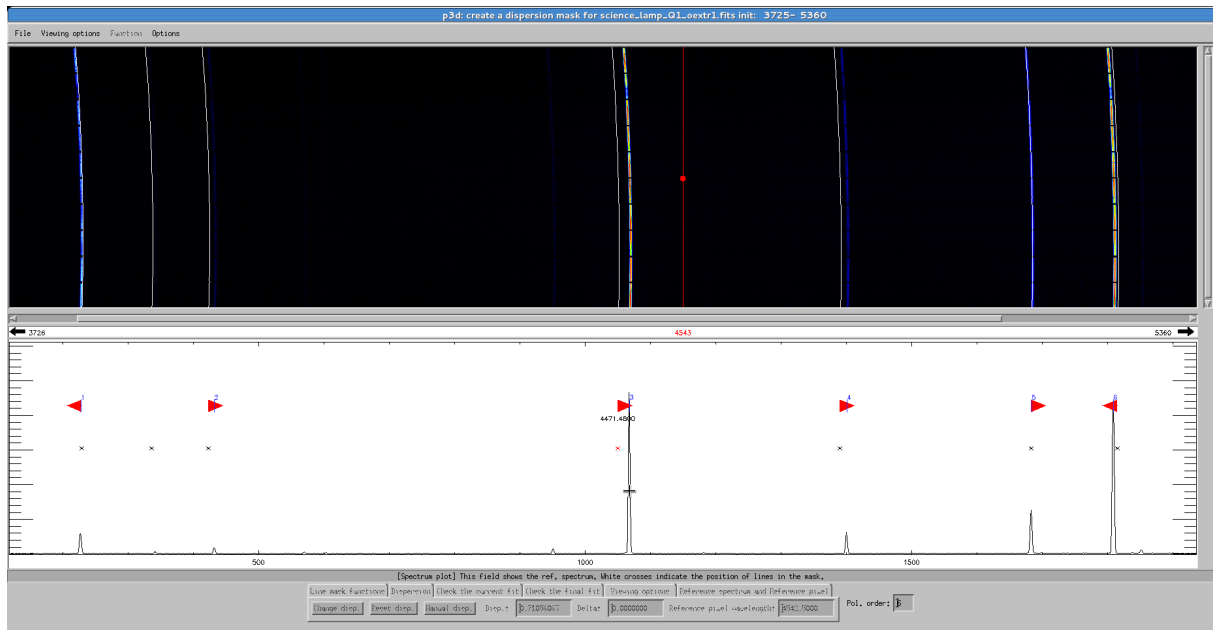


Figure 4.2.5: Same plot as in Figure 4.2.4, the red arrows in the bottom panel indicate the shifted line positions by respect to these obtained after the first-guess solution (crosses in Figure 4.2.4). After applying the curvature matching the white lines appear curved in the upper panel.

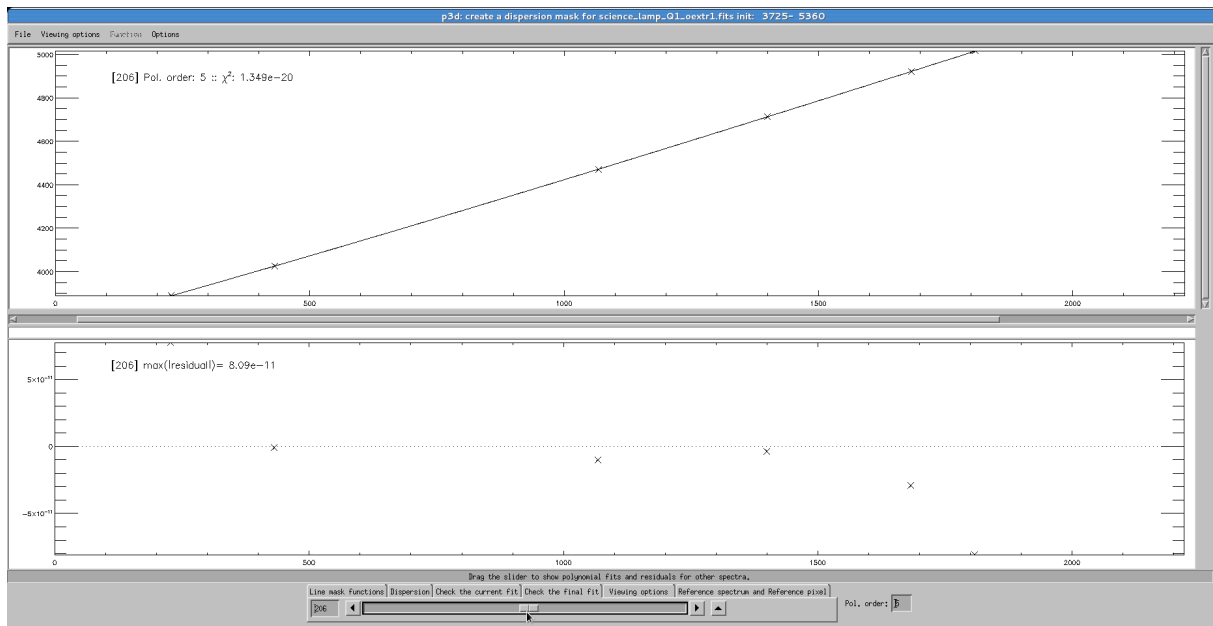


Figure 4.2.6: A snapshot of the GUI during the fit check. The RSS plot in the upper panel is substituted by the dispersion solution plot. The polynomial fit is drawn with a solid lines while arc line entries are indicated with a cross. The wavelength in  $\text{\AA}$  is on the Y axis, the number of the pixel on the X one. In the upper left corner are reported also the spectrum number in brackets, the polynomial fit order, and the chi-square number of the fit. In the lower panel the residuals plot appears, the residual values for the marked pixels are measured in  $\text{\AA}$ . The horizontal dotted line mark the zero level while in the upper left corner are shown the spectrum number in brackets and the maximum residual value of the shown spectrum.

	$\sigma_{\text{res } 1} [\text{\AA}]$	$\sigma_{\text{res } 3} [\text{\AA}]$	$\sigma_{\text{res } 4} [\text{\AA}]$	$\sigma_{\text{res } 5} [\text{\AA}]$	$\sigma_{\text{res } 6} [\text{\AA}]$	$\sigma_{\text{res } 7} [\text{\AA}]$	max res [ $\text{\AA}$ ]
<b>Q1</b>	0.557	0.240	0.118	0.171	0.360	0.587	1.63
<b>Q2</b>	0.667	0.276	0.125	0.194	0.407	0.681	1.96
<b>Q3</b>	0.558	0.239	0.129	0.171	0.349	0.589	1.75
<b>Q4</b>	0.615	0.258	0.117	0.118	0.389	0.640	1.73

Table 4.3: Accuracy of the dispersion solutions for the four different quadrants.  $\sigma_{\text{res } n}$  indicates the RMS values of the residuals for each line where  $n$  corresponds to the progressive number indicated in Table 4.2. The last column reports the maximum residual value found over all the spectra of a single quadrant.

- Create dispersion mask, check the final fit, Save and Exit

When happy with the mask fitting the final dispersion mask can be created and checked.

The dispersion solution is checked for all the spectra: wavelength residual values or abrupt changes in the polynomial fit trends should not be present.

The dispersion mask can then be saved in an output file, that will be used for the wavelength calibration of the science data during the extraction process.

Table 4.3 reports the residual of the final dispersion solution applied to our datasets. RMS residuals are of the order of a few tenths  $\text{\AA}$  and always well below the nominal 2.7  $\text{\AA}$  instrumental dispersion. However the accuracy of the dispersion solution tend to degrade going towards the (blue and red) edges of the spectral range covered.

#### 4.2.4 Flat fielding and transmission corrections

After the creation of a dispersion solution for all the spectra, the flat field exposures are used in order to correct for variations in sensitivity over the detector surface (flat fielding correction) and for light transmission efficiency of fibers (transmission correction). Such corrections will be applied during the spectra extraction (see Section 4.2.5).

As a first step the flat field raw exposures are combined with the min/max average method, and a master flat image is created. Using the trace-mask previously created, all the spectra are extracted from the master flat field image using a MPD optimal extraction method. In order to perform a wavelength dependent normalization, all the spectra are divided by the estimated mean spectrum. In this way a normalized image reflecting the instrumental spatial sensitivity is obtained. Although this first normalization accounts for fiber-to-fiber efficiency variations, a more accurate fibre-to-fibre correction is calculated. For each spectrum an intensity is calculated summing up the intensity values of all the pixels across the dispersion direction. All the values thus obtained (one value for each spectrum) are divided with their mean value. Doing so each spectrum/fiber can be associated to a normalized value representing its transmission efficiency. A transmission array is then created and saved. Low signal regions on the CCD can affect the integrated intensity of some spectra; for this reason about 30% of the pixels from the lower CCD part and 5% from the upper CCD part are excluded before the transmission correction estimate.

It should be noted that, during both processes, dead or low transmission fibers are not considered.

The extracted flat field image is also wavelength calibrated using the previously created dispersion mask. In this way possible problems related to this correction on the final scientific image can be identified with a better accuracy.

#### 4.2.4.1 Importance of flat-fielding correction for our NGC 3557 dataset

Due to the complicated arrangement of the spectra on the CCD, the flat fielding correction is often ignored in IFS data reduction (see e.g. in Gruyters et al. 2012 and Westmoquette et al 2011). Indeed the official ESO VIMOS pipeline (GASGANO) can perform only a transmission correction on the science data.

A first data reduction of this dataset was performed using GASGANO. However the sensitivity variations over the CCD affected the data in a considerable way, causing inconsistencies during the flux calibration process. This was due to the fact that the instrumental sensitivity changed significantly between the observation of the spectro-photometric standard star and of NGC 3557. The lack of a flat fielding correction for both the exposures yielded inconsistencies when applying the flux calibration to each quadrant. For this reason we decided to repeat the data reduction with the P3D software which includes the flat fielding correction.

#### 4.2.5 Extraction of the spectra

The main steps of the extraction procedure are listed below:

1. Master Bias subtraction
2. Cosmic ray removal
3. Cross-dispersion line profiles recentering
4. Scattered light subtraction
5. Spectra extraction
6. Recentering on the dispersion axis and wavelength calibration
7. Flat field correction
8. Transmission correction
9. Saving the spectra in RSS format

##### 4.2.5.1 Cosmic ray removal

Cosmic rays hits are removed directly from raw science images using PYCOSMIC<sup>3</sup>. PyCosmic combines the iterative Laplacian edge detection scheme (van Dokkum 2001) with a PSF convolution approach (Rhoads 2000).

---

<sup>3</sup>PyCosmic is a Python-based stand-alone program available at <http://pycosmic.sf.net>. For detailed description of the PyCosmic cosmic-ray rejection algorithm and a comparison to the commonly used L.A.Cosmic tool see Husemann et al. 2012.

	OB1-1	OB1-2	OB2-1	OB2-2	OB3-1	OB3-2
<b>iteration 1</b>	4564	4699	4437	4150	4830	4485
<b>iteration 2</b>	1567	1463	1420	1456	1190	1181
<b>iteration 3</b>	98	75	92	107	64	79
<b>iteration 4</b>	4	7	4	6	3	8

Table 4.4: Number of cosmic-ray affected pixels for the various NGC 3557 OBs exposures in the four iterations of PyCosmic (Q1 only).

	Q1	Q2	Q3	Q4
<b>iteration 1</b>	370	461	448	449
<b>iteration 2</b>	146	251	222	220
<b>iteration 3</b>	12	24	17	40
<b>iteration 4</b>	0	1	2	9

Table 4.5: Number of cosmic-ray affected pixels in the four quadrants of the spectro-photometric standard star Feige110 observation in the four iterations of PyCosmic.

A master bias image is subtracted from the data before applying PyCosmic. When a cosmic ray is detected the routine checks if the surrounding pixels are affected by cosmic ray hits as well. Once the pixel positions affected by cosmic rays are marked the raw science image is cleaned using a two-dimensional median filter which has a width of 5 pixel on both axes. Fig 4.2.7 shows the cosmic rays identified in a row image. PyCosmic is able to correctly identify cosmic rays also in the case of complex shapes.

PyCosmic is iterated four times. In general four iterations are enough for the process to converge.

Typical values of the number of cosmic ray affected pixels in each iteration of PyCosmic are reported in Table 4.4 and Table 4.5 (NGC 3557 and spectro-photometric standard star respectively). In the latter case the values are clearly smaller due to the significantly shorter exposure time.

At the end of the process the cosmic ray cleaned version of the input image is saved.

#### 4.2.5.2 Recentering the cross-dispersion line profiles

A crucial step for an accurate extraction of the science spectra is the estimate of possible offsets (in both X and Y directions on the CCD) between the trace-mask and the real spectra. The trace-mask is calculated using flat field exposures. Different instrumental flexures may affect the flat field and the science exposures, introducing offsets in the spectra arrangement on the CCD. Here the cross-dispersion recentering issue is discussed, for the realignment along the dispersion axis see Section 4.2.5.4.

With densely packed spectra obtained in IFU observing mode even a little offset can affect the results significantly (see e.g. Sandin et al. 2012).

Unlike the flat field image science images do not have a well-sampled continuum. In order to perform a reliable comparison between the trace-mask and the science spectra positions on the CCD, a higher signal-to-noise in the raw science spectra is needed. A median-filter (20 pixel-wide) is thus applied along the dispersion axis and spectra are replaced with median-filtered ones. For the spectro-photometric standard star the spectra

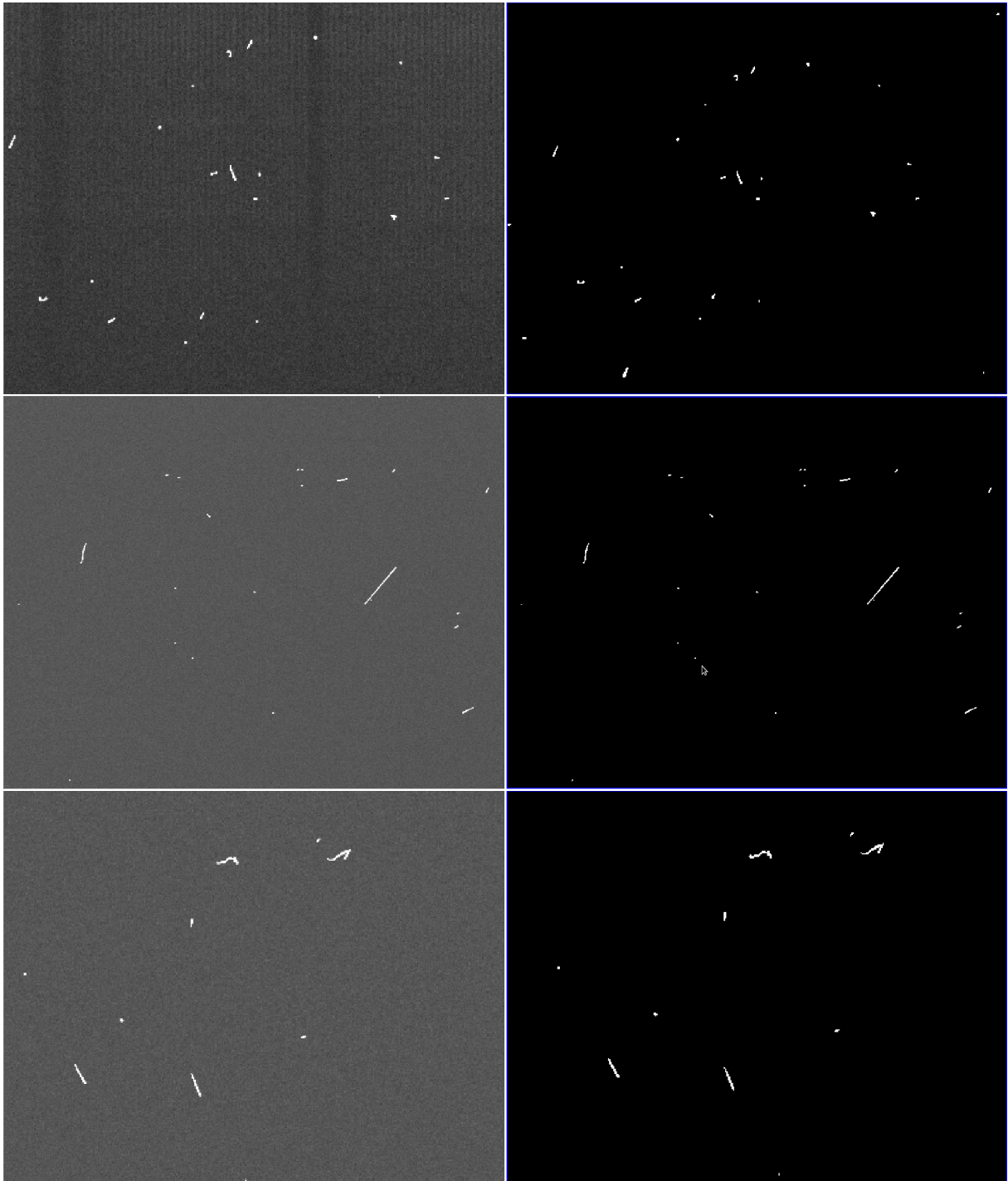


Figure 4.2.7: Raw science exposure (*left panel*) and related cosmic ray mask created by PyCosmic (*right panel*) in three different regions of the CCD. Cosmic ray hits can show complex shapes.

are bright enough and the median-filtering process is not necessary. A fit of the spectra profile along the cross-dispersion direction is performed for three different cuts in the dispersion direction (at the edges and in the central region). Comparing the fitted and the trace-mask profiles for the three cuts, an offset value is calculated for all the spectra as a function of wavelength. Then the estimated correction is applied. The offsets are typically below 1.5 pixels, except for the second quadrant (Q2), where offsets as large as 3 pixels are found. Figure 4.2.8 shows the results of the recentering process for Q2.

#### 4.2.5.3 Scattered light subtraction and extraction of the spectra

Raw data can show the presence of a scattered light component. To improve the quality of the spectra the scattered light component has to be estimated and subtracted. Empty regions of the CCD (no spectra present) are used for estimating the scattered light contribution. First the spectra are masked (all pixels within 6 pixels from each spectrum), then the unmasked regions are smoothed and a zero degree polynomial fit is calculated on the cross-dispersion axis. The polynomial order is kept low due to the lack of large spectrum-free regions on the CCD. In the final step the resulting image is smoothed with a Gaussian filter, and the scattered light image is created and subtracted from the input image. A scattered light image is shown in Fig 4.2.9. The values of the estimated scattered light are typically low, ranging from 2 to 8 ADU.

Spectra are extracted using a MPD extraction method in order to minimise crosstalk between adjacent fibres (see Sharp & Birchall 2010 for details). It should be noted that this process influences especially the trace-mask creation (see Section 4.2.2 for details). An accurate inspection is performed on the cross-dispersion fits in order to check the accuracy of the extraction process.

#### 4.2.5.4 Realignment along the dispersion axis and wavelength calibration

Different instrument flexures might affect the science spectra on the dispersion axis as well (see Section 4.2.5.2) with respect to the calibration arc lamp image. The wavelength calibration is fine tuned using the known wavelength of the telluric emission lines in the science data. This realignment is only performed for NGC 3557 exposures, as the spectrophotometric standard star exposure is not long enough, and the sky lines are not bright enough. Reference sky spectra are available at:

[http://www.eso.org/observing/dfo/quality/UVES/pipeline/sky\\_spectrum.html](http://www.eso.org/observing/dfo/quality/UVES/pipeline/sky_spectrum.html)

Sky lines from 5050 to 5290 Å are shown in Figure 4.2.10.

Visual inspection allowed to recognise two telluric lines (one at  $\sim 5198$  Å and the other at  $\sim 5200$  Å) in the spectral range covered by NGC 3557 spectra. All the other lines are too faint to be detected. These two sky lines are the brightest in the spectrum shown in Fig 4.2.10. The central wavelength, width, peak and integrated flux are listed in Table 4.6.

It is worth noticing that these two lines are blended at the resolution (2.7 Å) of our NGC 3557 observation. We therefore assume for the blended line a central wavelength of 5199 Å, while the flux is obtained by summing the two components. Before data are wavelength calibrated, the input sky line is fitted with a Gaussian in each spectrum of

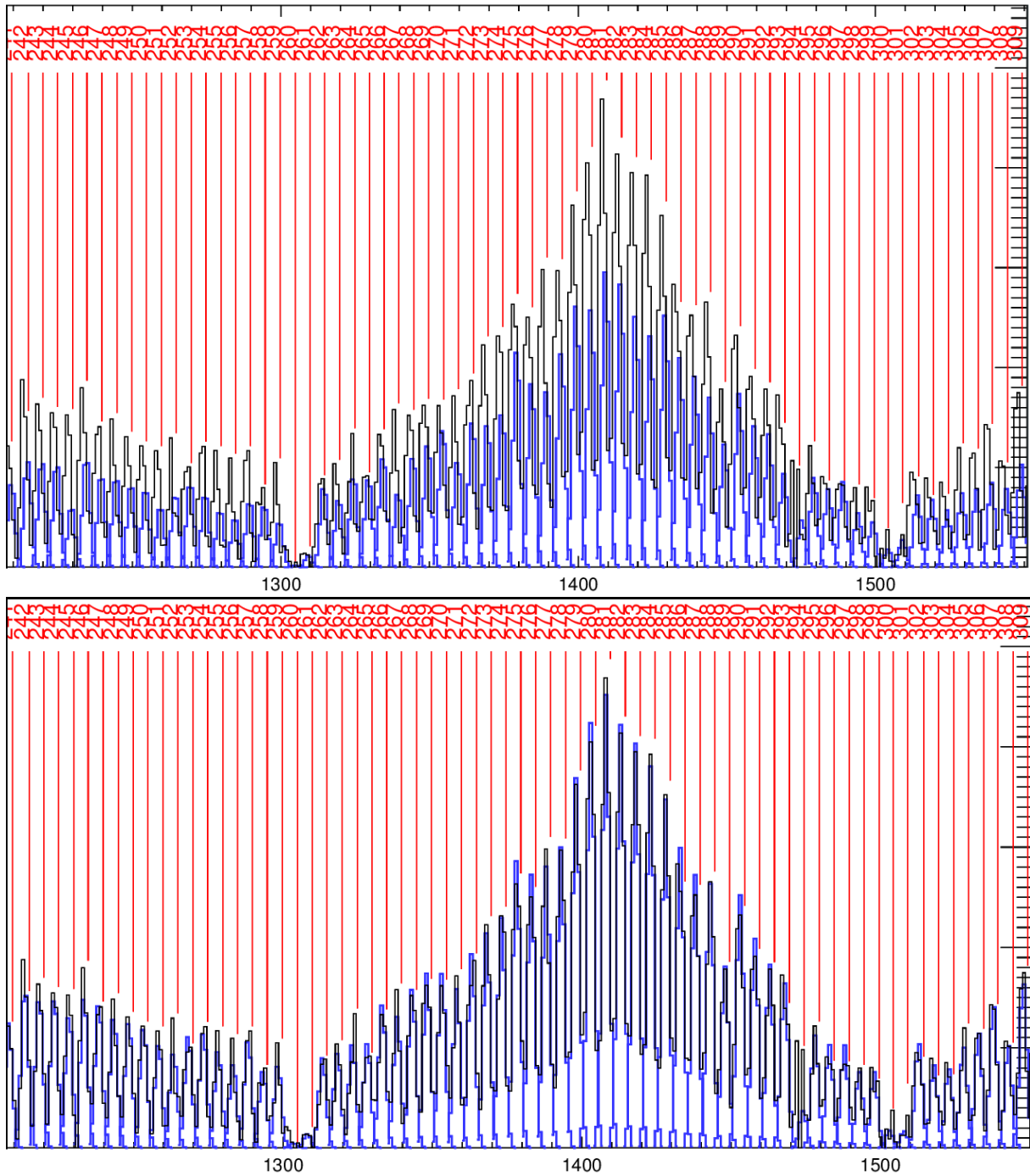


Figure 4.2.8: A sub-set of spectra cut along the cross-dispersion direction. The intensity of the spectra profile is plotted against the pixel number along the cross-dispersion axis of the CCD (black line). The cross-dispersion profile fit (blue line) is shown together with its fitted centre (red vertical line). The *upper* and *lower panels* respectively show the fitting result before and after applying the proper offset correction.



Figure 4.2.9: Example of scattered light image.

<b>centre [<math>\text{\AA}</math>]</b>	<b>FWHM [<math>\text{\AA}</math>]</b>	<b>Peak Flux</b> [ $10^{-16}\text{ergs}^{-1} \text{\AA}^{-1} \text{cm}^{-2}\text{arcs}^{-2}$ ]	<b>Integrated Flux</b> [ $10^{-16}\text{ergs}^{-1}\text{cm}^{-2}\text{arcs}^{-2}$ ]
5197.928223	0.12188	4.75124	0.617
5200.285645	0.12109	2.75663	0.358

Table 4.6: Central wavelength, width, peak and integrated flux for the two telluric lines used for the realignment along the dispersion axis. The integrated flux has been obtained by assuming a Gaussian shape for the line.

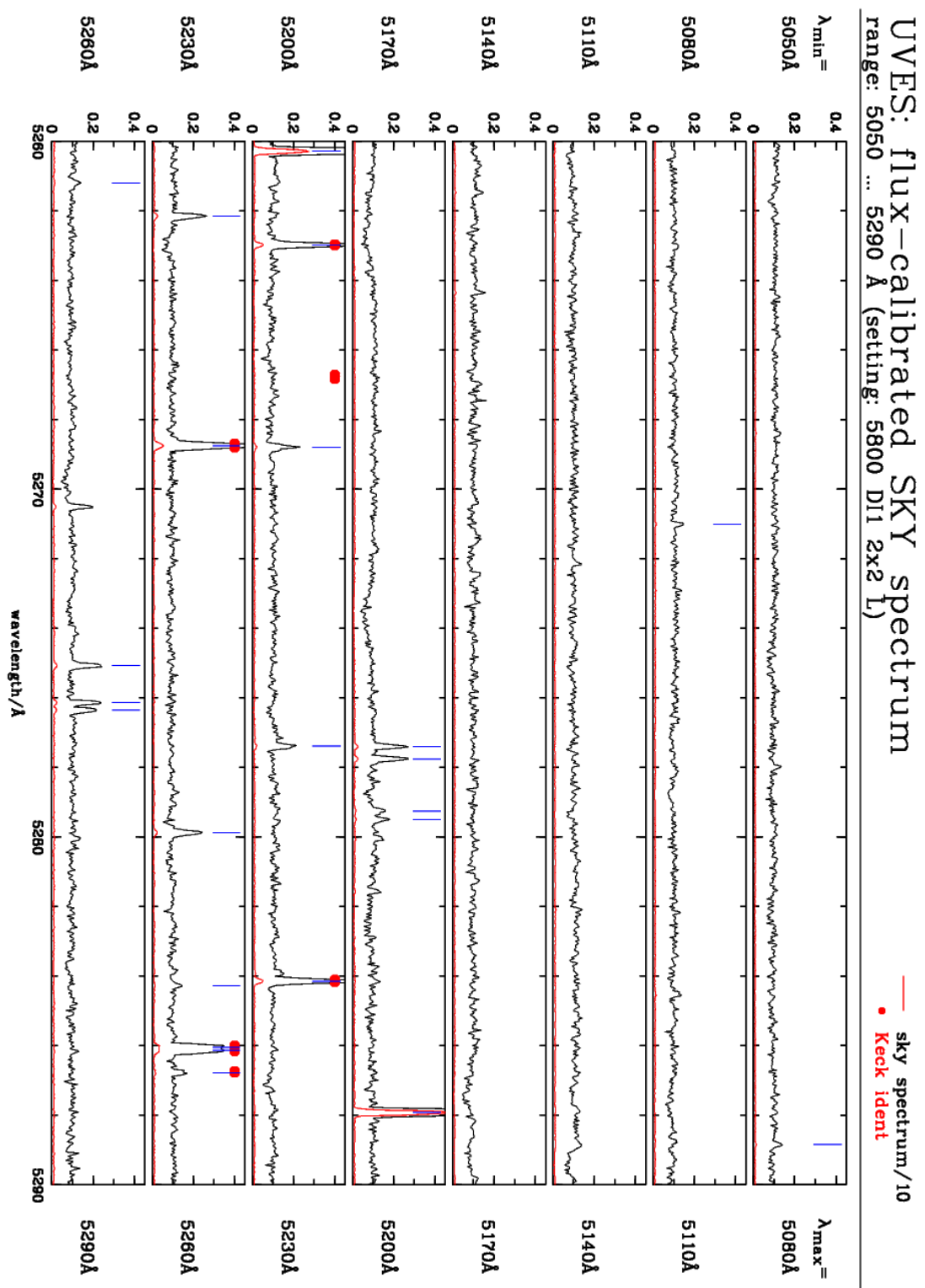


Figure 4.2.10: Sky spectrum taken with the high-resolution VLT-UVES spectrograph (UT2). Flux in units of  $[10^{-16}\text{erg/s \AA cm}^2\text{arcs}^2]$  vs wavelength. The eight panels show different wavelength ranges (30 Å wide) from 5050 Å to 5290 Å. The vertical blue bars mark measured lines while red dots indicate lines identified at Keck telescope.

the science exposures, as a single Gaussian proved to provide accurate enough fits of this blended line.

As a first guess for the fitting we used the pixel position corresponding to the input wavelength (5199 Å) in the dispersion-mask. Comparing this value with the wavelength assigned to the same pixel by the fitting process, an offset is first calculated and then applied to each spectrum. In the majority of the cases the offset is  $\lesssim 0.5$  pixel. In those cases where the fitting does fail, no offset is applied to the spectrum.

The wavelength calibration of the science and standard star spectra is performed using the realigned dispersion mask. In order to get the same for all the four quadrants, all the spectra are resampled. The final dispersion is 0.71 Å/px.

#### 4.2.5.5 Correction for transmission and flat-field

The last step of the spectra extraction process consist in the application of the corrections for the variations in sensitivity over the CCD (flat-fielding correction) and for the fiber light transmission efficiency (transmission correction). After both corrections are applied, the spectra are saved in RSS format.

#### 4.2.6 Sensitivity function and Flux Calibration

The intensity of the extracted spectra is provided in counts, using the analog-to-digital unit (ADU). In order to perform a conversion from ADU to physical units the spectro-photometric standard star Feige110 exposure is used. The first step is the creation of a sensitivity function that determines a correspondence between ADU and physical units at each wavelength. Feige110 spectra are first extracted using the previously described procedure. Extracted spectra are then displayed with the help of the *Spectrum Viewer* tool (a snapshot is shown in Fig 4.2.11). In the right upper panel of the Spectrum Viewer the FoV of the image is reconstructed using default position tables, that allows to handle and combine the star spectra distributed over several pixels (see left upper panel).

A sky spectrum is created by averaging those spectra not contaminated by the star light. They can be selected using the so-called *average* function from the outer pixels in the FoV image (see upper right panel). The sky spectrum obtained in this way is then subtracted from all the spectra in the image using the *subtr* function of the *Spectrum Viewer*. At this point a sky subtracted spectrum of Feige110 can be obtained by selecting all the pixels affected by the star light in the FoV image (see upper right panel) and summing such spectra in order to entirely recover the light from the standard star.

The spectro-photometric standard star spectrum and the mean sky spectrum obtained with this procedure for each quadrant are shown in Fig 4.2.12 and Fig 4.2.13 respectively.

We notice that dead or low transmission fibers are excluded in this process.

Fig 4.2.12 clearly shows an anomalous flux decrease in Q3 between 4550 and 4650 Å. An accurate investigation was carried out to understand if this feature is present also in NGC 3557 raw spectra. This check shows that only a limited number of spectra lying in a small region of Q3 are affected by a similar problem. It should be noted that the pixels/spectra showing the afore-mentioned feature are not the same for NGC 3557 and Feige110 when their sky positions are compared. Q3 thus appears affected by local variations of the sensitivity, and a single sensitivity function applied to the whole

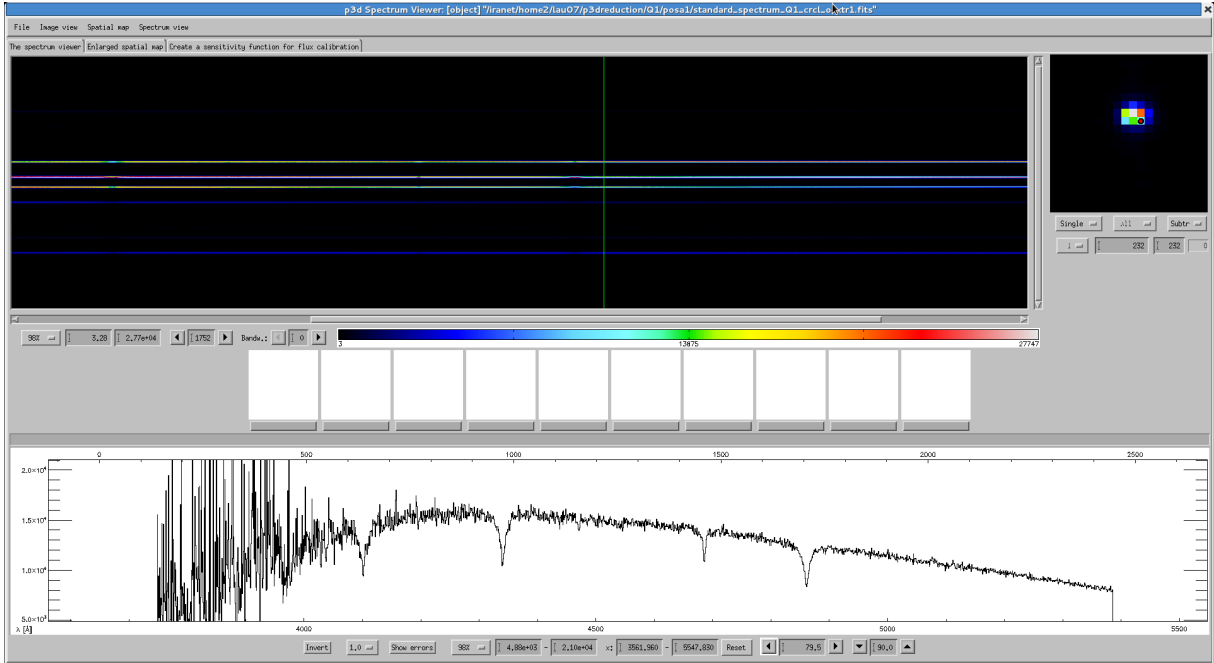


Figure 4.2.11: Two main panels are present: the RSS format image of the extracted spectra is shown in the left upper panel while the spectrum of a selected pixel is displayed in the lower panel. Feige110 extracted spectra are shown using the Spectrum Viewer. The upper-right panel shows the standard star image FoV at a selected wavelength.

quadrant cannot account for this problem. We are still trying to understand the origin of this problem, which however affects a limited number of spectra. This issue will be further described in Chapter 5.

During the selection of the spectra/pixel employed to obtain both the standard star spectrum and the sky spectrum all the spectra related to dead or low transmission fibers are excluded.

The sky subtracted standard star spectrum together with a calibration spectrum of the same star and an extinction function are used for the creation of a sensitivity function. A calibrated reference spectrum of Feige110 can be downloaded from the ESO webpage at:

<http://www.eso.org/sci/observing/tools/standards/spectra/feige110.html>

The reference spectrum is binned in 7 Å steps between 3200 and 4700 Å and in 13 Å steps between 4702 and 9200 Å. The flux unit is  $\text{ergs}/\text{cm}^2/\text{s}/\text{Å} * 10^{-16}$ .

The atmospheric extinction (tabulated in [mag/airmass]) as a function of wavelength [Å] is provided together with the reference spectrum. The exposure time and the mean airmass of the standard star are given in the spectrum file header.

A common wavelength range is determined for the calibrated and the observed spectrum. The extinction curve is interpolated with a rational spline in order to use the same wavelength grid for the calibration and the observed spectrum. The observed flux in each bandpass is calculated and, accounting for an extrapolated extinction value, a correction factor  $f_j$  is calculated for each pixel  $j$  in the bandpass  $i$ .

It should be noted that, with a spectral sampling of 0.71 Å/pixel, a 7 Å band pass

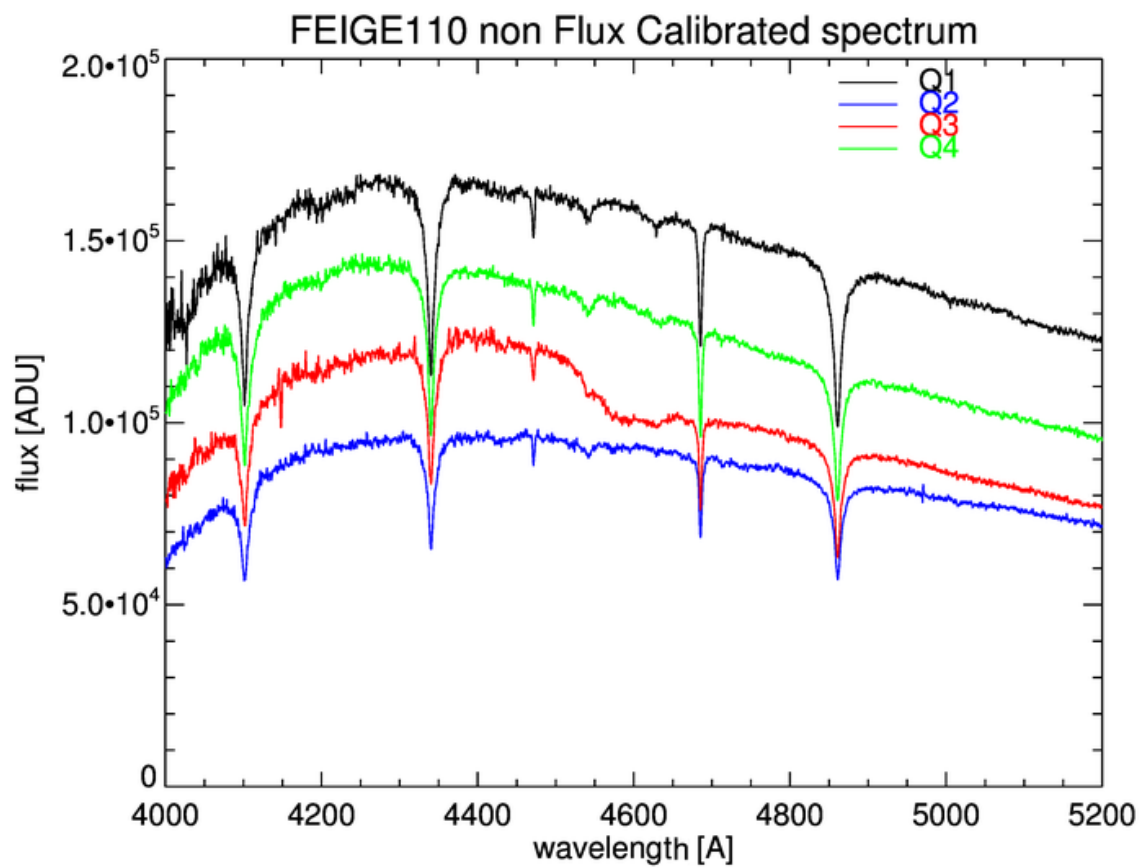


Figure 4.2.12: Feige110 non flux calibrated spectrum for each of the four quadrants. Quadrant are indicated in the upper-right side of the plot. The spectrum obtained for Q3 shows an anomalous feature in the 4550-4650 Å range.

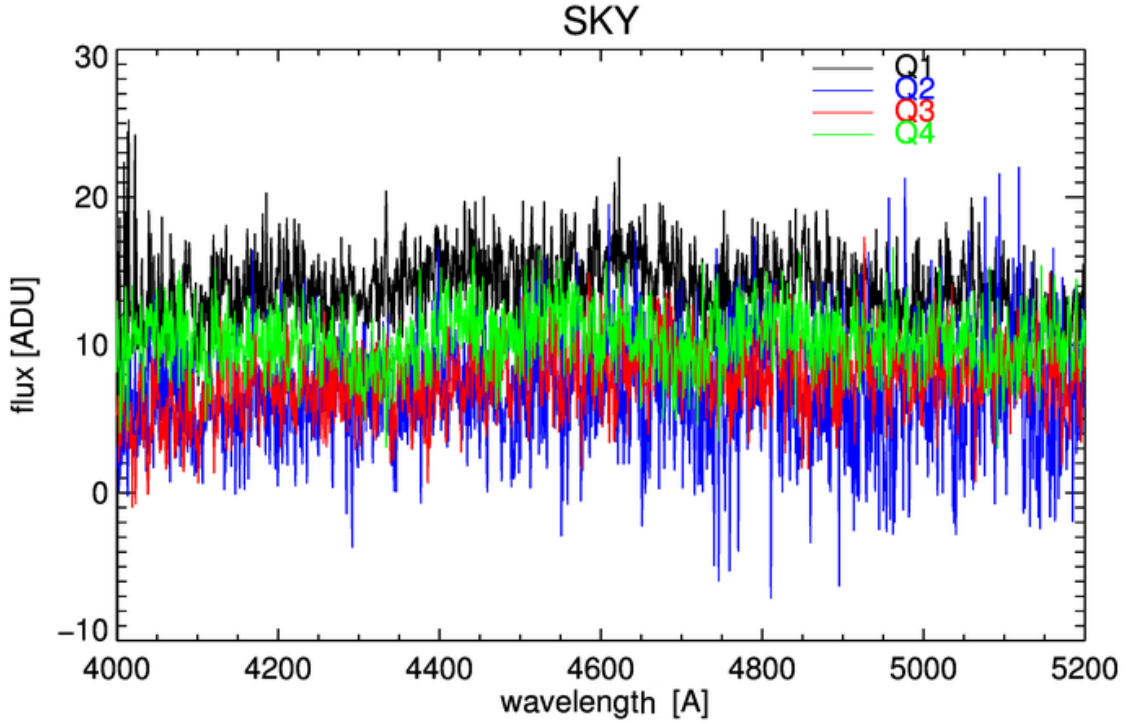


Figure 4.2.13: Mean sky non flux calibrated spectrum subtracted from the Feuge110 image. Quadrant are indicated in the upper-right side of the plot.

includes about ten pixels while for 13 Å bandpass it includes about 18 pixels.

Observed data are then multiplied by the  $f_j$  factors and a summed flux in each bandpass is estimated accounting for fractional pixels. At this point a calibration factor  $c_i$  is calculated for each bandpass  $i$ . The relevant formulas applied in this process are:

$$f_j = 10^{0.4 * \text{airmass} * (\text{ext}_j - \text{ext}_i)} \quad (4.2.2)$$

where  $\text{ext}$  is the extinction in mag/airmass;

$$c_i = 2.5 * \log_{10} \left( \frac{\text{flux\_corr}_i}{\text{exptime} * \text{flux\_cal}_i * b\_width_i} \right) + \text{exptime} * \text{ext}_i \quad (4.2.3)$$

where  $\text{flux\_corr}$  [ADU] is the observed summed flux in a band pass;  $\text{flux\_cal}$  [ergs/cm<sup>2</sup>/s/Å \* 10<sup>-16</sup>] is the band pass flux extracted by the calibrated spectrum,  $\text{exptime}$  [s] is the exposure time and  $b\_width$  [Å] is the band pass width.

The correction-factor array is interpolated over the observed wavelength range, to create a sensitivity function in mag units. The interpolation is obtained using a 8 degree polynomial fit (Q3 is the only exception, a 7 degree polynomial is used). This process can be fine tuned through the GUI. Figure 4.2.14 gives an example of the calibration plots.

The flux calibrated spectrum of the observed star can be interactively inspected in order to check for the accuracy of the sensitivity function. Some points can be excluded

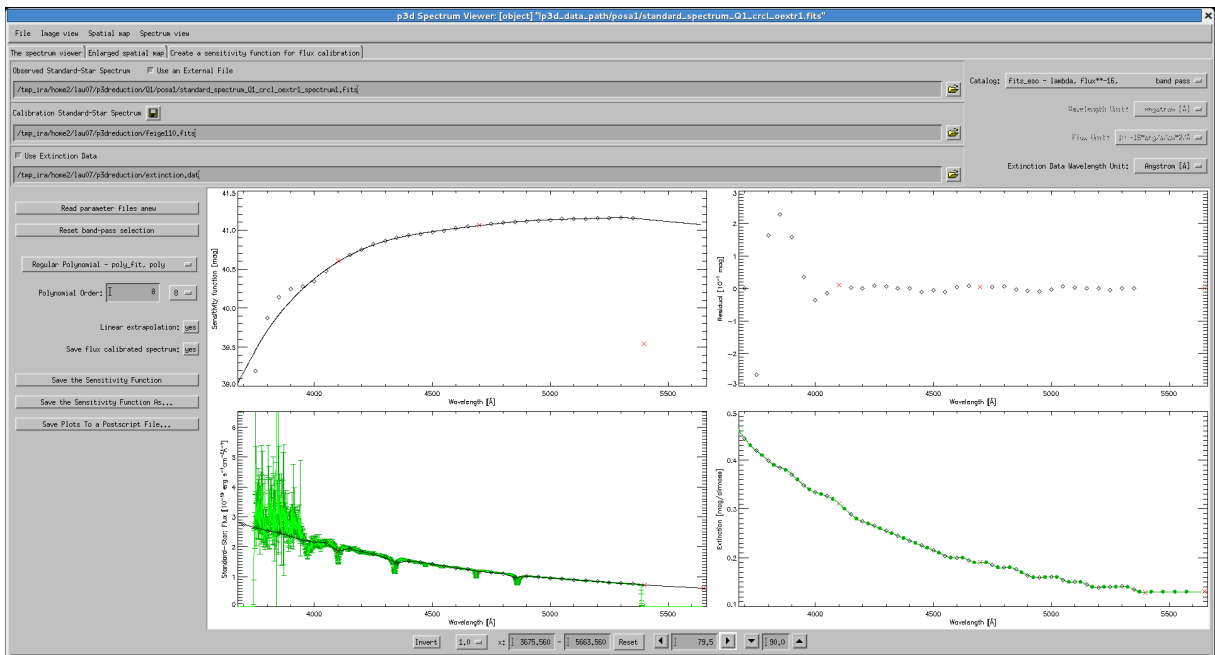


Figure 4.2.14: Example of calibration plots from the *Spectrum Viewer*. *Top-left panel*: sensitivity function in mag units. *Top-right panel*: sensitivity function residuals in units of  $10^{-2}$ mag. They represent the difference between the calculated correction factors (diamonds in the upper left panel) and the interpolated ones. *Bottom-left panel*: observed (green) and flux calibrated (black) spectrum of Feige110, [ $10^{-13}$ ergs/cm<sup>2</sup>/s/Å ] unit. *Bottom-right panel*: fitted extinction function in [mag/airmass] (green line); green filled points indicate the tabulated values while diamonds indicate the extrapolated ones.

Quadrant	Mean RMS [ $10^{-2}$ mag]
Q1	7.45
Q2	1.34
Q3	9.01
Q4	2.00

Table 4.7: Mean RMS of the sensitivity function residuals in the four quadrants.

from the fit in order to create a smoother sensitivity function over the entire wavelength range. In particular we forced the sensitivity function not to follow the anomalous drop in Q3 (see discussion above).

In addition we flagged some points which are close to the absorption lines as they can produce artificially high correction factors. This is mainly due to the fact that absorption lines in our observed spectrum are stronger than in the reference one, due to the higher resolution of the former. Figures 4.2.15, 4.2.16, 4.2.17, 4.2.18 show the final sensitivity function obtained for each quadrant.

The residuals in the fitting of the sensitivity function are never larger than a few tenths of magnitude. The largest spread is found at bluest wavelengths, where the spectra are very noisy. Table 4.7 reports the mean RMS of the residuals, which is of the order of few hundreds of a magnitude. The largest value ( $7.45 \times 10^{-2}$ mag) is found for Q1.

The sensitivity function is used to flux calibrate the NGC 3557 extracted spectra. The flux calibration is performed by multiplying the observed spectra by the following factor, calculated for each pixel  $j$ :

$$\tilde{f}_j = \frac{10^{0.4*airmass*ext_j}}{exptime * delt * 10^{0.4*sens_j}} \quad (4.2.4)$$

where  $delt$  [ $\text{\AA}$ ] is the observed spectrum sampling factor ( $0.71 \text{ \AA}/\text{px}$ ) and  $sens$  [mag] is the sensitivity function value.

The unit of the flux calibrated spectra is [ $\text{ergs}/\text{cm}^2/\text{s}/\text{\AA}$ ].

Fig 4.2.19 shows the flux calibrated spectra of Feige110 for the four quadrants. As can be noted the third quadrant Q3 is found to be more affected by local sensitivity variations, while for the other quadrants we found a very good match with the standard star spectrum.

It should be noted that the Feige110 spectrum used to create the sensitivity function for each quadrant is extracted using only the central pixels of a quadrant i.e. only the fibers sampling the star light (the star is a point source). Monreal-Ibero et al. (2006) report that a pointing of spectro-photometric standard star in different regions of the quadrant yield spectra with different continuum levels. In other words the sensitivity is not uniform across the detector. This means that the created sensitivity function can depend on where the star is located by respect to the centre of the CCD, and a single sensitivity function cannot account for sensitivity variations over the entire CCD. In addition response curves and efficiency measurements made by the ESO staff in IFU mode, show significant variations in time <sup>4</sup>, and this can again affect the flux calibration

<sup>4</sup>See <http://www.eso.org/observing/dfo/quality/VIMOS/qc/response.html> and [http://www.eso.org/observing/dfo/quality/VIMOS/qc/specphot\\_var.html](http://www.eso.org/observing/dfo/quality/VIMOS/qc/specphot_var.html)

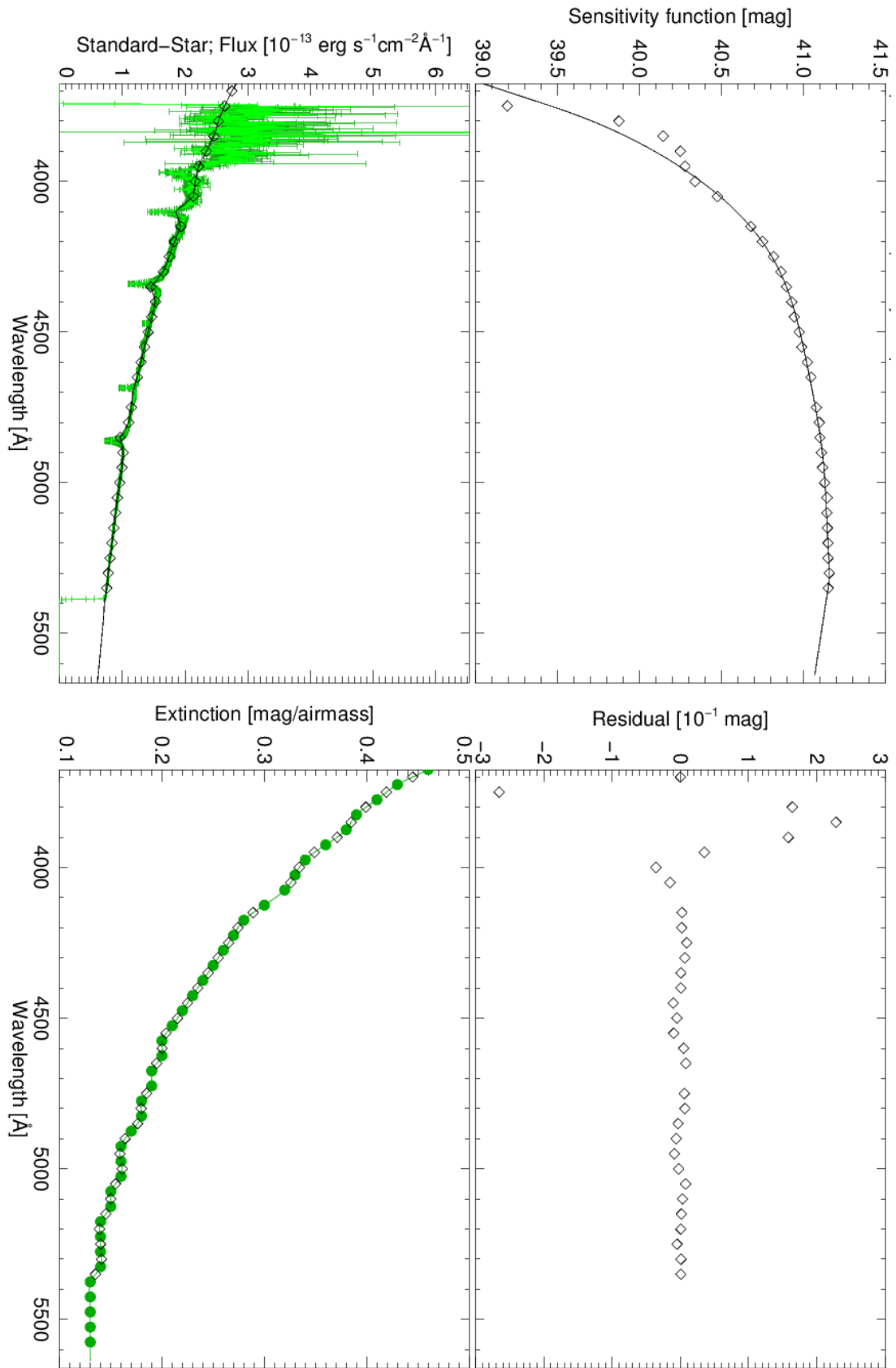


Figure 4.2.15: Final calibration plots for Q1. Panels as in Figure 4.2.14.

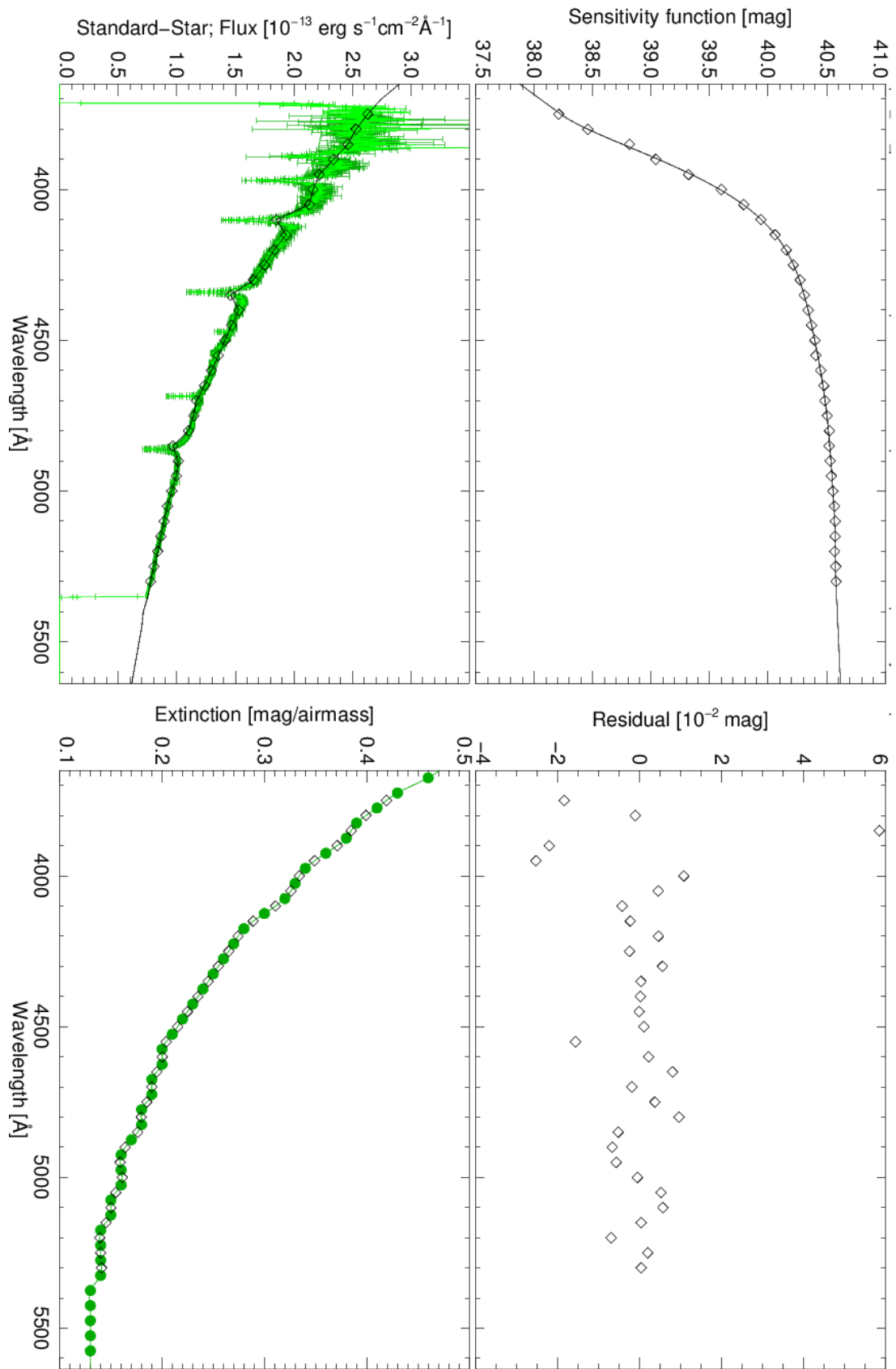


Figure 4.2.16: Final calibration plots for Q2. Panels as in Figure 4.2.14. The residuals are in [ $10^{-2}$  mag] units.

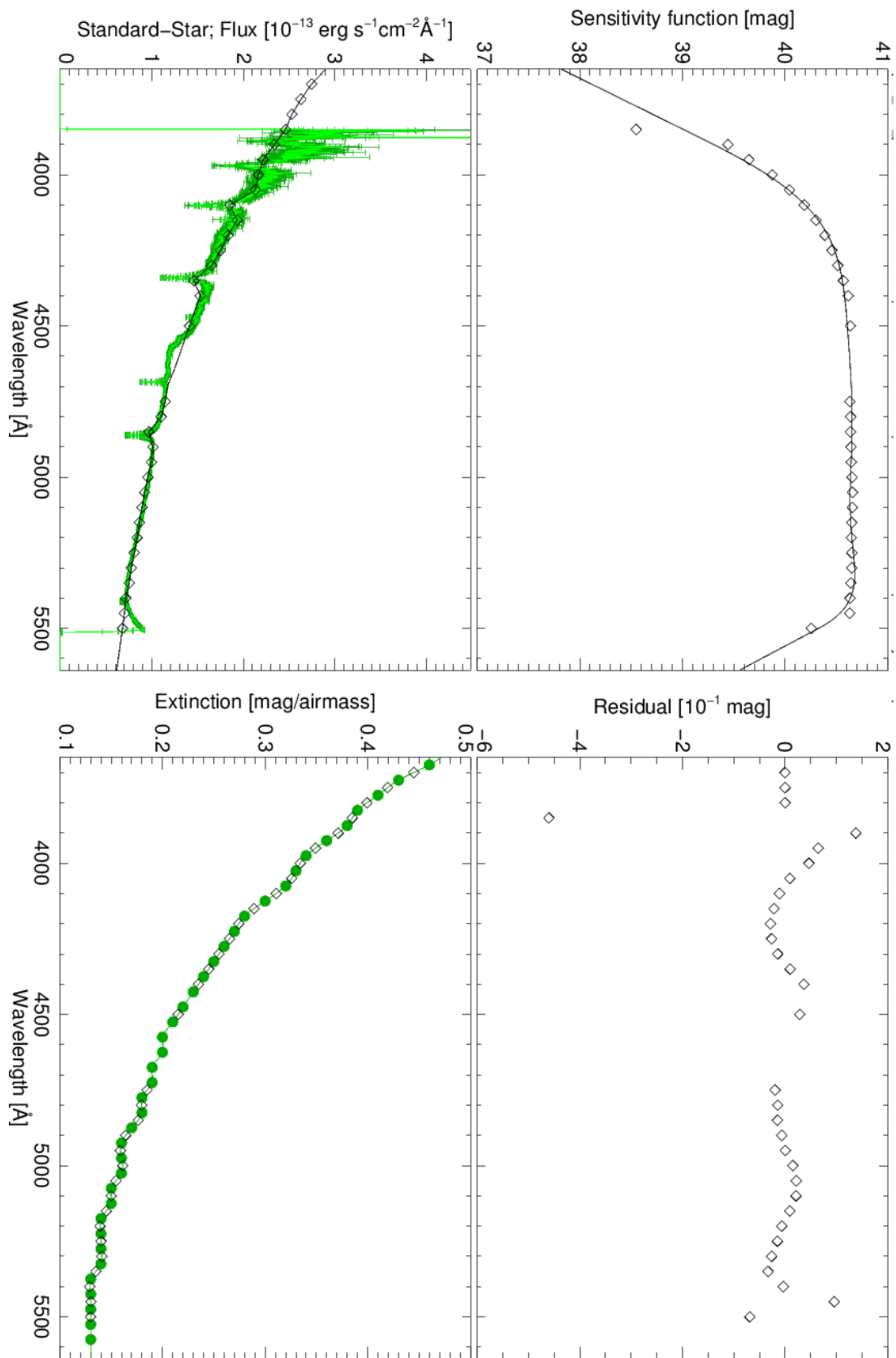


Figure 4.2.17: Final calibration plots for Q3. Panels as in Figure 4.2.14.

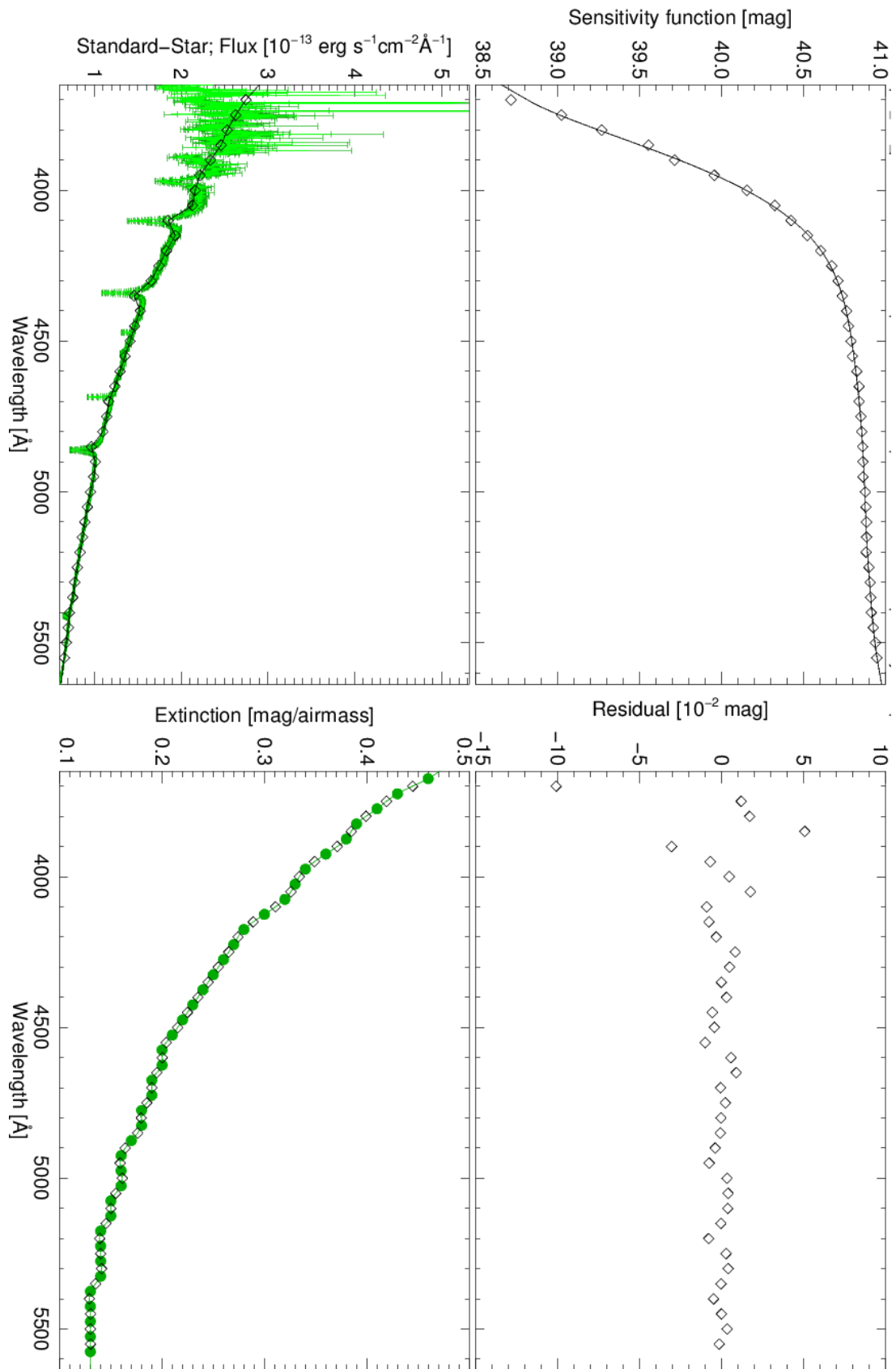


Figure 4.2.18: Final calibration plots for Q4. Panels as in Figure 4.2.14.

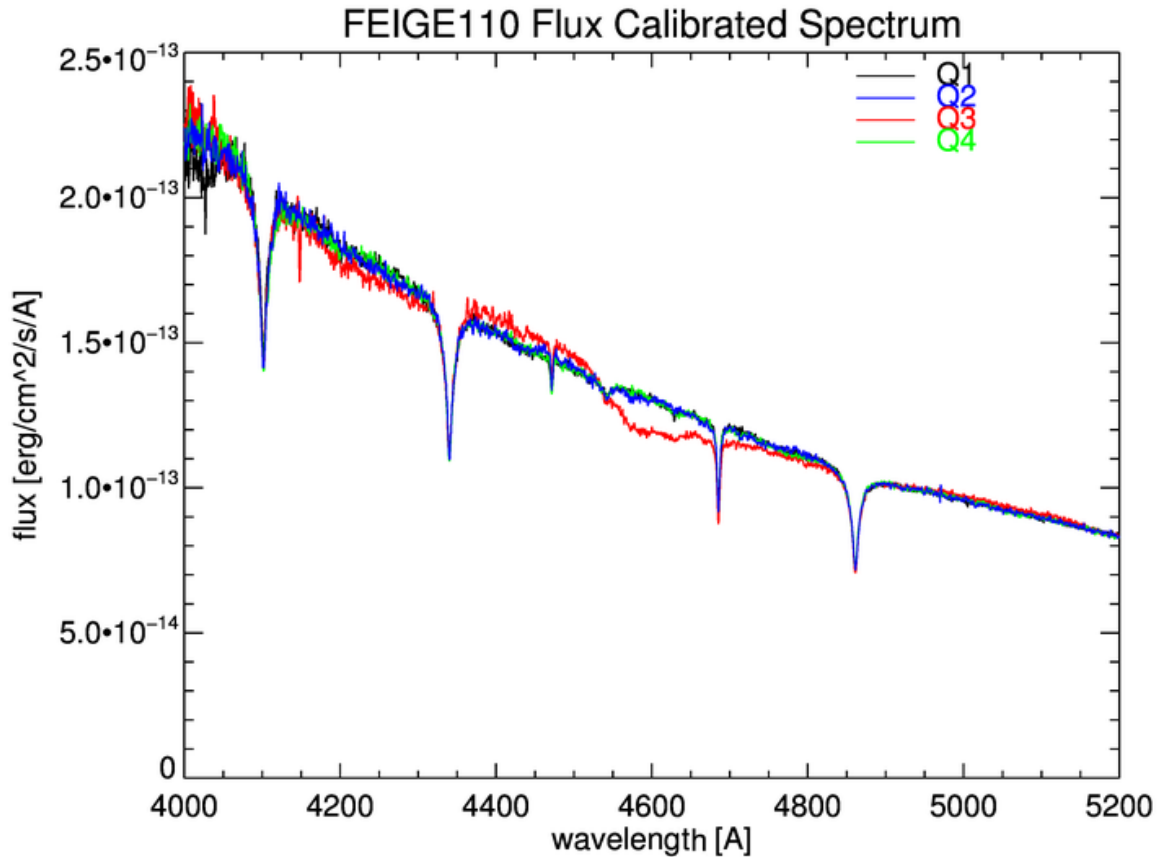


Figure 4.2.19: Feige110 flux calibrated spectrum for each quadrant. The quadrant is indicated in the upper-right side of the plot.

when the standard stars and the science frames are not obtained in the same night. This may at least partially explain the presence of offsets in the mean flux among the four quadrants in the final combined image (see Section 4.2.7), and potentially also the less precise flux calibration obtained for Q3.

#### 4.2.7 Image combination and final image cosmesis

Once the science extracted spectra are wavelength calibrated, flux calibrated and saved in RSS format, the images of the four quadrants can be combined together in order to reconstruct the entire FoV image of our target.

To correct for the systematic flux offsets among quadrants (seen Section 4.2.6) a renormalization is performed, using as reference the flux of the blended sky line at 5199 Å. A median flux of the selected sky line is estimated for each quadrant from all the spectra (see Table 4.8 for the typical line flux values) and a correction factor is determined by imposing for all the quadrants an integrated line flux equal to  $1 \times 10^{-16}$  ergs/cm<sup>2</sup>/s. This value is estimated by summing the flux of the two 5198 Å and 5200 Å sky lines (see Table 4.6) under the assumption of a typical seeing of 1 arcsec (see Table 3.8).

Once renormalized, the combined image is corrected for the effect of the Differential Atmospheric Refraction (DAR). Due to DAR the observed object appears at slightly

Quadrant	Median flux [ergs/cm <sup>2</sup> /s/Å]
Q1	4.362e-17
Q2	5.826e-17
Q3	8.292e-17,
Q4	6.926e-17

Table 4.8: Typical mean fluxes for the blended sky line at 5199 Å in the four quadrants.

OB	Exposure	min offset at 3650 Å [arcsec]	max offset at 5637 Å [arcsec]
1	1	-0.19	0.09
1	2	-0.17	0.08
2	1	-0.22	0.11
2	2	-0.26	0.13
3	1	-0.16	0.08
3	2	-0.18	0.09

Table 4.9: Amplitude of DAR induced offsets estimated with Ciddor (1996) equation.

different positions at different wavelengths, unless the observation is carried out at zenith. The data are converted from RSS to cube format, they are corrected, and then converted back to RSS format. The DAR routine (see Figure 4.2.20) first estimates the amplitude of the DAR induced positional shift as a function of wavelength (i.e. the DAR vector amplitude) and then corrects the image at each wavelength by this value. The direction of the DAR vector is the parallactic angle.

The approach of Ciddor (1996) is followed to calculate the wavelength-dependent refractive index employed for the final correction.

As shown in Table 4.9 the positional offsets introduced by the DAR are negligible on the wavelength range covered by the data; considering a spatial resolution  $0.67'' \times 0.67''/\text{pixel}$ , the shift is always of the order of a fraction of pixel.

As a final step all the exposures of NGC 3557 can be combined in order to improve the signal-to-noise ratio. It should be noted that science exposures do not have to be corrected for seeing variation before being combined. Seeing variations between the start and the end of a single exposure are indeed comparable to seeing variations between different exposures (see Table 3.8 for reference). The exposures are weighted by their exposure time, summed up and then divided by the number of exposures. The final averaged image is converted into a datacube  $(x, y, \lambda)$  using the default IFU fiber position tables.

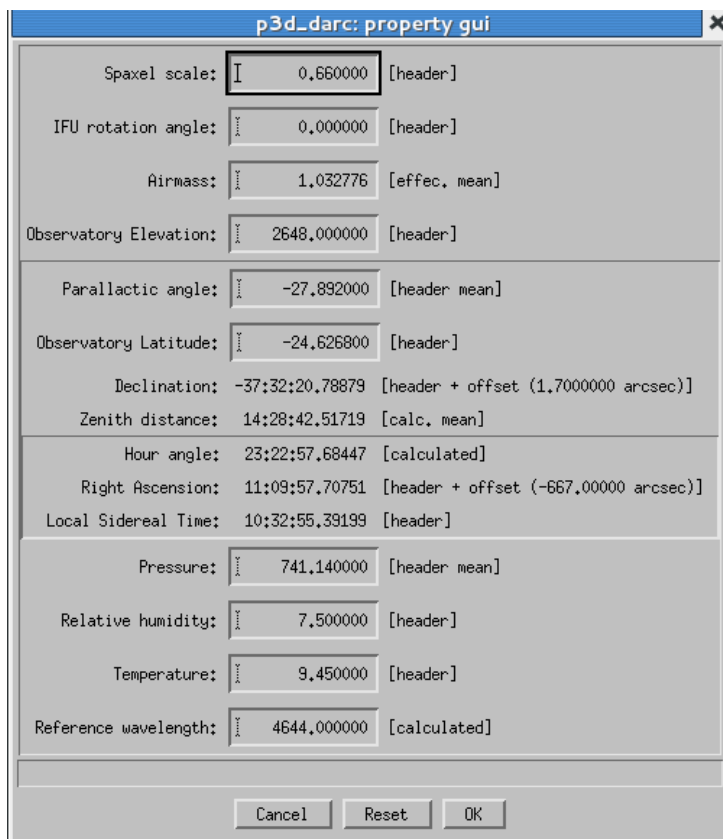


Figure 4.2.20: The DAR correction routine graphical window. Here is possible to check and possibly modify the input parameters for the DAR correction estimate.

# Chapter 5

## NGC 3557: Stellar kinematics analysis

As discussed in Chapter 4, the spectral resolution of our dataset is  $2.7 \text{ \AA}$  FWHM ( $\sigma_{instr} = 78 \text{ km s}^{-1}$ ) at the reference wavelength of  $4400 \text{ \AA}$ , while the spectrum sampling is  $0.71 \text{ \AA}$  /pixel ( $48 \text{ km s}^{-1}$ ). The wavelength calibration reaches an accuracy of  $0.35 \text{ \AA}$  ( $23 \text{ km s}^{-1}$ ).

The VIMOS/IFU FoV covers only the central part of NGC 3557 ( $27'' \times 27''$ ) with a spatial resolution of  $0.67'' \times 0.67''$  per pixel. This corresponds to  $\sim 0.4 R_e$ , being the effective radius of the galaxy is  $40''$ . As will be discussed later, this issue has a significant role in the scientific interpretation of the NGC 3557 kinematics. In addition, ATLAS<sup>3D</sup> galaxies, are in most cases, sampled up to  $1R_e$  and a comparison with ATLAS<sup>3D</sup> results must necessarily take into account the smaller galaxy scale we actually observe.

### 5.1 Extraction of the velocity and velocity dispersion maps

The four VIMOS/IFU quadrants cover slightly different spectral ranges. As a first step all the spectra were therefore cut in order to obtain a final common wavelength range for all the quadrants (i.e.  $4000\text{-}5300 \text{ \AA}$ ).

The stellar kinematics was extracted with the penalized pixel fitting (pPXF<sup>1</sup>) software (Cappellari & Emsellem 2004), which simultaneously fits the stellar kinematics and finds the optimal linear combination of spectral templates for the observed spectrum. The line-of-sight velocity distribution (LOSVD) is described via the Gauss-Hermite parametrization up to  $h_3$  and  $h_4$  moments. The pPXF algorithm uses a technique to fit the LOSVD, in which the solution is free to reproduce the details of the actual profile when the S/N is high, and where the solution tends to a Gaussian shape in case of low S/N. This is justified by the fact that the LOSVD of galaxies is generally well reproduced by a Gaussian. In other words, the velocity  $v$ , the velocity dispersion  $\sigma$ , and the  $h_3$  and  $h_4$  moments can be simultaneously fitted, or, alternatively, while the solution is biased towards a Gaussian shape when the higher moments are unconstrained by the data. This happens in low S/N spectra or when the LOSVD is not well sampled (i.e. less than two pixels sample the characteristic  $\sigma$  of the galaxy). It should be noted that pPXF works in pixel space.

The MILES library<sup>2</sup> (Sánchez-Blázquez et al. 2006) was employed in order to obtain

---

<sup>1</sup>pPXF is available from <http://www-astro.physics.ox.ac.uk/~mxc/idl/>

<sup>2</sup>Available from <http://miles.iac.es/pages/stellar-libraries/miles-library.php>

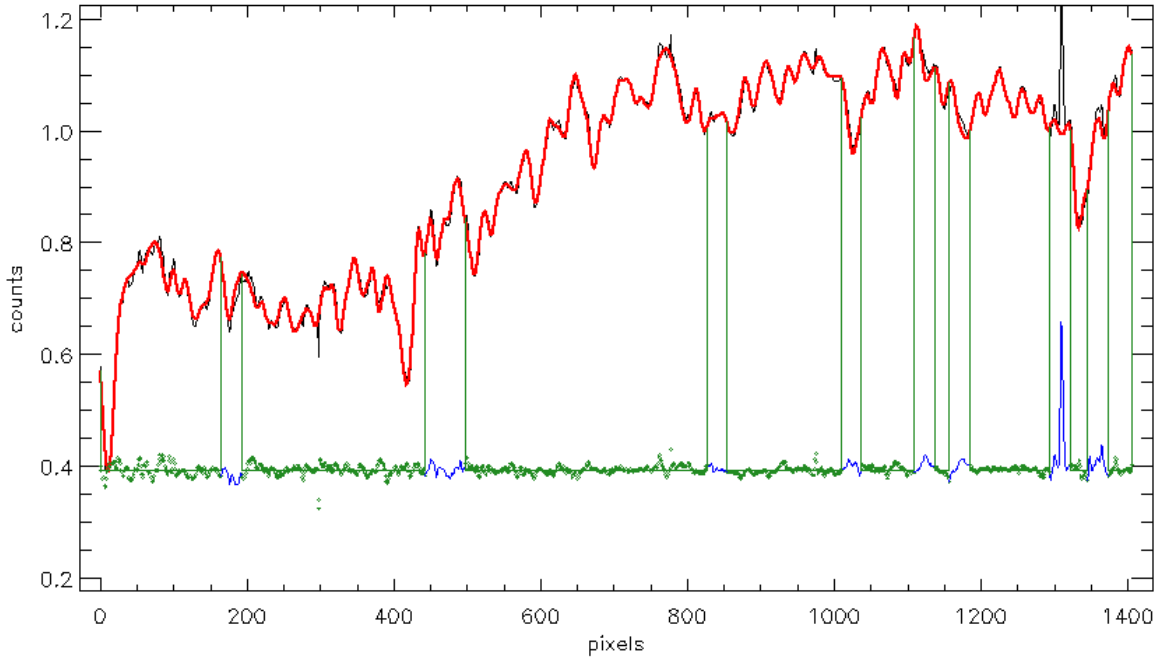


Figure 5.1.1: The integrated NGC 3557 spectrum: normalized flux versus pixel number. The black solid line and the red solid line indicate, respectively, the NGC 3557 spectrum and the fit. The green lines isolate the masked spectral region potentially affected by gas emission and/or sky lines. The residuals are plotted in the lower part of the plot using green dots; in masked regions the residuals are indicated with a thin blue line.

an optimal template to fit the spectra of NGC 3557. The library is constituted by  $\sim 1000$  stellar templates with a  $2.5 \text{ \AA}$  (FWHM) spectral resolution.

A first fit was performed on the integrated galaxy spectrum in order to check the goodness of the fit and, above all, to determine the optimal linear combination of the library templates to be used to fit each spectrum (i.e. the optimal template).

Figure 5.1.1 shows the fit of the total NGC 3557 spectrum; the masked regions are related to potential emission by ionized gas and to the sky emission line at  $\sim 5199 \text{ \AA}$ . The first-guess NGC 3557 velocity dispersion estimated by the fit ( $\sigma \gtrsim 200 \text{ km s}^{-1}$ ), shows that our data are not strongly affected by LOSVD undersampling. The pPXF simultaneous fitting procedure should therefore provide acceptable results.

The spectra corresponding to the central region of the galaxy, where the S/N ratio is higher, were more accurately inspected, in order to verify if ionized gas emission is present. During this check we noted that a significant fitting mismatch affects part of the spectra. Figure 5.1.2 shows two fitting examples: one providing a good match (*upper panel*) and one showing a mismatch (*lower panel*). An accurate investigation showed that the mismatch can be attributed to the already mentioned flux inconsistency that affects some spectra of the third quadrant Q3 (see Chapter 4, Section 4.2.6). In a limited region of the FoV an abrupt decrease of the spectrum continuum is reported around  $4500 \text{ \AA}$ . As already noted when discussing the flux calibration process, Q3 appears to be more affected by local sensitivity variations than the other quadrants. We tried to increase the degree

Emission line	Rest Wavelength [ $\text{\AA}$ ]
$H\delta$	4101.73
$H\gamma$	4340.46
[OIII]	4363.15
$HeII$	4685.74
$H\beta$	4861.32
[OIII]	4958.83
[OIII]	5006.77
[NI]	5197.90
[NI]	5200.39

Table 5.1: Candidate gas emission lines and corresponding rest wavelengths. Each line correspond to a masked region in Figure 5.1.3, some nearby emission line do fall in a single masked region.

of the polynomial fitting but the optimal stellar template continues to show a mismatch in correspondence of the abrupt decrease of the continuum. We identified the “faulty” spectra, and inspected them before and after the flux calibration process. The problem is clearly yet present in the raw spectra and seems to be related to a local variation of the detector sensitivity which we could not account for. The flux calibration alone could not solve this problem and we are currently checking if the flat-fielding correction or the spectral tracing can somehow be connected to this problem. Unfortunately the problematic spectra are in part covering the central region of NGC 3557, carrying with them a significant fraction of the flux and important kinematic information. We thus decided to perform the analysis in two separate wavelength range, one going from 4000 to 4500  $\text{\AA}$  and the other covering 4500-5300  $\text{\AA}$ , thus removing the problem introduced in the fitting by the continuum drop around 4500  $\text{\AA}$ .

The optimal linear combination of the templates was determined again and the fit was inspected for the two wavelength ranges separately. Figure 5.1.3 shows the fit of the total NGC 3557 spectrum for the 4500-5300  $\text{\AA}$  (*upper panel*) and 4000-4500  $\text{\AA}$  (*lower panel*) ranges.

The fits were again inspected in order to select regions of the spectra that have to be masked due to the presence of gas emission lines. Againg, the check was done on the central regions of the galaxy, where the S/N ratio is higher and the ionized gas emission is more likely to be detected (Sarzi et al. 2006). In the 4500-5300  $\text{\AA}$  range the contamination of the stellar continuum may be mainly due to  $H\beta$ , [OIII], and [NII] emission lines. Table 5.1 reports the rest wavelengths of all the candidate ionized gas emission lines in both the wavelength ranges.

Figure 5.1.4 shows how the potential gas emission in the masked regions is highlighted by the fit residuals drawn with a blue line. This figure corresponds to the spectral range 4500-5300  $\text{\AA}$ . Gas emission is clearly visible:  $H\beta$  and [OIII] line contributions being more visible and the [NII] contribution appearing more faint. No significant contribution is seen for the HeII emission line. Because of this the mask region related to the latter line was eliminated, while the others were retained during the following fits. In addition also the sky emission line at 5199  $\text{\AA}$  was masked.

In the lower spectral range 4000-4500  $\text{\AA}$  (see Figure 5.1.5) the masked regions of the spectrum do not show appreciable emission line features in the fit residuals so we decided

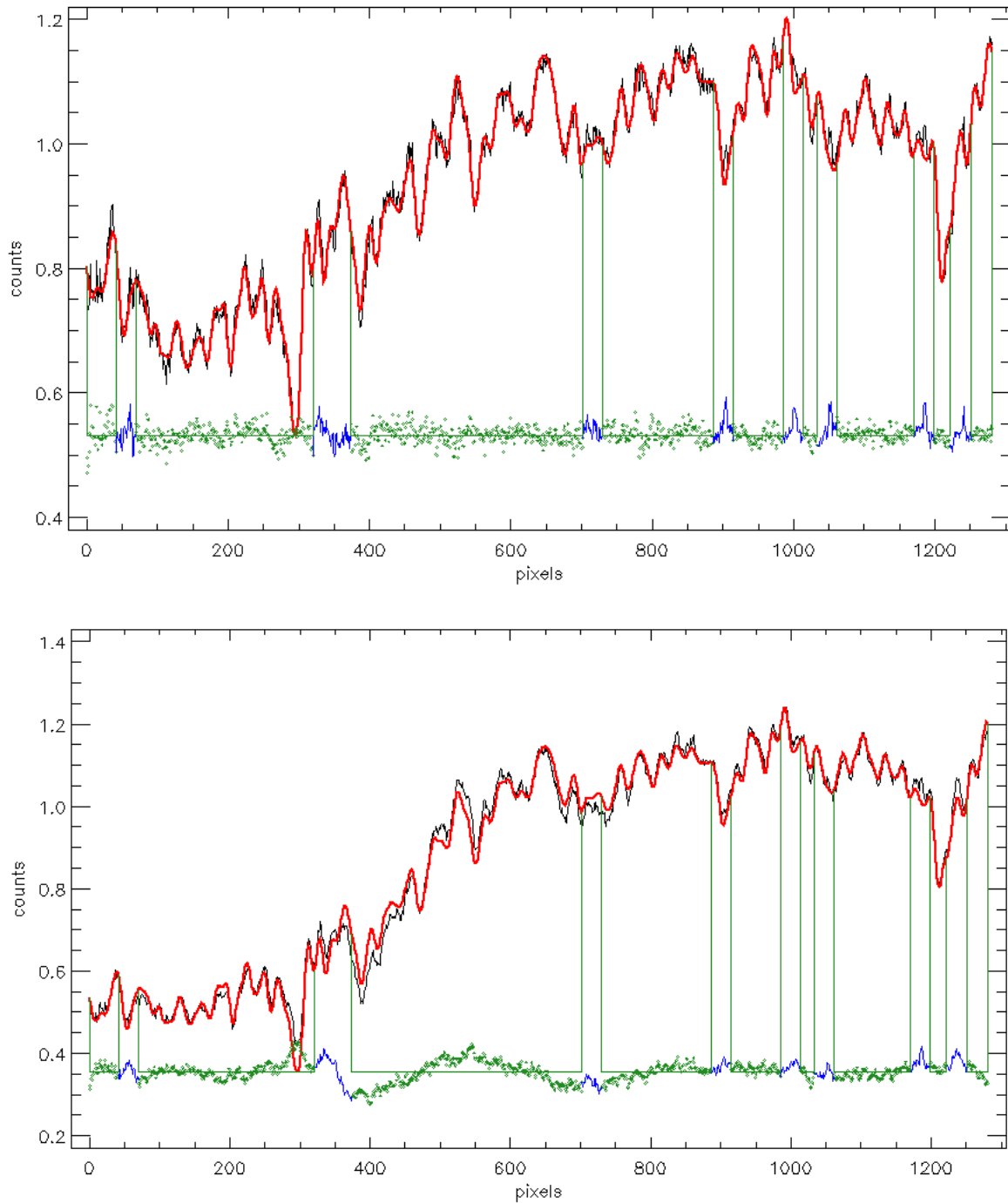


Figure 5.1.2: An example of a good match (*upper panel*) and a mismatch (*lower panel*) between a single NGC 3557 spectrum and the best fit found with pPXF. The plot components are as in Figure 5.1.1.

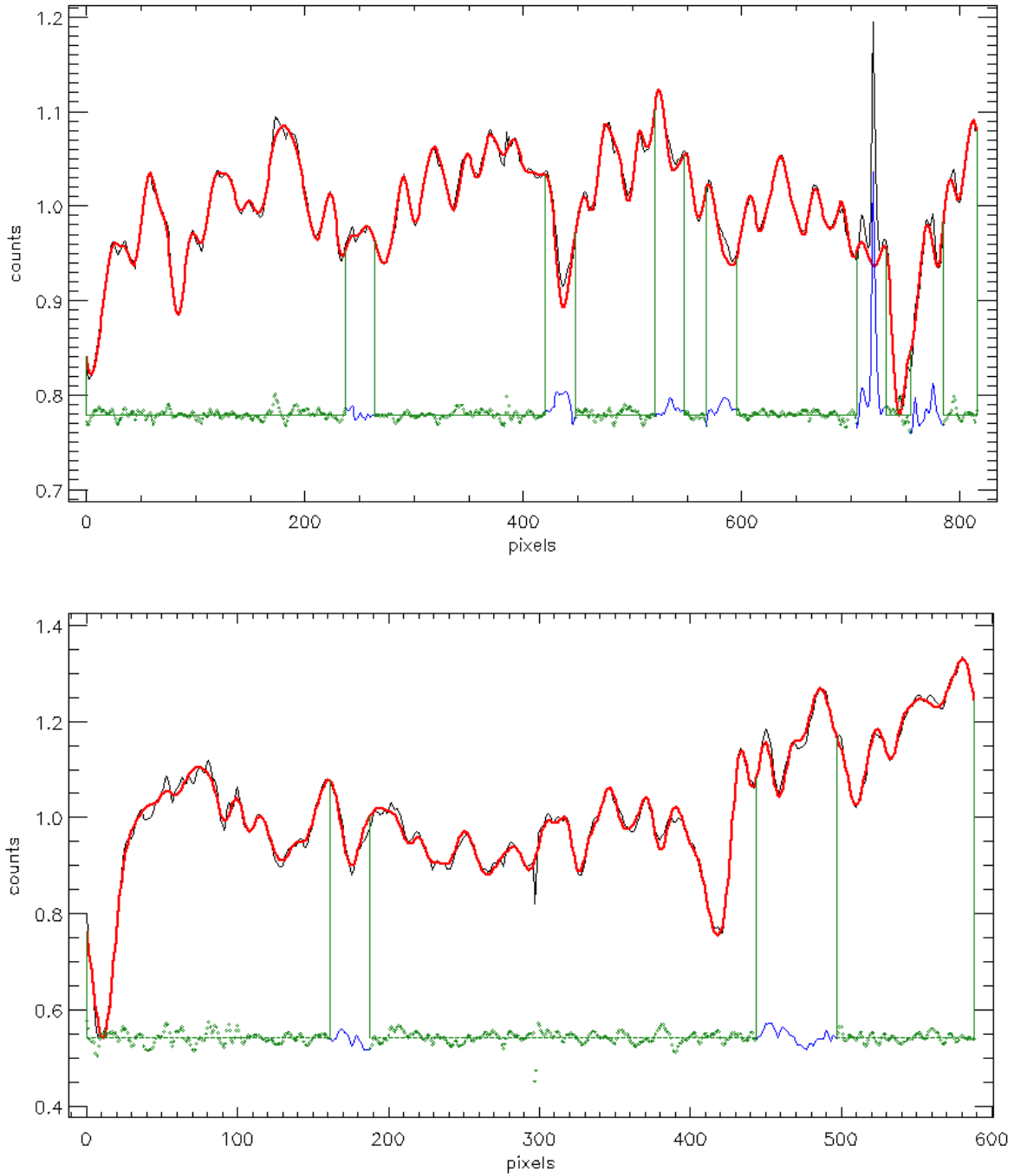


Figure 5.1.3: NGC 3557 integrated spectrum fit in the 4500-5300 Å (*upper panel*) and in the 4000-4500 Å (*lower panel*) ranges. In the upper panel the sky line at 5199 Å is clearly visible in the right part of the spectrum (at pixel  $\sim 725$ ). The plot components are as in Figure 5.1.1.

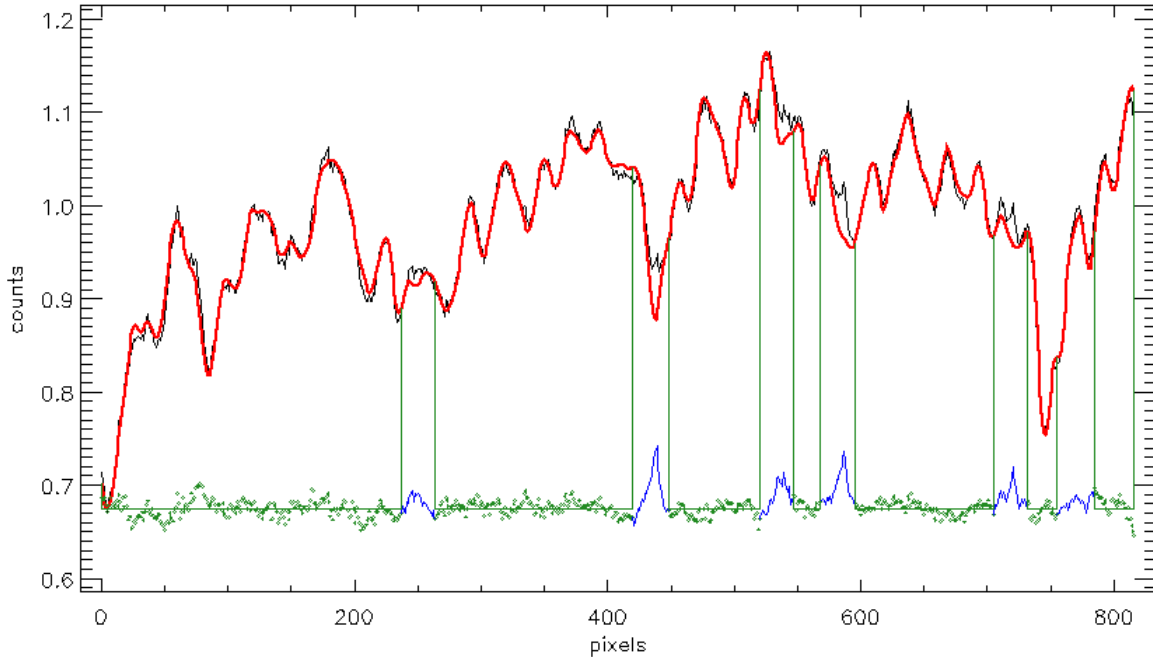


Figure 5.1.4: An example of spectrum showing gas emission in the 4500-5300 Å range in the centre of NGC 3557. The masked region corresponding to the 5199 Å sky emission line is located around pixel 725. The plot components are as in Figure 5.1.1.

to remove such masks in the following spectral fits.

At this point the signal and the noise of each spectrum have to be determined, in order to homogenize the signal to noise ratio (S/N) across the whole FoV. All the spectra were individually fitted using the previously determined optimal template. The signal was extracted as the median of the spectrum flux along the whole wavelength range, while the noise was assumed to be the standard deviation of the fit residuals. In this way we obtain for each spectrum an associated value for the signal and the noise. Having this information, the data were spatially binned with the adaptive Voronoi method<sup>3</sup> of Cappellari & Copin (2003), which optimally solves the problem of preserving the maximum spatial resolution of two-dimensional data, given a constraint on the minimum S/N. Being an adaptive binning method the size of the bin is automatically adapted to the local S/N: larger bins will be set to low S/N regions, while a higher spatial resolution will be retained in high S/N regions (i.e. the central part of the source). It is worth noting that this binning procedure reduces the final number of available spectra, by summing together the flux of all the spectra that belong to a single bin.

We decided to chose a minimum S/N=60 for our data. Figure 5.1.6 shows the results of the binning algorithm on the 4500-5300 Å range image. As can be noted, there are many bins where the desired S/N was not reached, in the external region of the FoV. In addition the bin size appears to be linked to its position in the FoV map in an unusual way. The bins are in general bigger in the upper-right side and in the lower-left side of the FoV.

<sup>3</sup>Available from <http://purl.org/cappellari/idl>

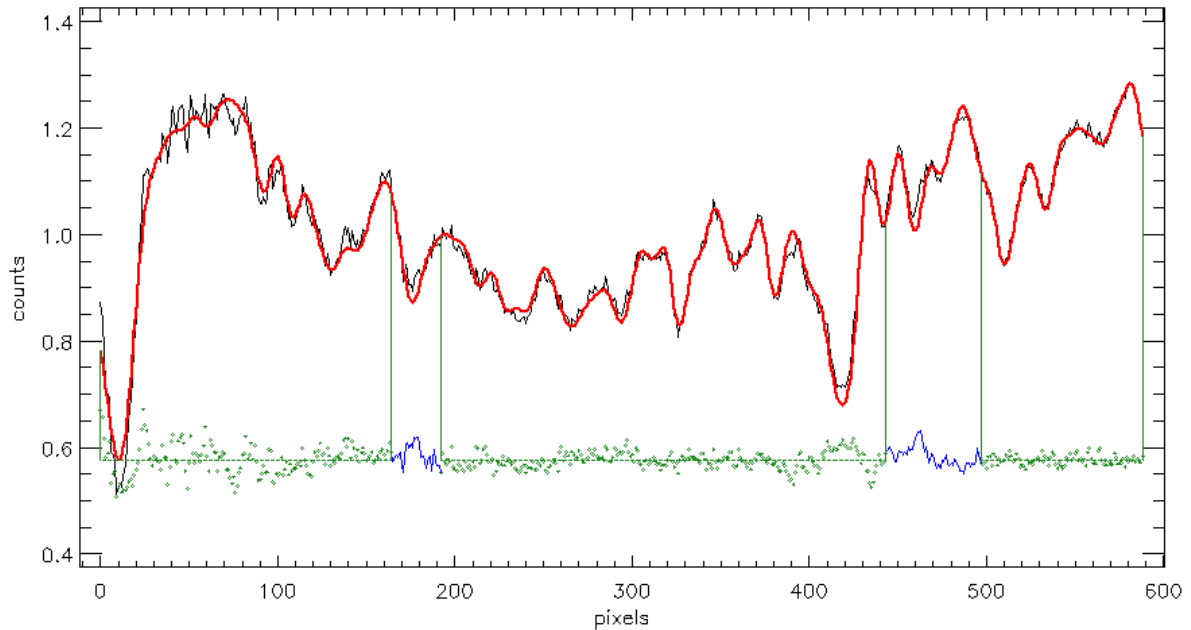


Figure 5.1.5: An example of spectrum covering the 4000-4500 Å range in the centre of NGC 3557. No significant gas emission is detected. The plot components are as in Figure 5.1.1.

The binning algorithm works better with the spectra in the 4000-4500 Å range (see Figure 5.1.7), despite the lower sensitivity of the detector in this spectral region. In this spectral range a constant S/N is reached over the entire map. Considering the typical seeing of our observations ( $\sim 1$  arcsec), the fact that the central regions are more coarsely binned with respect to the previous case is not a problematic issue, as the information from a single pixel cannot be considered to be rigorously independent from that of its neighbour.

The final fitting process was performed on the binned spectra. Each fitting was inspected in order to verify if template mismatch problems are eventually present or, alternatively, if the fit residuals show significant patterns. For each spectrum pPXF extracts information on the velocity  $V$ , the velocity dispersion  $\sigma$ , and the  $h_3$  and  $h_4$  moments. The  $h_3$  and  $h_4$  moments describe the departure of the LOSVD from a Gaussian in the wings and the core region respectively. They are difficult to analyze, because they heavily depends on the reliability of the Gaussian fitting of the LOSVD and on a very robust error analysis which is typically obtained through Monte Carlo simulations. This is beyond the scope of the present thesis, and the  $h_3$  and  $h_4$  analysis is postponed to future time.

## 5.2 Analysis of velocity and velocity dispersion maps

The velocity and velocity dispersion maps extracted from the spectra in the 4500-5300 Å and 4000-4500 Å range respectively, are presented in Figure 5.2.1 and Figure 5.2.2. The values found for the velocity are in the range  $\pm 180$  km s $^{-1}$  while the velocity dispersion goes from 200 up to 280 km s $^{-1}$ .

As can be noted, both velocity maps show an ordered rotation for the projected

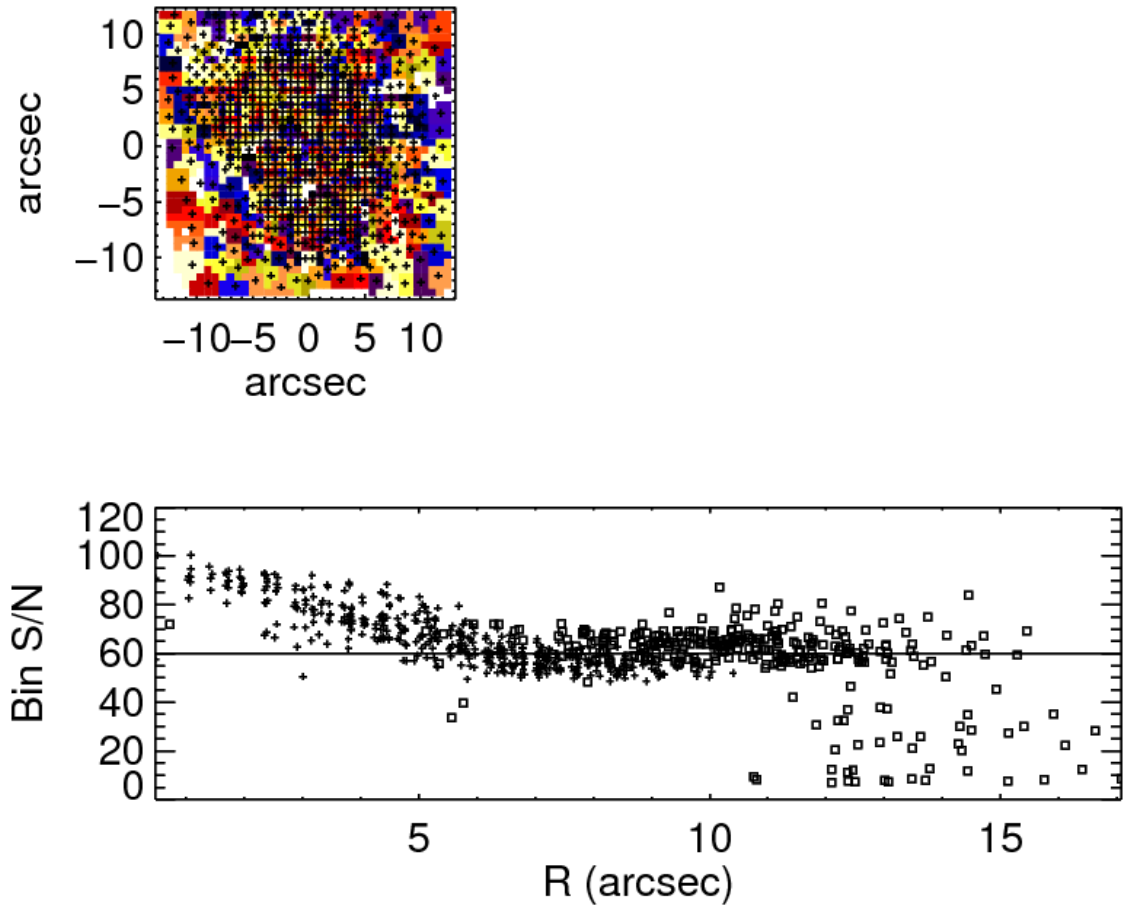


Figure 5.1.6: Results of the binning process for the 4500-5300 Å range. In the upper panel the FoV is shown: different bin are highlighted with different colors in order to distinguish them. The black cross symbols indicate the centre of each bin. In the lower panel the S/N of each bin is plotted as a function of the bin distance from the FoV centre, measured in arcsec. The black line marks the minimum required S/N (S/N=60).

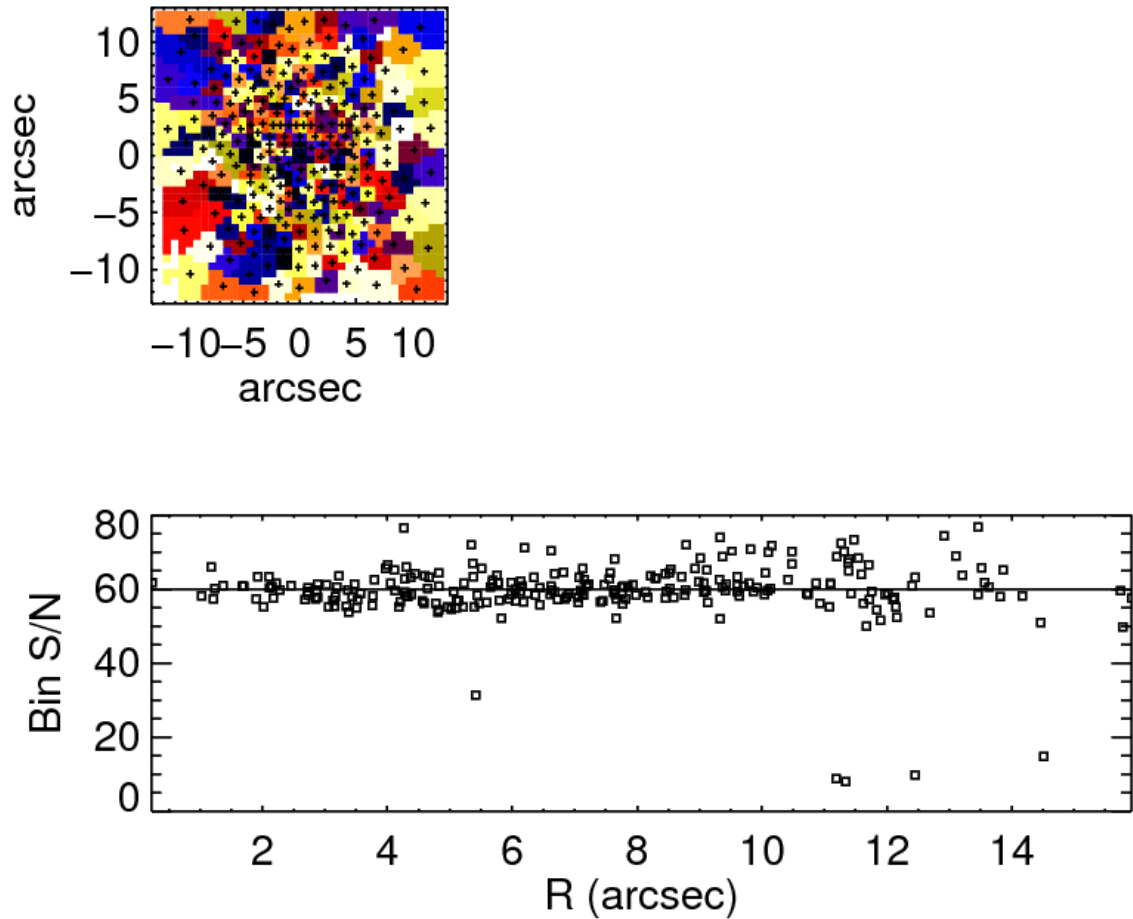


Figure 5.1.7: Results of the binning process for the 4000-4500 Å range. In the upper panel the FoV is shown: different bins are highlighted with different colors in order to distinguish them. The black cross symbols indicate the centre of each bin. In the lower panel the S/N of each bin is plotted as a function of the bin distance from the FoV centre, measured in arcsec. The black line marks the minimum required S/N (S/N=60).

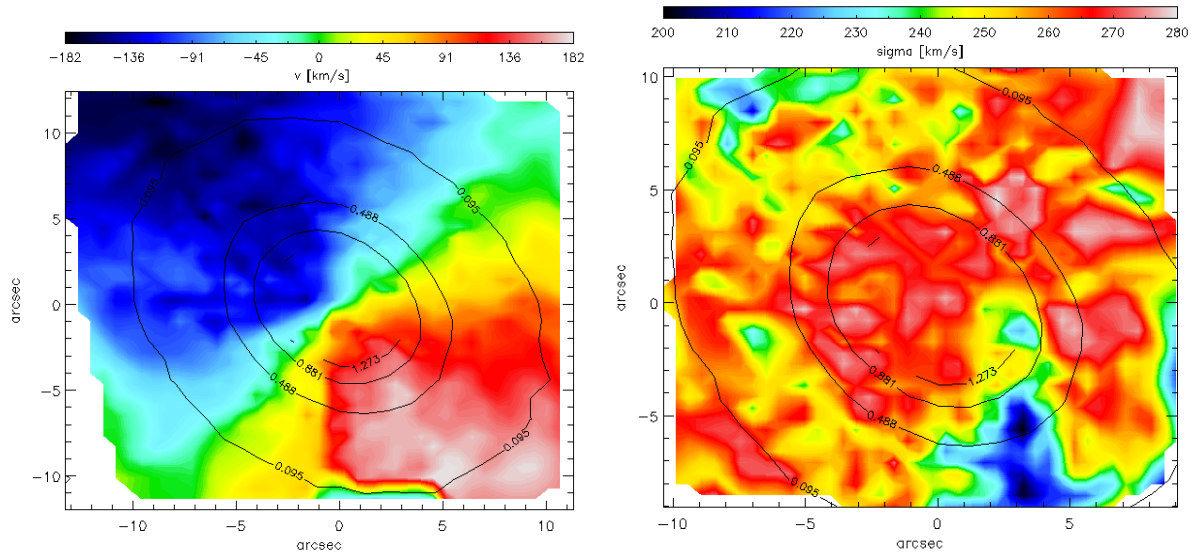


Figure 5.2.1: NGC 3557 velocity  $V$  (*left panel*) and velocity dispersion  $\sigma$  (*right panel*) maps extracted in the 4500-5300 Å range. The colour scale is indicated in the upper part of each panel together with the corresponding values. Representative isophotes of the HST NGC 3557 image are overlotted on the maps using solid black lines. The sky coordinates are measured in arcsec with the origin at the centre of NGC 3557.

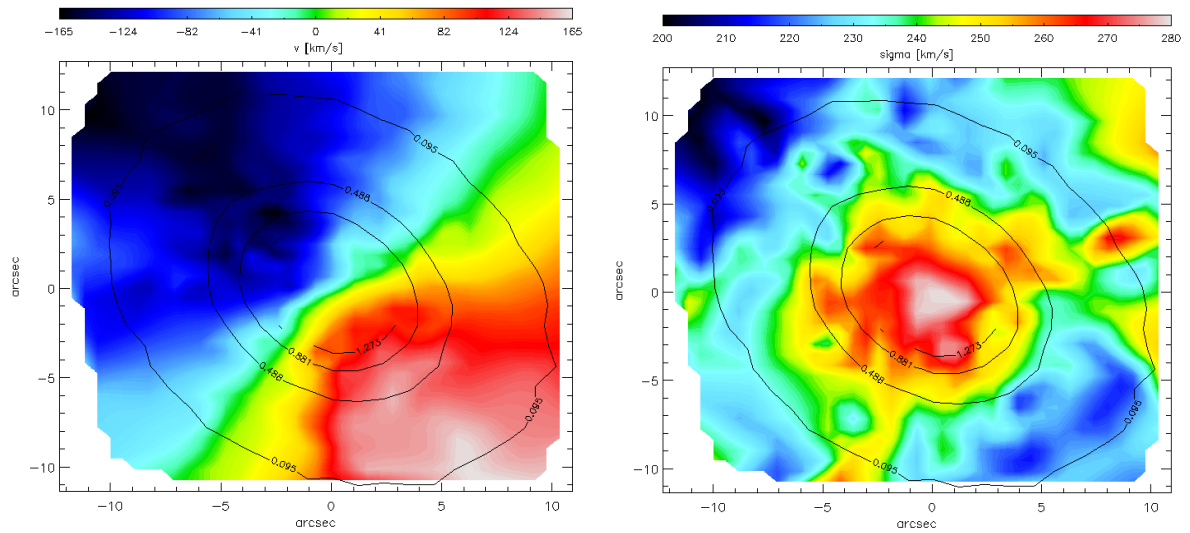


Figure 5.2.2: NGC 3557 velocity  $V$  (*left panel*) and velocity dispersion  $\sigma$  (*right panel*) maps in the 4000-4500 Å range. The colour scale is indicated in the upper part of each panel together with the corresponding values. Representative isophotes of the HST NGC 3557 image are overlotted on the maps using solid black lines. The sky coordinates are measured in arcsec with the origin at the centre of NGC 3557.

component of the stellar velocity field. The velocity fields have a disk-like structure and, comparing our results with the velocity maps presented in the ATLAS<sup>3D</sup> sample, NGC 3557 is ideally classifiable as a Regular Rotator.

The velocity dispersion map is however quite different when we compare the two wavelength ranges. The map extracted in the upper 4500-5300 Å range (Figure 5.2.1, *right panel*) shows an elongated structure characterized by high  $\sigma$  values extending along the minor axis of the galaxy. This is due to the large bins covering the outer parts of the galaxy, where the required S/N could not be reached during the binning process (see Figure 5.1.6 and related discussion). Ignoring these outermost bins the sigma maps looks more reasonable with no apparent elongation or perhaps a very weak one along the minor-axis. If real, such an elongation could be, in principle, produced by the presence of a young star component. Such component would presumably have formed in a disk i.e. in a spatially flatter structure. This indeed yields lower velocity dispersions along the disk, and higher dispersion values perpendicular to the disk i.e. along its rotation axis. Similar elongation are found in the ATLAS<sup>3D</sup> galaxy sample (Krajnović et al. 2011).

The velocity dispersion map extracted in the lower wavelength range (4000-4500 Å) looks more regular and similar to the dispersion velocity maps found for ATLAS<sup>3D</sup> regular rotators (Krajnović et al. 2011).

However, changing the wavelength range can in theory alter the appearance of the velocity dispersion map. Indeed the strongest absorption lines produced by young stars (e.g.  $H\beta$ ) are included in the 4500-5300 Å range.

Although we cannot exclude that the elongation visible in the 4500-5300 Å range is real (at least to some extent), we decided to focus our following analysis on the lower wavelength range i.e. 4000-4500 Å, where potential artefacts are not present.

An accurate estimate of the errors associated with  $v$  and  $\sigma$  values in our maps requires a Monte Carlo approach in which the kinematic parameters are derived from many realizations of the input spectrum, obtained by adding Poissonian noise to a model galaxy spectrum. We are confident that the errors estimated through Monte Carlo simulations for the SAURON project can be assumed as upper limits for our dataset; NCG 3557 data indeed have a better spectral sampling and spectral resolution, and the spectra are binned so as to reach the minimum S/N ratio (i.e. S/N=60) also assumed for the SAURON sample. Assuming a S/N=60, Emsellem et al. (2004) found  $1\sigma$  errors for  $V$  and  $\sigma$  of 4-8 km s<sup>-1</sup> and 5-7 km s<sup>-1</sup>, respectively.

### 5.3 Kinematic parameters $\Gamma_{kin}$ , $k_1$ , $k_5/k_1$

We performed the analysis of the kinematic parameters applying the KINEMETRY<sup>4</sup> routine to our velocity maps. Kinemetry provides a generalization of the surface photometry analysis to the higher order moments of the LOSVD. The moments of the LOSVD have odd or even parity. The surface brightness (zero moment  $k_0$ ) is even, the mean velocity (first moment  $k_1$ ) is odd, the velocity dispersion (second moment  $k_2$ ) is even, etc. The basic assumption of Kinemetry implies that for the odd moments the profile along each ellipse satisfies a simple cosine law,  $V = V_{rot}\cos(\theta)$ , where  $V_{rot}$  is the amplitude of rotation and  $\theta$  is the eccentric anomaly. For the even moments the profile is assumed to

---

<sup>4</sup>The IDL KINEMETRY routine can be found at <http://www.eso.org/~dkrajnov/idl>

be constant (the same assumption used in surface photometry). Applying Kinemetry to velocity maps thus consists in finding the best fitting ellipse along which the velocities can be described as a function of  $\cos(\theta)$ . Kinemetry performs a rigorous generalization of the photometric ellipse fitting. It determines the best-fitting ellipse by minimising the Fourier coefficients up to the 3rd. This ensures a more robust fit and also that the higher order Fourier terms are unaffected by the ellipse fit. Kinemetry first fits for the ellipse parameters: position angle  $\Gamma_{kin}$  and flattening of the ellipse  $q_{kin} = b/a$  (where  $b$  and  $a$  are the minor and major axes respectively). The axial ratio of the best-fitting ellipse is related to the opening angle of the isovelocity contours: the larger the axial ratio, the more open are the contours of the velocity map. The velocity profile is then decomposed into odd Fourier harmonics. The first order term  $k_1$  is equivalent to  $V_{rot}$ , while the higher ones show departures of the velocity profiles from the assumed cosine law.

The deviation from the assumed law can be quantified looking at the amplitude of the  $k_5$  harmonics. As noted in Krajnović et al. (2011), it is however better to use a scale free measure which is obtained by dividing  $k_5$  by the rotation velocity described by  $k_1$ .

It should be noted that all the parameters extracted via Kinemetry are calculated up to a maximum ‘‘aperture’’ radius for which the corresponding ellipse differs in area not more than 15% from the actual FoV covered by our spectrograph (Emsellem et al. 2007). In our case such maximum aperture corresponds to  $\simeq 13$  arcsec.

The results of Kinemetry obtained for NGC 3557 are shown in Figure 5.3.1.

Figure 5.3.1 shows that the position angle  $\Gamma_{kin}$ , and the velocity  $k_1$  radial profiles have typical values of  $\sim 45^\circ$  and  $\sim 130$  km s<sup>-1</sup> respectively, and do not show significant variations as a function of the distance ( $R$ ) from the galaxy centre. This flat behaviour is typical of galaxies classified as Regular Rotator (RR) with no significant features (NF) (see Krajnović et al. 2011).

A luminosity weighted average ratio  $\overline{k_5/k_1}$  could be estimated, from the radial profile, following the prescription of Ryden et al. (1999), as detailed below. The luminosity weighted average  $G_R$  of a generic quantity  $G(r)$  (where  $r$  is the semimajor-axis of the fitting ellipse), within a radius  $R$ , derived from its radial profile, is defined as:

$$G_R = \frac{\int_0^R q(R) F(R) G(R) R dR}{\int_0^R q(R) F(R) R dR} \quad (5.3.1)$$

where  $q(R)$  and  $F(R)$  are the best-fitting ellipse axis ratio and the surface brightness profiles respectively. Using a sampled radial profile, the latter equation can be approximated with:

$$G_R \sim \frac{\sum_{k=1}^N q(R_k) F(R_k) G(R_k) (R_{out,k}^2 - R_{in,k}^2)}{\sum_{k=1}^N q(R_k) F(R_k) (R_{out,k}^2 - R_{in,k}^2)} \quad (5.3.2)$$

where  $R_{out,k}$  and  $R_{in,k}$  correspond to the inner and the outer radii of the  $k$ -th annulus respectively.

In particular, the values of  $\overline{k_5/k_1}$  are determined within the semi-major axis ( $R \cong 13$  arcsec) of the largest best fitting ellipse that is enclosed by the velocity map. The values

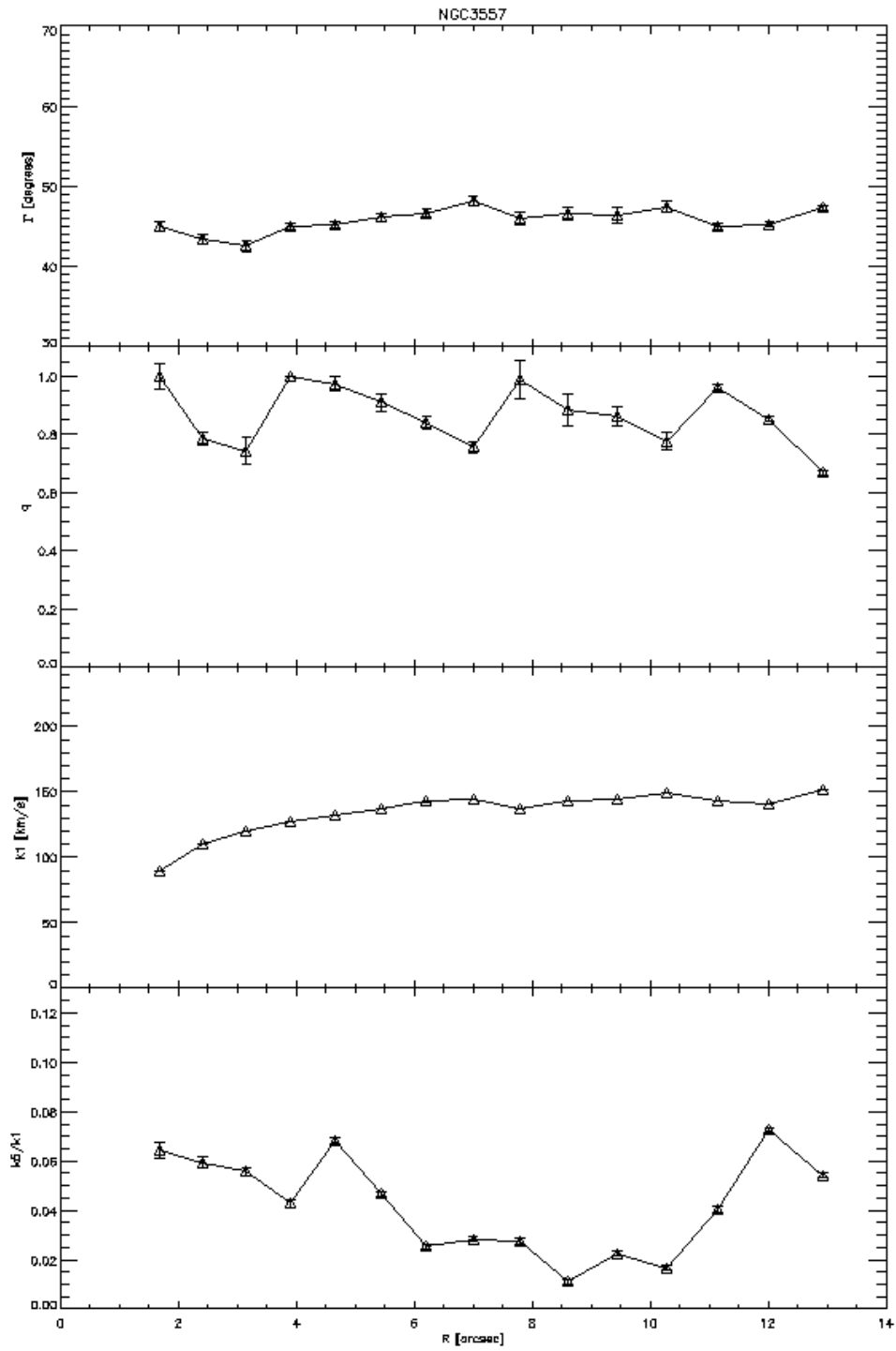


Figure 5.3.1: Results of Kinemetry on the NGC 3557 velocity map. From top to bottom: radial profiles of  $\Gamma_{kin}$ ,  $q_{kin}$ ,  $k_1$ ,  $k_1/k_5$ .

of  $q(R)$  and  $F(R)$  are derived from the HST image (see Figure 2.5.2, *central panel*) for the same radii sampled by kinemetry on the velocity map. The extracted value is  $\overline{k_5/k_1}=0.07$ .

It should be noted that the  $k_5/k_1$  threshold estimated for the ATLAS<sup>3D</sup> sample by Krajnović et al. (2011), as a minimum reliable value to assess the presence of significant departures from the cosine law is  $k_5/k_1 \geq 0.04$ . Such value was estimated from a Monte Carlo error analysis where a lower minimum S/N threshold was assumed in the velocity map extraction (i.e. S/N=40 against our S/N=60). Therefore the minimum  $k_5/k_1$  threshold to be applied to our data should be, in principle, lower and more similar to the one assumed for the SAURON sample ( $k_5/k_1 > 0.02$ ) where the same S/N=60 was assumed.

A value  $\overline{k_5/k_1}=0.07$  can be therefore considered as unusually high for a Regular Rotator, as it indicates that significant departures from the cosine law are present in the velocity map.

This issue will be further discussed in Chapter 6.

## 5.4 Kinematic misalignment: $PA_{phot}$ , $PA_{kin}$ and $\Psi$

The photometric position angle ( $PA_{phot}$ ) represents the orientation of the stellar distribution and it defines the position of the apparent photometric major axis measured East of North. We derived  $PA_{phot}$  from the HST image of NGC 3557 using the FIND\_GALAXY<sup>5</sup> routine that calculates the moments of inertia of the surface brightness distribution. The computation is iterated using an increasing fraction of pixels (i.e. on growing ellipses). This procedure provides also the global galaxy ellipticity  $\varepsilon \equiv 1 - \frac{b}{a}$ . The standard deviation derived from the above measurements provides an estimate of the uncertainties on  $PA_{phot}$  and  $\varepsilon$ . The derived values for  $PA_{phot}$  and  $\varepsilon$  are  $PA_{phot}=33.0^\circ \pm 0.2$  and  $\varepsilon=0.243 \pm 0.001$ . It should be noted that both the  $PA_{phot}$  and  $\varepsilon$  present very little variations for increasing “aperture” radii and can be assumed to be nearly constant along the entire region of the galaxy probed by the HST image.

As a double-check we also derived the photometric parameters directly from Kinemetry through the analysis of the zero moment ( $k_0$ ) of the HST image, which corresponds to its surface brightness. We found  $\Gamma_{phot}=33.5^\circ \pm 1.3$  and  $q=0.252 \pm 0.006$  in good agreement with the values reported above and estimated using FIND\_GALAXY.

The global kinematic position angle ( $PA_{kin}$ ), on the other hand, is the angle which describes the orientation of the mean stellar motion on a velocity map. It usually defines the angle between the North and the receding part of the velocity map. We measured it using the FIT\_KINEMATIC\_PA<sup>6</sup> routine. For any chosen  $PA_{kin}$  a bi-(anti)symmetric velocity map is constructed (mirrored around an axis with the position angle  $PA_{kin} + 90^\circ$ ). The best  $PA_{kin}$  is defined as the angle which minimises the difference between the symmetrised and the observed velocity maps. The error is defined as the smallest opening angle that encloses the position angles of all the models for which the symmetrised and observed data are consistent within a chosen confidence level. The latter is defined by  $\Delta\chi^2 < 9 + 3\sqrt{2N}$ , where  $\Delta\chi^2 < 9$  is the standard  $3\sigma$  confidence level for one parameter, and the additional term accounts for the  $3\sigma$  uncertainties in  $\Delta\chi^2$ .

<sup>5</sup>The IDL routine FIND\_GALAXY.PRO is a part of the MGE package that can be found at <http://www.purl.org/cappellari/idl>.

<sup>6</sup>The IDL FIT\_KINEMATIC\_PA.PRO is publicly available at <http://www.purl.org/cappellari/idl>.

360 different bi-symmetrised maps were produced, with  $0.5^\circ$  steps in position angle ranging from  $0^\circ$  to  $180^\circ$ . The best value was found to be  $PA_{kin}=47^\circ\pm 3$ . The systemic velocity of NGC 3557 was also extracted and was found to be  $v_{syst}=3060.86\text{ km s}^{-1}$ .

We notice that  $PA_{kin}$  is in very good agreement with the  $\Gamma_{kin}$  values previously derived using Kinemetry (see Section 5.3).

Following Franx et al. (1991), the kinematic misalignment angle  $\Psi$  is defined as the difference between the measured photometric and kinematic position angles:

$$\sin\Psi = |\sin(PA_{phot} - PA_{kin})|. \quad (5.4.1)$$

$\Psi$  provides a good approximation of the true kinematic misalignment angle, which should be measured between the intrinsic minor axis and the intrinsic angular momentum vector. In this parametrization,  $\Psi$  lies between  $0$  and  $90^\circ$  and it is not sensitive to differences of  $180^\circ$  between  $PA_{phot}$  and  $PA_{kin}$ . In the case of NGC 3557  $\Psi$  is equal to  $14^\circ\pm 3$ . This value lies near the threshold (i.e.  $\Psi = 15^\circ$ ) that, according to Krajnović et al. (2011), separates aligned and misaligned structures. However the ATLAS<sup>3D</sup> galaxies classified as misaligned usually shows values significantly larger than  $15^\circ$ . Therefore we can conclude that the internal region of NGC 3557 is likely to show no or at most a low misalignment between the photometric and the kinematic structures, in line with what found for regular rotating structures. This seems to indicate that we are dealing with an axisymmetric system that, during its formation history retained a disk-like structure, at least in its central region.

## 5.5 Anisotropy diagram ( $V/\sigma - \varepsilon$ ) and angular momentum ( $\lambda_R$ )

The relation between  $V/\sigma$  and the mean ellipticity  $\varepsilon$ , i.e. the anisotropy diagram, was recently revisited by Binney (2005) to design a more robust diagnostics of the velocity anisotropy in galaxies using 2D kinematic information. Binney reformulated the ratio of ordered versus random motions in terms of integrated quantities observable with integral-field spectrographs, namely  $\langle V \rangle$  and  $\langle \sigma \rangle$ , where  $V$  and  $\sigma$ , respectively denote the observed stellar velocity and velocity dispersion, and the brackets indicate a sky averaging weighted by the surface brightness, following the general equation:

$$\langle G \rangle = \frac{\sum_{i=1}^{N_p} F_i G_i}{\sum_{i=1}^{N_p} F_i} \quad (5.5.1)$$

where  $G$  is the parameter to be averaged, and the sums extend over a defined region of the sky.  $N_p$  is the total number of pixels and  $F_i$  is the flux value within the  $i$ -th pixel.

The values of  $\langle V \rangle$  and  $\langle \sigma \rangle$  for NGC 3557 were estimated using Equation 5.5.1 up to an ‘‘aperture’’ radius of  $\sim 16$  arcsec. It should be noted that we use  $v$  and  $\sigma$  values extracted from the binned maps via pPXF; the  $i$  index in Equation 5.5.1 therefore indicates the  $i$ -th bin. The found values are reported in Table 5.2.

$\langle V \rangle$	$\langle \sigma \rangle$	$\frac{\langle V \rangle}{\langle \sigma \rangle}$
$km s^{-1}$	$km s^{-1}$	
85,7	251	0.34

Table 5.2:  $\langle V \rangle$ ,  $\langle \sigma \rangle$  and their ratio found for NGC 3557 within the maximum “aperture” radius ( $\sim 16$  arcsec).

Figure 5.5.1 shows the anisotropy diagram for the SAURON sample galaxies. Cappellari et al. (2007) identified a region ( $0.0 \lesssim \varepsilon \lesssim 0.3$ ,  $0.0 \lesssim (V/\sigma)_e \lesssim 0.13$ ) where Slow Rotators are generally found. We can use the values found for NGC 3557 ( $\frac{\langle V \rangle}{\langle \sigma \rangle} = 0.34$  and  $\varepsilon = 0.24$ ) to infer a first classification. Our galaxy clearly lies outside the *Slow Rotator* region, indicating that a *Fast Rotator* classification is more likely, at least in its central part. However a direct comparison with the SAURON sample may be misleading as we are probing  $\sim 0.4 R_e$  while the diagram refers to values estimated up to  $1 R_e$ .

Emsellem et al. (2007) showed that the revisited anisotropy diagram fails to provide a way to differentiate some galaxies with stellar velocity fields qualitatively and quantitatively very different. They found a new empirical way to quantify the global kinematics of a galaxy: the angular momentum  $\lambda_R$  (Equation 1.4.1).

The parameter  $\lambda_R$  can be measured via two-dimensional spectroscopy from:

$$\lambda_R = \frac{\sum_{i=1}^{N_p} F_i R_i |V_i|}{\sum_{i=1}^{N_p} F_i R_i \sqrt{V_i^2 + \sigma_i^2}}, \quad (5.5.2)$$

where  $F_i$  is the flux in the  $i$ th bin,  $R_i$  its distance from the centre, and  $V_i$  and  $\sigma_i$  are the corresponding stellar velocity and velocity dispersion extracted from the binned spectrum.

The estimated values of the  $\lambda_R$  parameter as a function of radius for NGC 3557 are reported in Table 5.3. The maximum “aperture” radius is defined as done for the kinometry measurements, following the prescription of Emsellem et al. (2007). With this criterion we could calculate the  $\lambda_R$  up to a radius  $R_{max} = 16.21 \text{ arcsec}$  (i.e.  $0.4 R_e$ ), where we measure  $\lambda_{R_{max}} = 0.34$

Emsellem et al. (2007) report that  $\lambda_R$  radial profile of *Fast* and *Slow Rotators* are qualitatively different. The  $\lambda_R$  radial profiles of *Fast Rotators* are found to be significantly rising, while for *Slow Rotators* the observed profiles are decreasing or nearly flat. It should be noted that in Emsellem et al. (2007) the classification criterion was determined by a simple  $\lambda_R$  threshold (estimated at  $R = 1R_e$ ) with *Fast* and *Slow Rotators* lying respectively above and below  $\lambda_R = 0.1$ . Despite the high value of  $\lambda_{R_{max}}$  found for NGC 3557, its radial profile is nearly flat (it presents a very weak rise as a function of  $R$ ) and therefore is more consistent with the *Slow Rotator* class.

Assuming that our  $\lambda_{R_{max}}$  is representative of the  $\lambda_R$  value at  $R_e/2$ , we can use the refined criterion of Emsellem et al. (2011) to better classify NGC 3557. Applying Equation 1.4.3, (assuming the  $\varepsilon = 0.24$  as found for NGC 3557) the threshold value that separates *Fast* from *Slow Rotators* is  $\lambda_{R_e/2} = 0.12$ . The NGC 3557  $\lambda_{R_{max}}$  value clearly lies above this limit and looking at Figure 1.4.2 (*left panel*) our galaxy falls in the *Fast Rotator* region. However, the fact that we can only probe apertures smaller than

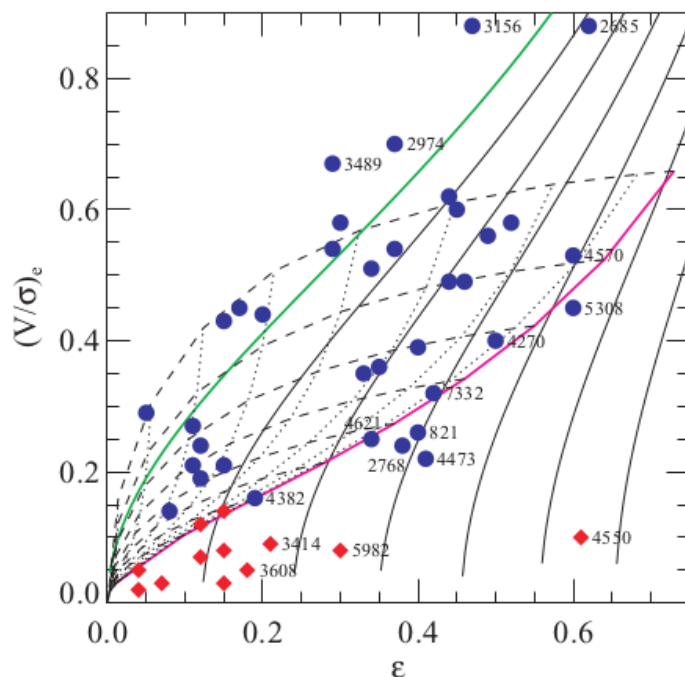


Figure 5.5.1: The anisotropy diagram for the 48 galaxies in the SAURON sample. The red diamonds and the blue circles refer to *Slow* and *Fast Rotators* respectively. The magenta line shows the edge-on view for ellipsoidal galaxies integrated up to infinity (using  $\beta = 0.7 \times \varepsilon_{intr}$ ). The black dashed lines correspond (from top to bottom) to equally spaced decreasing values of the  $\varepsilon_{intr}$ . The black dotted lines show the location of galaxies, originally on the magenta line, when the inclination is varied. The grid of solid curves shows (from left to right) the location on this diagram of edge-on oblate galaxies with increasing anisotropy. Edge-on isotropic models ( $\beta = 0$ ) are shown by the thick green line.

$\lambda_R$	$R [arcsec]$
0.19	2
0.24	3
0.26	4
0.28	5
0.28	6
0.30	7
0.31	8
0.32	9
0.32	10
0.32	11
0.33	12
0.33	13
0.33	14
0.33	15
0.33	16

Table 5.3: NGC 3557  $\lambda_R$  values as a function of the “aperture” radius.

$R_e/2$  makes our  $\lambda_R$  measurement more dependent on instrumental characteristics and observational conditions. Indeed the classification criterion used for the ATLAS<sup>3D</sup> sample was empirically determined and depends on the scale used.

The velocity dispersion is usually calculated at the effective radius  $R_e$ , which for NGC 3557 corresponds to 40 arcsec (Govoni et al. 2000). NGC 3557 velocity dispersion at  $R_e$  ( $\sigma_e$ ) was extrapolated by inverting the following Equation (Cappellari et al. 2006):

$$\left(\frac{\sigma_R}{\sigma_e}\right) = \left(\frac{R}{R_e}\right)^{-0.066 \pm 0.035} \quad (5.5.3)$$

derived by fitting  $\sigma$  as a function of  $R$  for the SAURON sample. We use the velocity dispersion reported in Table 5.2 (i.e.  $\sigma_R = \langle \sigma \rangle = 251 \text{ km s}^{-1}$ ) and assume  $R/R_e=0.4$ . The value found for NGC 3557 is  $\sigma_e = 236 \pm 9.1 \text{ km s}^{-1}$ .

This value can be used for an estimate of the virial mass of NGC 3557. The following Equation (Cappellari et al. 2006) was used:

$$M_{vir} \sim 5.0 \frac{R_e \sigma_e^2}{G} \quad (5.5.4)$$

where  $G$  is the Gravitational constant.

Assuming a standard  $\Lambda - CDM$  cosmology with  $H_0 = 71 \text{ km s}^{-1} \text{ Mpc}^{-1}$ ,  $R_e$  corresponds to 8.32 kpc and the estimated virial mass is  $M_{vir} \sim 5.4 \times 10^{11} M_\odot$ .

# Chapter 6

## NGC 3557: General Discussion and Conclusions

### 6.1 NGC 3557 kinematics: an open scenario

NGC 3557 is a very bright ( $M_K = -26.08$ ) and consequently massive galaxy, characterized by a low ellipticity ( $\varepsilon=0.24$ ). These properties indicate that NGC 3557 is a good *Slow Rotator* candidate (Emsellem et al. 2011, Cappellari et al. 2011). Indeed in the ATLAS<sup>3D</sup> sample only 11% (4/36) of all *Slow Rotators* are low mass objects ( $M_{dyn} < 10^{10.5} M_\odot$ ). All other *Slow Rotators* (32/36) are relatively round objects on the sky ( $\varepsilon_e < 0.4$ ), and are massive ( $M_{dyn} > 10^{10.5} M_\odot$ ). They often present Kinematically Distinct Cores (Emsellem et al. 2011).

Figure 6.1.1 shows the K band luminosity histogram for ATLAS<sup>3D</sup> galaxies in bins of  $\lambda_{R_e}$  (*upper panel*). It is clear how fast-rotating systems brighter than  $M_K = -24$  are rare, while all galaxies brighter than  $M_K = -25$  have  $\lambda_{R_e} \leq 0.2$ . A similar trend is found when considering  $\lambda_R$  at  $R_e/2$  (*lower panel*).

A few *Fast Rotators* are found up to  $M_K \simeq -25$ , but the brightest galaxies ( $M_K \simeq -26$ ) are all slow Rotators.

The fact that a massive galaxy like NGC 3557 is classified as a *Fast Rotator* is therefore very puzzling.

Krajnović et al. (2011) report that the 2D kinematic analysis may be influenced by instrumental effects. These are mainly related to the spatial coverage (or, in other words, to the size of the FoV) and/or to the spatial resolution of the instrument. Indeed some galaxies reveal a different global kinematic structure on small and larger scales. For example the ATLAS<sup>3D</sup> NGC3607 and NGC4278 galaxies (see Figure 6.1.3) are classified as Regular (Fast) Rotator galaxies based on kinemetry measurements performed up to  $R_{max} \approx 0.6 - 0.7 R_e$  (see Table 6.1), but Krajnović et al. (2011) argue that their classification may turn to Non-Regular Rotators/KDC galaxies, over a full  $1R_e$  scale.

name	$\varepsilon$	$\Psi$	$\overline{k_5/k_1}$	$k_1^{max}$	Dust	KinStruc	Group	$M_k$	$R_{max}/R_e$	F/S
NGC3607	0.13	3.3	0.028±0.013	113.3	dusty disk	RR/NF	<i>e</i>	-24.74	0.60	F
NGC4278	0.09	29.5	0.035±0.016	74.2	none	RR/NF	<i>e</i>	-23.80	0.72	F

Table 6.1: The table reports the main properties of the ALTAS<sup>3D</sup> NGC 3607 and NGC 4278 galaxies.

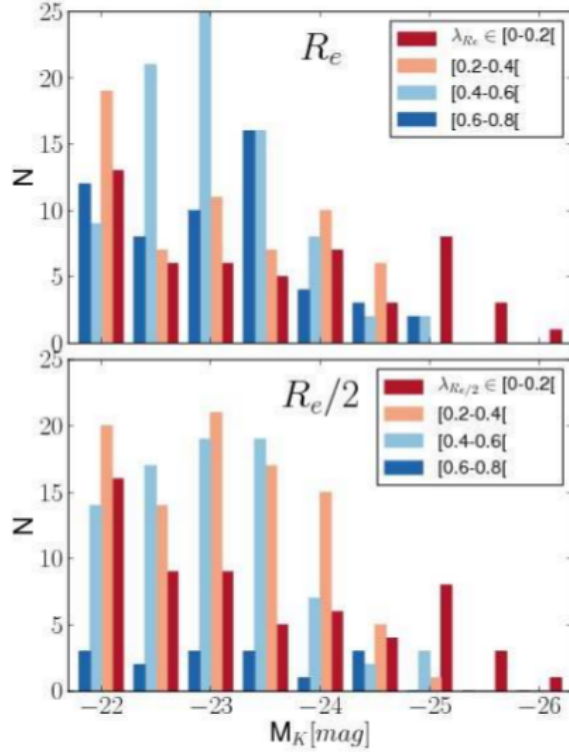


Figure 6.1.1: Distribution in K band luminosity for the ATLAS<sup>3D</sup> sample. Different bins in  $\lambda_{R_e}$  are highlighted (red:[0-0.2]; light red: [0.2-0.4]; light blue: [0.4-0.6]; blue: [0.6-0.8]). The *top panel* refers to  $\lambda_R$  values derived for an aperture radius of  $1R_e$  ( $\lambda_{R_e}$ ); the *bottom panel* refers to  $\lambda_R$  values derived for an aperture radius of  $R_e/2$  ( $\lambda_{R_e/2}$ ).

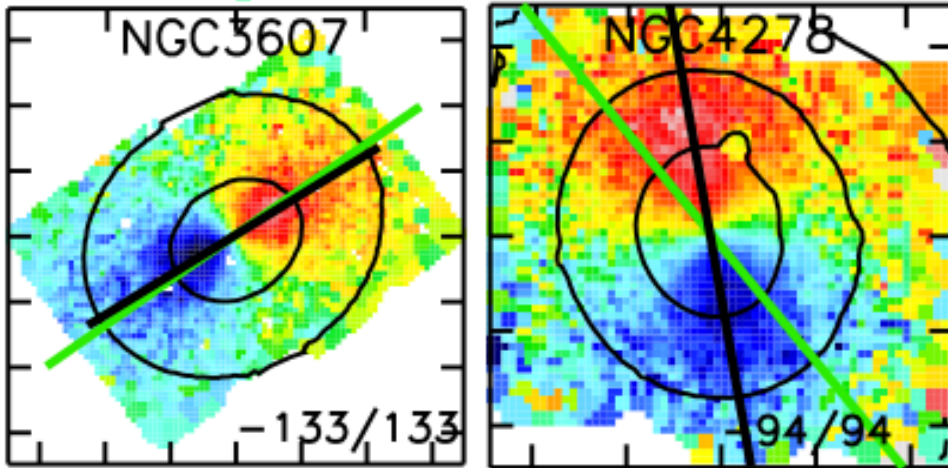


Figure 6.1.2: Velocity maps of NGC3607 (*left panel*) and NGC4278 (*right panel*). Contours are isophotes of the surface brightness. Maps are Voronoi binned. The number in right corners show the range of plotted velocities in  $\text{km s}^{-1}$ . The photometric and kinematic major axis are plotted using a green and a black solid line respectively. Ticks are separated by  $10''$ .

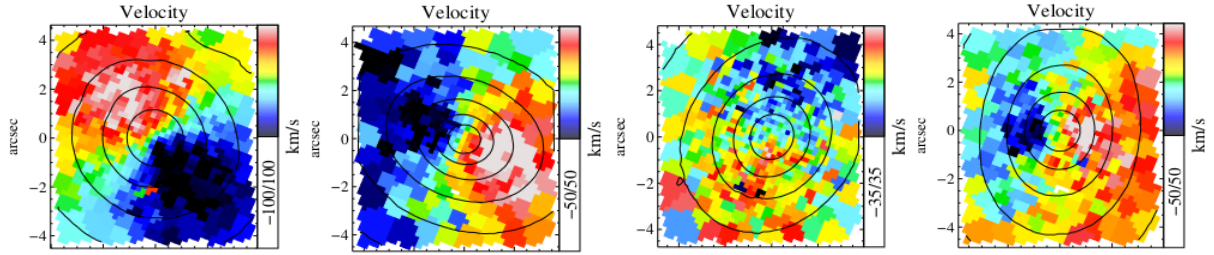


Figure 6.1.3: Velocity maps of NGC 5813, 3414, 3608, and 5982 (from left to right) extracted from OASIS data. The velocity range and colour scale are indicated on the right side of each panel. Black lines are representative isophotes. All the maps are Voronoi binned.

For the particular case of NGC 4278 they report that the mean velocity shows a decreasing profile towards the edge of the FoV ( $R \simeq 0.7 R_e$ ). In that respect, the observed rotation might belong to a large Kinematically Distinct Core covering the entire FoV. Only complete sampling of the effective radius would solve this issue.

Similar cases were found in a sub-sample of 28 SAURON galaxies that were additionally observed with the Integral Field Spectrograph OASIS (Krajnović et al. 2008; McDermid et al. 2006), which probes the nuclear region of these galaxies in more detail. The OASIS FoV is only  $10 \times 8 \text{ arcsec}^2$ , but the spatial scale is  $0.27 \times 0.27 \text{ arcsec}^2$ , significantly improving the spatial resolution with respect to SAURON. Kinematic profiles of the OASIS data clearly show structures that are only partially resolved in SAURON data, such as KDC or corotating components, corresponding to the nuclear disks visible in the HST images.

It should be noted that the one-to-one relation between *Slow Rotators* and objects with large higher order harmonic terms (i.e.  $k_5/k_1$ ) is significant and correctly reflects the internal structure of galaxies only when SAURON data are used. The OASIS data cover only a small fraction of the effective radius and do not show such a clear relationship.

Here are reported the cases of four galaxies (NGC 3414, 3608, 5813 and 5982) classified as *Slow Rotators* when sampled at  $\sim 1 R_e$ , but showing considerable rotation in their centres. Figure 6.1.3 shows the velocity maps of the central regions of the aforementioned galaxies when observed with OASIS. The maps show significant rotation to be ascribed to a KDC covering the full OASIS FoV. OASIS Kinemetry parameters of the four galaxies are shown in Figure 6.1.4 (*lower panels*), and are indicated with open blue circles. As can be noted  $k_5/k_1$  values are unusually high with respect to the regular velocity field seen over the OASIS FoV. Figure 6.1.4 also shows the velocity maps (*upper panels*) and the kinemetry parameters (black filled circles) extracted for the same galaxies using SAURON data. The regular rotating structures observed with OASIS are clearly visible in the central region of SAURON velocity maps.

The sizes of the KDCs found in these galaxies are listed in Table 6.2.

The aforementioned findings may explain the lack of correspondance between the observed regular velocity field and the high values of  $k_5/k_1$  found for NGC 3557, and may indicate that a large ( $\approx 0.4 R_e$ ) KDC (like the ones suggested on even larger scale for the ATLAS<sup>3D</sup> NGC 3607 and NGC 4278 galaxies) can significantly influence the kinematic classification of our object.

This would also reconcile the kinematic and photometric properties of NGC 3557 as only *Slow Rotators* (possibly with KDCs) are found among round massive ( $M_K \sim -26$ )

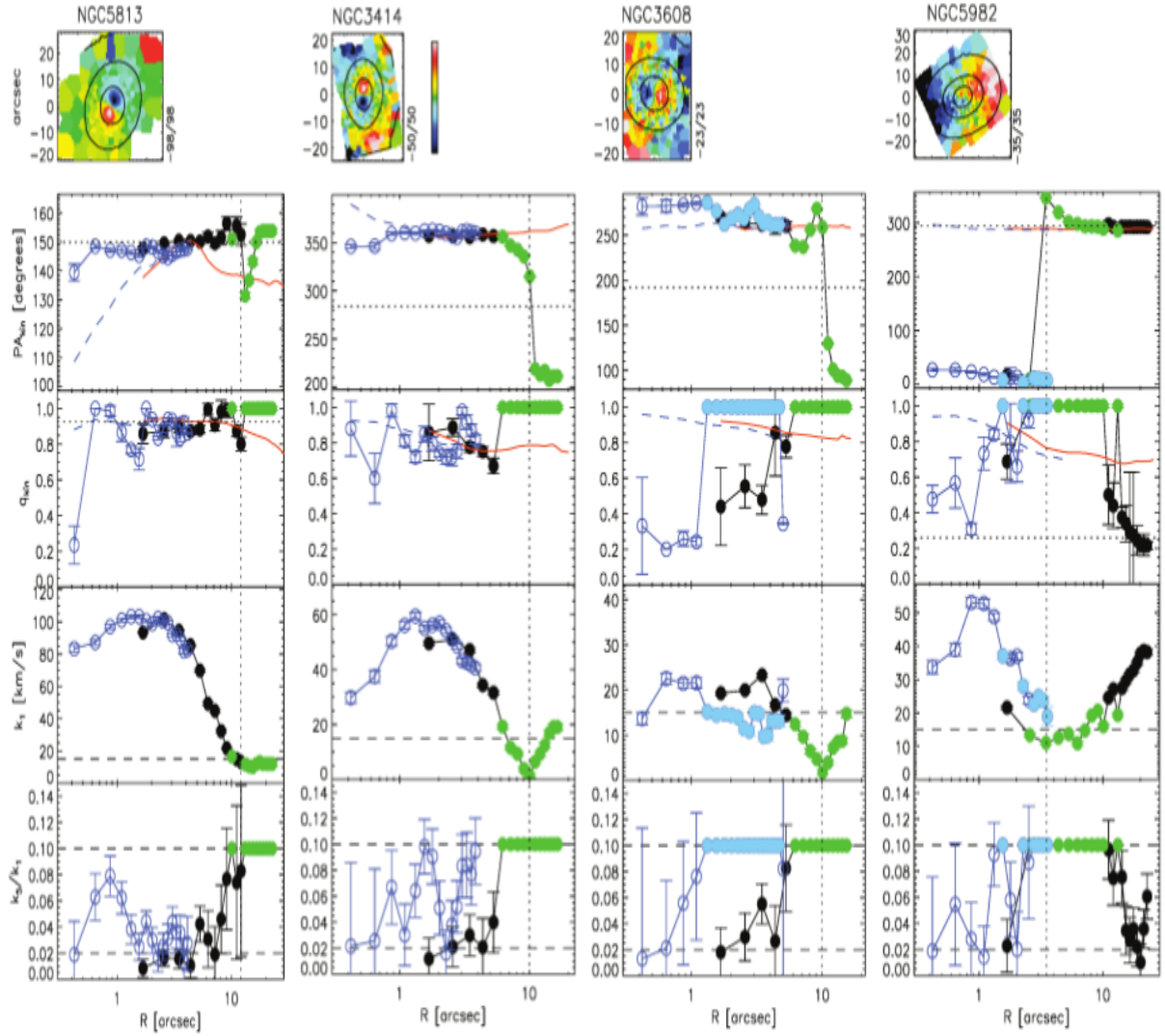


Figure 6.1.4: Kinematic properties of NGC 5813, 3414, 3608, and 5982 (from left to right) extracted from SAURON/OASIS data. The first row shows the SAURON stellar velocity maps (Voronoi binned), the following rows show the kinematic profiles (from top to bottom): position angle, axial ratio,  $k_1$  and  $k_1/k_5$  coefficients. Solid black symbols refer to SAURON data, open blue circles to OASIS data. The other symbols are not relevant for the present discussion.

name	diameter [kpc]	$R_{\max}/R_e$
NGC 3414	$2.8 \pm 0.4$	0.12
NGC 3608	$2.3 \pm 0.1$	0.1
NGC 5813	$3.1 \pm 0.2$	0.08
NGC 5982	$2.0 \pm 0.2$	0.15

Table 6.2: Diameter of the KDCs and corresponding fraction of the effective radius found in NGC 3414, 3608, 5813 and 5982 (McDermid et al. 2006).

galaxies.

We finally notice that four galaxies (i.e. NGC 4374, 4486, 4278 and 3665) of the ATLAS<sup>3D</sup> sample are classified as Radio Galaxies. NGC4374 and NGC4486 are both classified as *Slow Rotators* while NGC 4278 and NGC 4486 are classified as *Fast Rotators*. As already discussed, the classification of NGC 4278 is questioned, and the presence of a large KDC was suggested instead (Krajinović et al. 2011). Despite the low statistics available, this may indicate that large KDCs are common in RGs.

The complete reduction and analysis of VIMOS/IFU data of the eleven radio galaxies of the Southern Sample, will certainly help to shed light on the kinematic properties of radio galaxies and will allow a more robust comparison with the ATLAS<sup>3D</sup> sample.

## 6.2 Linking radio-quiet to radio-loud ETGs

NGC 3557 is a *low power* radio galaxy hosting an AGN and showing twin jets. Due to dust, a classification of its surface brightness nuclear profile was not possible (see Chapter 2), but it is very likely that, like all radio galaxies for which a profile can be derived, it is a core galaxy (de Ruiter et al. 2005, Capetti et al. 2005, Capetti et al. 2006). The formation of a core profile seems indeed to be more consistent with high mass and large size of the galaxy. Krajinović et al. 2013 studied the surface brightness profile properties of ATLAS<sup>3D</sup> galaxies finding that, indeed, most massive ( $M > 2 \times 10^{11} M_{\odot}$ ) and largest ( $R_e \geq 5$  kpc) ATLAS<sup>3D</sup> galaxies tend to have core profiles. In particular at masses  $M > 5 \times 10^{11} M_{\odot}$  no core-less galaxy was found (see the mass-size diagram presented in Figure 1.8.4).

As reported in Krajinović et al. (2013) core galaxies are mostly associated with massive *Slow Rotators*, however a genuine population of core-less *Slow Rotators* and core *Fast Rotator* was found.

Nevertheless Krajinović et al. (2013) showed that core galaxies tend to have low  $\lambda_R$  values (always  $\lambda_R \leq 0.25$ , except for one galaxy, where a  $\lambda_R \gtrsim 0.3$  was measured). In addition core galaxies always have large velocity dispersions ( $\sigma_e \geq 160$  km s<sup>-1</sup>, see the  $\lambda_R - \sigma_e$  diagram presented in Figure 1.8.5). Again, the relatively low  $\lambda_R$  ( $\simeq 0.33$ ) and the high  $\sigma_e$  ( $=236$  km s<sup>-1</sup>) values found for NGC 3557 point towards a core profile classification.

While the large majority of ATLAS<sup>3D</sup> galaxies are radio-quiet, a few tens of them show AGN-driven radio emission at some level. The four brightest ones ( $P_{1.4} > 10^{22} WHz^{-1}$ ) are the aforementioned radio galaxies (Senatore et al. 2013). As discussed in Chapter 2, all the AGN-powered ATLAS<sup>3D</sup> galaxies with  $P_{1.4} > 10^{22} WHz^{-1}$ , for which a profile could be derived, are core galaxies. This strongly suggests a link between radio emission and core profile, and consequently a link between the formation scenario yielding core profiles and the triggering of AGN-driven radio emission.

As discussed in Chapter 1, the currently favoured scenario for the formation of core profiles is based on binary BH interactions, in equal mass dry mergers. Such a scenario can explain most core profiles ATLAS<sup>3D</sup> galaxies which are associated to *Slow Rotators*. However the fact that core profiles can be found in some *Fast Rotators* as well, yields Krajinović et al. (2013) to suggest that different processes, also involving dissipative major mergers could produce core galaxies.

The core growth in a gas-rich merger could be guaranteed, for example, by very long timescales for the BH interaction process (longer than for star formation) and/or by star formation regulating processes, like AGN feedback, morphological quenching etc. The fact

that AGN-triggered radio emission is linked to the presence of core profiles may indeed support an important role of AGN feedback.

### 6.3 Future work

In this thesis we have presented a first preliminary analysis of the stellar kinematics of NGC 3557. However a lot of work remains to be done to exploit the VIMOS/IFU NGC 3557 data, as summarized below:

- The flux calibration inconsistency for Q3 need to be solved (if ever possible). This would allow us to reach a higher S/N for each spectrum and to use the entire wavelength range (i.e. 4000-5300 Å) for the fitting procedure, providing more reliable and complete results.
- An accurate evaluation of the binning procedure for the 4500-5300 Å range has to be carried out in order to remove the many low S/N bins and to obtain better  $v$  and  $\sigma$  maps.
- Once the aforementioned problems will be solved, the ionized gas component can be analysed. The kinematic misalignment/alignment and the metallicity of the ionized gas with respect to the stellar component will shed light on the external/internal origin of the gas itself.
- After modeling and removing the ionized gas component, the stellar population analysis can be carried out. It should be noted that pPXF, when used with synthetic galaxy template spectra (arranged in a grid of ages and metallicities) constitutes a state-of-the-art method to extract stellar population information from observed galaxy spectra. This method represents the most efficient and reliable public implementation of the so called "Full-Spectrum Fitting" method and, thanks to the availability of high-quality model spectra, is becoming a popular alternative to the use of line-strength indices in the study of stellar populations..
- Monte Carlo simulations for a robust estimate of errors and confidence levels to be applied to the kinematic parameters have to be carried out.

# Bibliography

Allen Steven W., Dunn R. J., Fabian A. C., Taylor G. B., Reynolds C. S., 2006, MNRAS, 372, 21

Annibali F., Bressan A., Rampazzo R., Zeilinger W. W., Vega O., Panuzzo P., 2010, A&A, 519A, 40

Annibali F., Bressan A., Rampazzo R., Zeilinger W. W., Danese L., 2007, A&A, 463, 455

Antonucci R., 1993, ARA&A, 31, 473

Baldwin J. A., Phillips M. M., Terlevich R., 1981, PASP, 93, 5

Barnes J. E., 2002, MNRAS, 333, 481

Baum S. A., Zirbel E. L., O'Dea C. P., 1995, ApJ, 451, 88

Baum S. A., Heckman T. M., van Breugel W., 1992, ApJ, 389, 208

Bendo George J., Barnes Joshua E., 2000, MNRAS, 316, 315

Best P. N., Heckman T. M., 2012, MNRAS, 421, 1569

Bettoni D., Falomo R., Fasano G., Govoni F., Salvo M., Scarpa R., 2001, A&A, 380, 471

Binney J., 2005, MNRAS, 363, 973

Bois M., et al. 2011, MNRAS, 416, 1654

Buttiglione S., Capetti A., Celotti A., Axon D. J., Chiaberge M., Macchetto F. D., Sparks W. B., 2010, W. B., 2010, A&A, 509, 6

Capetti A., Balmaverde B., 2006, Memorie della Società Astronomica Italiana Supplementi, 9, 313

Capetti A., Balmaverde B., 2005, A&A, 440, 73

Cappellari M., et al., 2012a, arXiv:1208.3523

Cappellari M., et al. 2011, MNRAS, 416, 1680

Cappellari M., et al, 2011, MNRAS, 413, 813

Cappellari, M., et al., 2010, Highlights of Astronomy, 15, 81

Cappellari M., 2008, MNRAS, 390, 71

Cappellari M., et al., 2007, MNRAS, 379, 418

Cappellari M., et al., 2006, MNRAS 366, 1126

Cappellari M., Emsellem E., 2004, PASP, 116, 138

Cappellari M., Copin Y., 2003, MNRAS, 342, 345

Chiaberge M., Capetti A., Celotti A., 2002, A&A, 394, 791

Ciddor, P.E., Appl. Optics 1996, 35, 1566

Colbert James W., Mulchaey John S., Zabludoff Ann I., 2001, AJ, 121, 808

Colla G., Fanti C., Fanti R., Gioia I., Lari C., Lequeux J., Lucas R., Ulrich M. H., 1975, AAP, 38, 209

Condon J. J., Cotton W. D., Broderick J. J., 2002, AJ, 124, 675

Davies T., et al., 2011, MNRAS, 417, 882

de Koff S., Best P., Baum S.A., et al., 2000, ApJS, 129, 33

de Ruiter H. R., Parma P., Capetti A., et al., 2005, A&A, 439, 487

de Ruiter H. R., Parma P., Capetti A., Fanti R., Morganti R., 2002, A&A, 396, 857

de Zeeuw P.T. et al., 2002, MNRAS, 329, 513

Dressler A., 1980, ApJ, 236, 351

Dumas G., Emsellem E, Mundell C. G., 2007, IAUS, 235, 94

Ekers R. D., Wall J. V., Shaver P. A., Goss W. M., Fosbury R. A. E., Danziger I. J., Moorwood A. F. M., Malin D. F., Monk A. S., Ekers J. A., 1989, MNRAS, 236, 737

Emsellem E. et al. 2011, MNRAS, 414, 888

Emsellem E. et al., 2007, MNRAS, 379, 401

Emsellem E., et al., 2004, MNRAS, 352, 721

Emsellem, E., Monnet, G., & Bacon, R. 1994, A&A, 285, 723

Faber S. M., et al., 2007, ApJ, 665, 265 Barnes Joshua E., 2002, MNRAS, 333, 481

Faber S. M. et al., 1997, AJ, 114, 1771

Fanaroff B. L., Riley J. M., 1974, MNRAS, 167, 31

Franx M., Illingworth G., de Zeeuw P.T., 1991, ApJ, 383, 112

Govoni F., Falomo R., Fasano G., Scarpa R., 2000, A&A, 353, 507

Gruyters P., Exter K., Roberts T. P., Rappaport S., 2012, A&A, 544, 86

Hardcastle M. J., Evans D. A., Croston J. H., 2007, MNRAS, 376, 1849

Heckman T. M., Smith Eric P., Baum Stefi A, van Breugel W. J. M., Miley G. K., Illingworth G. D., Bothun G. D., Balick B., 1986, ApJ, 311, 526

Hill G. J., Lilly S. J., 1991, ApJ, 367, 1

Horellou C., Black J. H., van Gorkom J. H., Combes F., van der Hulst J. M., Charmandaris V., 2001, AAP, 376, 837

Husemann B., Kamann S., Sandin C., Sánchez S.F., García-Benito R., Mast D., 2012, A&A, 545, 137

Jesseit R., Cappellari M., Naab T., Emsellem E., Burkert A., 2009, MNRAS, 397, 1202

Kauffmann G., Heckman T. M., Tremonti C., et al., 2003, MNRAS, 346, 1055

Kewley L. J., Dopita M. A., Sutherland R. S., Heisler C. A., Trevena J., 2001, ApJ, 556, 121

Khochfar S., et al., 2011, MNRAS, 417, 845

Krajnović D. et al., 2013, arXiv:1305.4973K

Krajnović D. et al., 2011, MNRAS, 414, 2923

Krajnović D. et al., 2008, MNRAS, 390, 93

Krajnović D., Cappellari M., de Zeeuw P.T., Copin Y., 2006, MNRAS, 366, 787

Laing R. A., Jenkins C. R., Wall J. V., Unger S. W., 1994, in "The First Stromlo Symposium: The Physics of Active Galaxies.", eds. G.V. Bicknell, M.A. Dopita, and P.J. Quinn, ASP Conference Series, 54, 201

Lauer Tod R., Faber S. M., Gebhardt Karl, Richstone Douglas, Tremaine Scott, Ajhar Edward A., Aller M. C., Bender Ralf, Dressler Alan, Filippenko Alexei V., Green Richard, Grillmair Carl J., Ho Luis C., Kormendy John, Magorrian John, Pinkney Jason, Siopis Christos, 2005, AJ, 129, 2138

Lauer T. R., 2012, ApJ, 759, 64

Lauer R. R., et al., 1995, AJ, 110, 2622

Leon S., Lim J., Combes F., Dinh-v-Trung, 2003, ASPC, 290, 525

Lim J., Leon S., Combes F., Dinh-v-Trung, 2003, ASPC, 290, 529

Mahony E. K., et al., 2011, MNRAS, 417, 2651

McDermid R.M., Emsellem E., Shapiro K.L., Bacon R., Bureau M., Cappellari M., Davies R.L., de Zeeuw, P.T., Falcón-Barroso J., Krajnović D., Kuntschner H., Peletier R.F., Sarzi M., 2006, MNRAS, 373, 906

Milosavljević M., Merritt D., Rest A., van den Bosch F.C., 2002, MNRAS, 331, L51

Monreal-Ibero A., Roth M. M., Schönberner D., Steffen M., Böhm P., 2006, NewAR, 50, 426

Ocaña Flaquer B., Leon S., Combes F., Lim J., 2010, A&A, 518, 9

Ogle Patrick, Boulanger Francois, Guillard Pierre, Evans Daniel A., Antonucci Robert, Appleton P. N., Nesvadba Nicole, Leipski Christian, 2010, ApJ, 724, 1193

Okuda T., Kohno K., Iguchi S., Nakanishi K., 2005, ApJ, 620, 673

Oosterloo T., Morganti R., Crocker A., Jütte E., 2010, MNRAS, 409, 500

Oser L., Ostriker J.P., Naab T., Johansson P.H., Burkert A., 2010, ApJ, 725, 2312

Owen F. N., Ledlow M. J., 1994, in "The First Stromlo Symposium: The Physics of Active Galaxies.", eds. G.V. Bicknell, M.A. Dopita, and P.J. Quinn, ASPC, Vol. 54, p319

Owen F. N., 1993, LNP, 421, 273

Prandoni I., Laing R. A., de Ruiter H. R., Parma P., 2010, A&A, 523A, 38

Prandoni I., Laing R. A., Parma P., de Ruiter H. R., Montenegro-Montes F. M., Wilson T. L., 2007, ASPC, 375, 271P

Ramos Almeida C., et al., 2012, MNRAS, 419, 687

Rhoads J. E., 2000, PASP, 112, 703

Ryden B. S., Terndrup D. M., Pogge R. W., Lauer T. R., 1999, ApJ, 517, 650

Sage Leslie J., Welch Gary A., 2006, ApJ, 644, 850

Sánchez-Blázquez, P., et al. 2006, MNRAS, 371, 703

Sandage A., Brucato R., 1979, AJ, 84, 472

Sandin C. , Weilbacher P., Tabataba-Vakili F., Kamann S., Streicher O., 2012, in: "Software and Cyberinfrastructure for Astronomy II", Radziwill N. M., Chiozzi G., eds, Proc. SPIE, 8451, 84510F-1-16 – © 2012 SPIE

Sandin C., Becker T., Roth M.M., Gerssen J., Monreal-Ibero A., Böhm P., Weilbacher P., 2010, A&A, 515, 35

Sarzi M., et al., 2006, MNRAS, 366, 1151

Schlegel D. J., Finkbeiner D. P., Davis M., 1998, ApJ, 500, 525

Scott N., et al., 2009, MNRAS, 398, 1835

Senatore et al., 2013, A&A, submitted

Serra P., et al., 2012, MNRAS, 422, 1835

Sharp R., Birchall M. N., 2010, PASA, 27, 91

Skrutskie M. F., et al., 2006, AJ, 131, 1163

Spitzer Jr.L., Baade, W., 1951, ApJ, 113, 413

Urry C. M., Padovani P., 1995, PASP, 107, 803

van den Bergh S., 1976, ApJ, 206, 883

van Dokkum P.G., 2001, PASP, 113, 1420–1427

Verdoes Kleijn G. A., de Zeeuw P. T., 2005, A&A, 435, 43

Westmoquette M. S., Smith L. J., Gallagher J. S., 2011, MNRAS, 414, 3719

York D. G. et al., 2000, AJ, 120, 1579

Young Lisa M., et al., 2011, MNRAS, 414, 940Y